Scuola Internazionale Superiore di Studi Avanzati

Physics Area
Ph.D. Course in Astrophysics

Thesis submitted in partial fulfillment of the requirements for the degree of Doctor Philosophiæ

CMB lensing signal analysis: prospects for measurements and characterisation for future surveys

Supervisor:
Prof. Carlo Baccigalupi

Candidate:
Claudia Antolini

Academic Year 2013-2014

I'll meet you in a dream.

"Mais nous n'avons qu'une seule vie.
Même si j'obtenais la fortune, même si j'atteignais la gloire,
j'éprouverais sûrement le sentiment d'avoir perdu la mienne,
si je cessais un seul jour de contempler l'Univers."

M. Yourcenar

Abstract

Within the last few years, Cosmic Microwave Background gravitational lensing has become a new tool for cosmology and astrophysics. As a new independent kind of measurement in this field, it can help to break the degeneracy between the cosmological parameters and determining their values with a better accuracy. This field of research is becoming increasingly prominent and fertile in the latest years, both as a way to investigate the evolution of the Universe at late times, and in relation to the EUCLID mission preparatory science work, aiming at mapping galaxies on ABOUT 30% of the sky reaching a redshift of about 2.

The aim of this thesis is to characterise the lensing signal in the CMB and to study the efficiency of lensing extraction at small angular scales from simulated CMB maps lensed by N-body simulations, and how this translates in constraining Dark Energy and its relevant parameters for the expansion.

After investigating the balance between the tensor modes and lensing in the $B-$mode power spectrum [1], the feasibility of lensing extraction on CMB lensed N-body simulations is demonstrated [2]: the faithfulness of the implemented pipeline is assessed and verified for upcoming experimental setups and validated ranging from the degree to the arcminute scale.

List of Abbreviations

CMB ..... Cosmic Microwave Background

LSS ..... Large Scale Structure

DE ..... Dark Energy

ΛCDM ..... Λ Cold Dark Matter (standard model of cosmology)

DM ..... Dark Matter

CC ..... Cosmological Constant

EoS ..... Equation of State

SM ..... Standard Model (of particle physics)

CIB ..... Cosmic Infrared Background

SN ..... SuperNova

BAO ..... Baryonic Acoustic Oscillations

QFT ..... Quantum Field Theory

CPL ..... Chevallier-Polanski-Linder

PGWs ..... Primordial Gravitational Waves

FWHM ..... Full-Width at Half-Maximum

MCMC ..... Monte Carlo Markov Chains

LP ..... `LensPix`

MS ..... Millennium Simulation

DEMNUNI ... Dark Energy Massive Neutrino Universe

CoDECS .... Coupled Dark Energy Cosmological Simulations

Contents

Introduction

During the last decade, Cosmic Microwave Background (CMB) gravitational lensing has become a new and promising tool for cosmology and astrophysics after its detection with high significance by the collaborations ACT[1] [3] and SPT[2] [4]. As a new independent kind of measurement in this field, it can help to break the degeneracy between key cosmological parameters related in particular to the cosmological expansion history and determining their values with a better accuracy. Also the PLANCK experiment, in the first cosmological data release of March 2013, has been able to extract the lensing pattern from the temperature anisotropy maps [5]; ground-based and balloon experiments have the instrumental capabilities to detect a signal in the $B-$modes of the CMB, which are dominated by the lensing signal at high multipoles. First detections of the lensing signal coming from the polarised $B-$modes of the CMB have already been presented by the SPT [6] and POLARBEAR[3] [7] collaborations. The state of the art of the technology and analysis is shortening more and more the time needed for a full characterisation of the signal in different spectra and different angular scales.

Moreover, data collected in this framework can be combined with other probes, e.g. the Large Scale Structure (LSS), to give further insight on the history of the recent Universe (in the range $1 < z < 3$) and the evolution of Dark Energy (DE) during the latest evolution phases of the Universe. This latter phenomenon is tightly related to CMB lensing, as the recent expansion history of the Universe, characterised by an accelerated expansion given by the DE, determines the statistics of structures that will arise and hence the number of gravitational lenses that will distort the CMB spectrum during its trip from the last scattering surface to us. In this regard, measuring this effect can give a better description of the recent evolution history of the Universe [8]; moreover, this phenomenon has been shown to be capable of breaking the projection degeneracy affecting CMB anisotropies at the linear level [9], as it was recently confirmed in the context of lensing detection for sub-orbital $T-$mode[4] experiments [10]. Once data from advanced LSS surveys like EUCLID [11] will become available, the next step towards a deeper

[1] Atacama Cosmology Telescope

[2] South Pole Telescope

[3] Characterization of the POLARization of the Background Radiation

[4] This notation will be used throughout this work: $T-$mode refers to the temperature or total intensity spectra, while $E-$ and $B-$mode refer to the E and B polarisation respectively.

understanding of this signal and characterization of the recent evolution of the Universe will be the process of cross-correlating the two signals: the structures in the foreground, that deflect the CMB on its path to the observer, with the deflections themselves. In [2], for the first time, CMB maps lensed by N-body simulations were targeted for the extraction and characterisation of the deflection signal.

Besides the implications for the ability to constrain the parameters of the standard ΛCDM[5] cosmology, the considered phenomenon can shed light on possible extensions to more exotic scenarios, and in the understanding of still open crucial questions in fundamental physics. Involving the process of clustering in the recent Universe, the angular spectrum of lensing is heavily influenced not only by the acceleration of the expansion in the redshift span $0.5 < z < 2$, but also by its possible deviation from a Cosmological Constant (CC) during cosmic time, or by different assumptions on the Equation of State (EoS) of the DE component [1]. Various theoretical and phenomenological models have been proposed in the recent years, and new observational probes, either coming from specifically designed experiments or from synergies between different datasets, are being planned. In the era of high precision cosmology, exploiting the available information and improving the accuracy of the theoretical predictions, both with analytical and computational methods, will allow in the near future to understand the mechanism underlying the expansion by discriminating efficiently between different theoretical models and by characterizing the physics of the recent expansion with increasing precision.

Another physical quantity that affects the gravitational lensing of the CMB is the mass of neutrinos which affects the matter power spectrum [12] that gives rise to structures which distort the CMB emission. Neutrino physics has provided the first clear indication of particle physics beyond the Standard Model (SM), as there is now experimental evidences for non-zero neutrino masses from the oscillation between different neutrino flavors. The sum of neutrino masses is currently bounded by cosmology to be $\Sigma m_\nu \lesssim 0.2$ eV [13]; and CMB lensing can effectively constrain this observable [14]. Combining information from cosmology with data coming from an experiment such as KATRIN[6] [15] our current knowledge will be improved by an order of magnitude on the sum of the masses, possibly shedding light on the mass hierarchy of neutrinos.

The motivation of this thesis is to explore the capabilities of CMB lensing as an independent cosmological probe, and to characterize the relevant quantities also in relationship with other phenomena such as tensorial modes coming from inflation. A deep comprehension of the features of this observable is most important in view of cross-correlating CMB lensing measurements with those of LSS which are responsible for the lensing itself, following the path of building synergies between different observational probes. In view of this, a lensing extraction algorithm applied to N-body lensed CMB maps is presented, on an extended range of angular

[5]The acronym stands for Λ Cold Dark Matter. Λ indicates the presence of DE under the form of a Cosmological Constant (CC) in Einstein equations, while CDM (Cold Dark Matter) means that the particles of Dark Matter (DM) are not relativistic (and hence cold) at the moment of recombination.

[6]KArlsruhe TRItium Neutrino experiment

scales, both for a standard ΛCDM case, and for a set of maps with a non-zero value of the neutrino mass. This work aims to demonstrate the feasibility of CMB lensing studies based on large scale simulations of cosmological structure formation in the context of the upcoming large observational campaigns.

Outline of the thesis

In Chapter 1 the effect of weak lensing on the CMB is presented, along with the relevant physical observables; in Chapter 2 possible expansions of the standard model of cosmology are presented and discussed; in Chapter 3 forecasts of the $B-$mode polarisation of the CMB as a tool for constraining simultaneously primordial tensors and an evolving DE EoS are illustrated; in Chapter 4 the process of ray tracing through simulated N-body structures of unlensed CMB is described, and the recovered lensing signal with the reconstructed shear maps are presented. Finally, the conclusions and possible extensions of the work illustrated in this Thesis are discussed.

1

Weak lensing of the Cosmic Microwave Background

Experimental measurements of the CMB radiation anisotropies are one of the most fertile research areas in cosmology since their detection, and have provided fundamental evidence for establishing our knowledge about the Universe, enabling the scientific community to formulate the now standard ΛCDM cosmological model. The CMB photons are an invaluable source of information about the physics of the Early Universe and the properties of the matter perturbations which evolved from the primordial fluctuations to constitute the structures we can observe today.

As experiments became more and more sensitive along the years, it has been possible to detect the modifications enacted by the cosmological and astrophysical evolution of the large scale structures on the CMB photons themselves. This class of phenomena is often referred to as secondary anisotropies, in opposition to primary anisotropies, which were generated by the physical effects taking place at the time of recombination.

Among the most significant of the former, stands the distortion enacted by gravitational lensing of CMB photons by the evolving LSS on the line of sight connecting the observer to the last scattering surface, when CMB photons started to propagate freely. Gravitational lensing bends the trajectories of CMB photons modifying their overall statistical properties. The polarised component is more affected with respect to the total intensity because lensing generates a curl-like pattern ($B-$modes) from the overall gradient-like pattern ($E-$modes) of a CMB polarisation field even in absence of a primordial components of $B-$modes, to be discussed later.

In this Chapter the relevant CMB observables and power spectra characterising the anisotropies will be defined (in Sec. 1.1 and Sec. 1.2); subsequently, the basics of weak lensing will be described in Sec. 1.3, and the application of this effect as a secondary anisotropy of CMB is presented in Sec. 1.4. In Sec. 1.5, the state of the art of the observations is discussed.

1.1 CMB observables

The basic observable of CMB is the intensity as a function of frequency and direction $\hat{\mathbf{n}}$ in the sky. Since the CMB spectrum follows very carefully a black body

radiation with a nearly constant temperature across the sky, we can describe the intensity of the anisotropies field simply in terms of temperature fluctuations:

$$\Theta(\hat{\mathbf{n}}) = \frac{\Delta T}{T}. \tag{1.1}$$

The CMB signal is distributed over the sphere of the sky; by projecting it on the orthonormal function set over the sphere its harmonic domain representation is obtained:

$$\Theta_{\ell m} = \int d\hat{\mathbf{n}} Y^*_{\ell m}(\hat{\mathbf{n}})\Theta(\hat{\mathbf{n}}). \tag{1.2}$$

Its expansion on the spherical harmonics set will thus be

$$\Theta(\tau, \overrightarrow{x}, \hat{\mathbf{n}}) = \sum_{\ell m} Y_{\ell m}(\hat{\mathbf{n}})\Theta_{\ell m}(\tau, \overrightarrow{x}). \tag{1.3}$$

A similar approach can be applied to the polarised component of the light, which is characterised in the following.

A homogeneous and isotropic black body distribution is unpolarised by definition. If the black body temperature varies with position and photon propagation direction, differences in the strength of the electric and magnetic fields along different axes may occur. This is the case of the CMB, as the Thomson scattering of CMB photons on electrons happening at the time of decoupling is markedly anisotropic. If Θ is measured on a given direction $\hat{\mathbf{n}}$, one may project the intensity onto two perpendicular axes orthogonal to $\hat{\mathbf{n}}$ forming the polarisation plane, defining

$$Q(\tau, \overrightarrow{x}, \hat{\mathbf{n}}) = \Theta_{\parallel} - \Theta_{\perp} \ , \ U(\tau, \overrightarrow{x}, \hat{\mathbf{n}}) = \Theta_{\nparallel} - \Theta_{\nperp}, \tag{1.4}$$

where τ is the optical depth at the moment of recombination, $\overrightarrow{x}$ is the direction of observation, and Q, U are the Stokes parameters describing linear polarisation (the symbols $\nparallel$ and $\nperp$ represent axes rotated by $\pi/4$ with respect to the ones defining Q). A third Stokes parameter, V, is needed to describe circularly polarised radiation; however, it is not considered here as Thomson scattering produces linear polarisation only.

Polarisation physically arises from products of the electric and magnetic fields on the plane orthogonal to $\hat{\mathbf{n}}$ thus behaving as a rank 2 tensor. It is possible to show that Q and U represent the amplitude of the decomposition of the polarisation tensor into the Pauli matrices σ_1 and σ_3:

$$\mathbf{P} = Q\sigma_3 + U\sigma_1 = \begin{pmatrix} Q & U \\ -U & Q \end{pmatrix}. \tag{1.5}$$

It is useful to define the matrices

$$\mathbf{M}_{\pm} = \frac{1}{2}(\sigma_3 \mp i\sigma_1), \tag{1.6}$$

so that one can rewrite

$$\mathbf{P} = (Q + iU)\mathbf{M}_{+} + (Q - iU)\mathbf{M}_{-} \tag{1.7}$$

and analogously with what has been done for the temperature, compute the projection and the expansion on the tensorial spherical harmonics basis for the polarisation:

$$\mathbf{P} = (Q \pm iU)(\tau, \overrightarrow{x}, \hat{\mathbf{n}})\mathbf{M}_{\pm} = \sum_{\ell m} {}_{\pm 2}Y_{\ell m}(\hat{\mathbf{n}})(Q \pm iU)_{\ell m}(\tau, \overrightarrow{x}) \tag{1.8}$$

where ${}_{\pm 2}Y_{\ell m}(\hat{\mathbf{n}})$ are the tensor spherical harmonics, needed to define the expansion on the spherical set for a rank 2 tensor such as polarisation. In order to connect this quantity, which is frame dependent, with the cosmological observables, it is useful to define two different modes for the polarisation spin-2 field:

$$\begin{aligned} {}_{\pm 2}E_{\ell m} &= \frac{(Q+iU)_{\ell m} + (Q-iU)_{\ell m}}{2} \\ {}_{\pm 2}B_{\ell m} &= i\frac{(Q+iU)_{\ell m} - (Q-iU)_{\ell m}}{2}. \end{aligned} \tag{1.9}$$

This allows us to rewrite the polarisation tensor in Eq. 1.8

$$\mathbf{P} = (Q \pm iU)\mathbf{M}_{\pm} = \sum_{\ell m}(E_{\ell m}Y^{E}_{\ell m}\mathbf{M}_{E} + B_{\ell m}Y^{B}_{\ell m}\mathbf{M}_{B}). \tag{1.10}$$

The combinations $E_{\ell m}Y^{E}_{\ell m}$ and $B_{\ell m}Y^{B}_{\ell m}$ pick up a $(-1)^{\ell}$ and $(1)^{\ell+1}$, respectively, under transformations $\hat{\mathbf{n}} \rightarrow -\hat{\mathbf{n}}$. These parity relations coincide with those prescribed for the angular distribution of two fields generated by the gradient of a scalar potential, and the curl of a vector one, respectively, as in the case of the electric field $\overrightarrow{E}$ and the magnetic field $\overrightarrow{B}$. For this reason, we can consider the E and B components to be the gradient-like and curl-like components of the polarisation field [16, 17] and the E, B notation is chosen for the polarised modes of CMB. It is to be noted that in absence of any cosmological process which is parity violating, we expect the cross-correlation signal between ΘB and EB to vanish.

1.2 Temperature and polarisation power spectra

If we assume that CMB anisotropies obey a Gaussian statistics, as the density fluctuations produced during inflation are expected to do, the multipole moments of the temperature and polarisation fields are characterised completely by their angular power spectrum (or the Fourier transform of the 2-point correlation function in real space)

$$\begin{aligned} \langle \Theta_{\ell m}\Theta^{*}_{\ell' m'} \rangle &= \delta_{\ell\ell'}\delta_{mm'}C_{\ell}^{\Theta\Theta} \\ \langle E_{\ell m}E^{*}_{\ell' m'} \rangle &= \delta_{\ell\ell'}\delta_{mm'}C_{\ell}^{EE} \\ \langle \Theta_{\ell m}E^{*}_{\ell' m'} \rangle &= \delta_{\ell\ell'}\delta_{mm'}C_{\ell}^{\Theta E} \\ \langle B_{\ell m}B^{*}_{\ell' m'} \rangle &= \delta_{\ell\ell'}\delta_{mm'}C_{\ell}^{BB} \end{aligned}$$

There is an ongoing search for deviations from Gaussianity, as a possible indication towards discriminating between different inflationary models. The current

upper limits on deviations from the second order statistics of the CMB have been presented by the PLANCK Collaboration in [18], measuring the first order quadratic correction to the gravitational potential to be compatible with zero within 68% confidence level.

Although this represents a loss of information, (e.g. the phases of the coefficients are lost) such a description is convenient from the point of view of a statistical description of the observables. Furthermore, if each coefficient is a Gaussian variable with known variance, no physical information is coded into the phases of CMB anisotropies, so that the compression is not deteriorating our overall knowledge.

Performing the full linearisation of the Einstein equations, one can classify the perturbations to a homogeneous background in scalar, vector (which represent vortical motions in the primordial plasma and are damped by the expansion if produced near the time of recombination) and tensor type perturbation. Fig. 1.1 provides the different contribution of these two types of primordial perturbations to the different power spectra.

Scalar perturbations represent the main contribution to the Θ power spectrum, which encodes the angular distribution of temperature anisotropies in the sky. Its structure reflects the physics ongoing at the moment of recombination: the peaks represent the oscillations of the tightly coupled matter-radiation fluid on different scales. The angular extension in spherical harmonics and the small thickness of the last scattering surface determine a tight relation between the angular scale θ and the multipole ℓ: $\theta \approx \frac{200}{\ell}$ degrees. The Hubble horizon at decoupling subtends about 1° on the sky, corresponding to $\ell \approx 200$. The odd peaks represent moments of maximum compression, while the even ones represent the maximum expansion of bubbles of size corresponding to that particular angular scale. This is due to the evolution of short wavelength modes that enter the horizon before recombination: the first peak corresponds to the mode that entered the horizon at the moment of decoupling. It had just the time to undergo half an oscillation, and corresponds to an overdensity region. The subsequent peaks are due to smaller scale modes undergoing one or more oscillations. On very small scales, the oscillations are damped: this is due to an imperfect coupling between baryons and photons on smaller scales. Perturbations on scales smaller than the mean free path of photons are washed out.

Scalar perturbations are able to contribute to the polarisation via a non-zero quadrupole term present at recombination. After electrons combine with protons to produce neutral hydrogen, the photons can travel undisturbed: their mean free path increases progressively and every electron sees more and more anisotropic incoming radiation, due to both density and dipolar (velocity) perturbations present at that time. The resulting quadrupole is proportional to the velocity field, and will be small if the derivative of the opacity is large; it will grow only at the moment of decoupling thanks to the drop of the opacity.

The tensor perturbations produce a signature in the $E-$mode signal and in Θ although its amplitude is much lower than the level of polarisation anisotropies

induced by density perturbations in the ΛCDM model, especially in the case of temperature (see again Fig. 1.1). The main contribution of $E-$mode power spectra derives from the density perturbation quadrupole which is subjected to the same acoustic physics of temperature perturbation and show therefore acoustic oscillations in the power spectrum.

$E-$modes vary in strength in the same direction as the orientation of the polarisation vector, suggesting an analogy with the electric field from a point source, which changes in intensity as one moves away from the source along the direction of the field. On the contrary, $B-$modes polarisation varies in strength in a different direction from the one of the polarisation vector; this kind of pattern on the sky has in fact an additional azimuthal dependence which drives the pattern to vary along a direction at 45° with respect to the polarisation vector. This peculiar feature is directly connected to the physical origin of the $B-$modes.

In fact, the distinction between different kinds of perturbations is crucial in this case, since tensor modes, corresponding to gravitational waves, represent the transverse trace-free perturbations to the spatial metric, and constraints on inflation are obtained by comparing theoretically calculated scalar and tensor metric perturbations to measurements of these perturbations. The amplitude of the tensor power spectrum relative to the scalar spectrum defines the tensor-to-scalar ratio r, which is currently the main parameter used to characterise the energy scale of inflation. The amplitude of $B-$modes power spectrum on large scale is in fact directly proportional to this parameter, and a measurement of a non-zero value of r would be a smoking-gun evidence that an inflationary mechanism occurred in the early Universe, as since the $E-$modes are activated by all kinds of cosmological perturbations, the primordial $B-$modes can be sourced by vector-type and tensor-type perturbations only. The other cosmological contributor to the spectra of the $B-$modes is gravitational lensing of the CMB. The coexistence of these two effects in this spectrum will be the subject of Chapter 3 and therefore it will not be discussed in detail here.

The CMB temperature and polarisation anisotropy power spectrum is a powerful mean to constrain cosmological parameters through the dependence of the acoustic phenomenology on the sound horizon, angular diameter distance and the gravitational potential evolution. After the detection made by COBE in 1992 [19] several collaborations started to hunt the acoustic peaks to track down the composition of the Universe and inaugurated the era of precision cosmology from the CMB. The state of the art for CMB measurements and constraints on cosmological parameters is represented by the first cosmological data release coming from the PLANCK experiment [13].

At the present moment, the analytical and numerical tools developed to predict the spectrum are able to detect and distinguish the influence of a huge variety of physical effects. A complete list would be therefore very long and is beyond the scope of the writer; in the following, the effect of the main parameters which define the standard cosmological model without any sake of completeness is done, remembering also that the effect of cosmological parameters is very often degenerate and the overall result of the variation of several quantities is more complicated

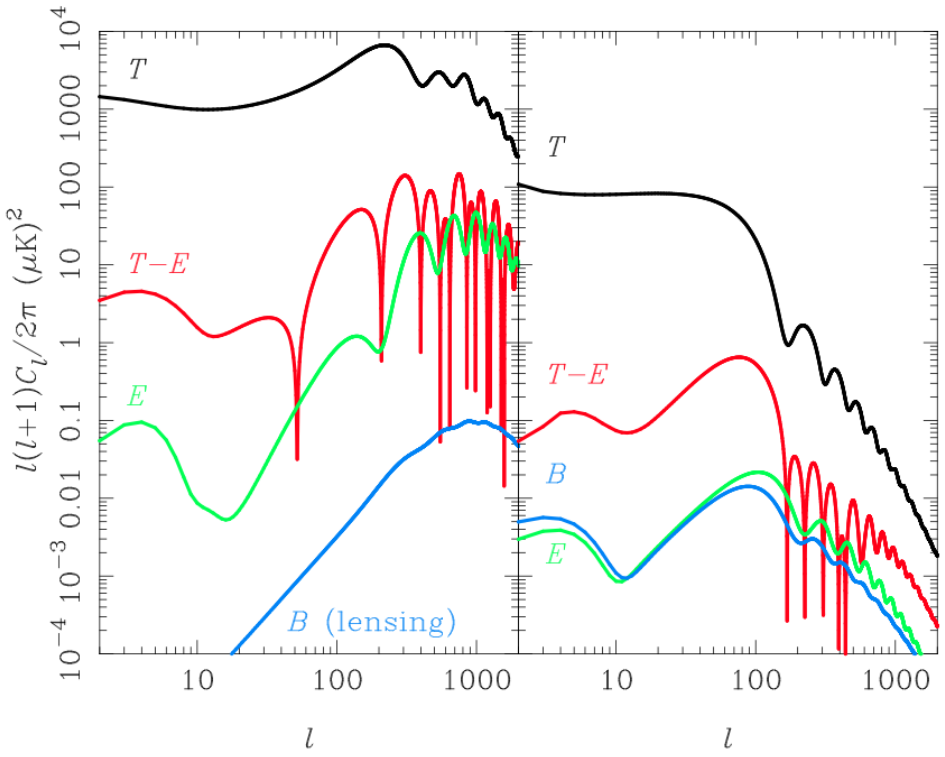

Figure 1.1: Temperature (black), $E-$mode (green), $B-$mode (blue) and TE cross-correlation (red) CMB power spectra from scalar perturbations (left) and tensor perturbations (right). The $B-$mode spectrum induced by weak gravitational lensing is also shown in the left panel. Figure from [20].

that what will be outlined in the following.

- Curvature Ω_k: in an open or closed Universe, the angular diameter distance to the last scattering surface changes with respect to the flat Universe case where it is simply equal to $\eta_0 - \eta$. It approximately scales as $(1 - \Omega_k^{-0.45})$ [21] and is therefore larger in an open Universe. The value of the curvature therefore shifts the location of the acoustic peaks and has been the first parameter to be effectively constrained around the year 2000. See Fig. 1.2.

- Dark Energy Ω_Λ: the dynamical effects of DE are late-time phenomena as at the time of recombination its energy density was negligible. Therefore, the only possible effect is on the free-streaming of photons on large scales which entered the horizon just recently, which is visible through an enhancement of power in large scale anisotropies due to a late-time integrated Sachs-Wolfe effect. See again Fig. 1.2.

- Baryon density $\Omega_b h^2$: the baryon density changes the sound speed and subsequently the sound horizon, shifting the position of peaks. Adding baryons, the sound speed is reduced and the compression phase is enhanced without

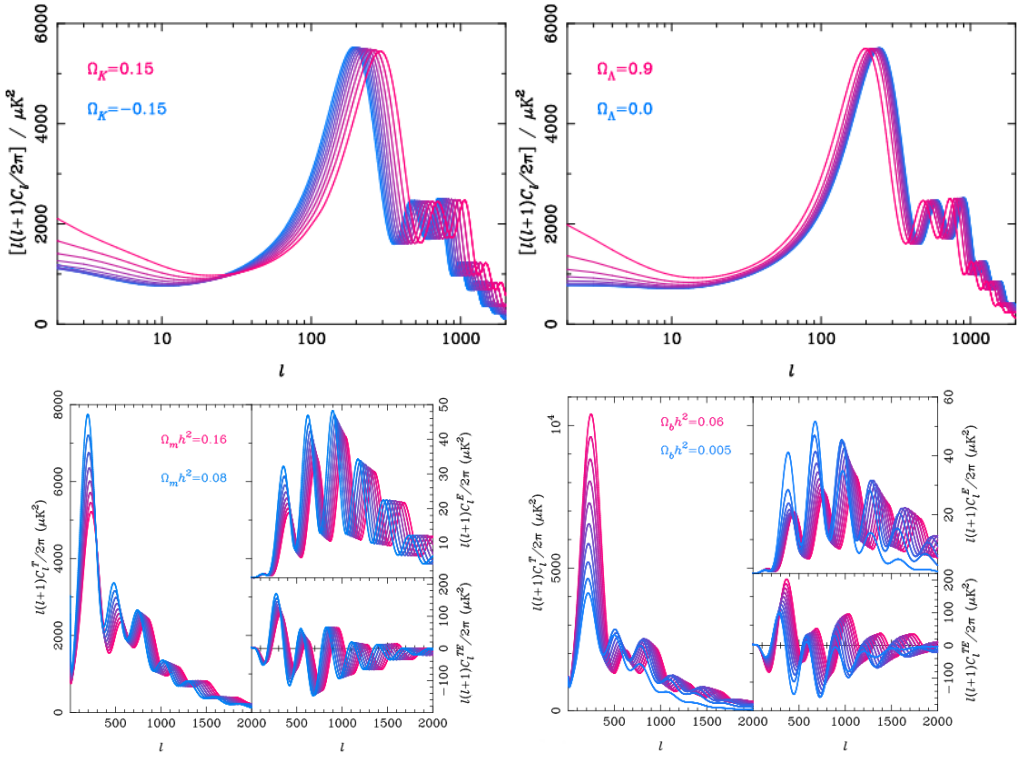

Figure 1.2: Top panel: sensitivity of the temperature power spectrum to curvature (left) and DE (right) density. Bottom panel, left: sensitivity of the temperature and polarisation power spectra to the DM density. Bottom panel, right: sensitivity of the temperature and polarisation power spectra to the baryon density. Figure from [20].

increasing in the pressure, leading to an overall increased height of the odd peaks. See again Fig. 1.2.

- Matter density $\Omega_m h^2$: the total matter density defines the moment of equality, i.e. when energy density in the radiative component equals the one due to matter. If the matter content is low, the equality happens closer to recombination and thus an additional radiative component must be taken into account when computing inhomogeneities at recombination. This component enhances the oscillations, therefore there are more CMB anisotropies on small scales if the matter density is low. This can be understood as follows: since the background density is decreasing with time, the density fluctuations must grow unimpeded by pressure to maintain constant potentials. In a radiation dominated regime pressure begins to fight gravity at the first compressional extreme of the acoustic oscillation, therefore the Newtonian gravitational potential and spatial curvature must decay. The decay drives the oscillations as at the moment of maximum compression, there is no gravitational potential neither curvature perturbation to overcome as the sound waves turns around. When the Universe becomes matter dominated the

gravitational potential is no longer dominated by density perturbations of the DM which is insensitive to pressure. See again Fig. 1.2.

- Optical depth to reionisation τ_{re}: as the first stars and galaxy form, the hydrogen and helium, who recombined at the last scattering surface, begin to ionise again interacting with the energetic photons from astrophysical sources. Electrons are therefore free again to interact with CMB photons and eventually to wash out the acoustic peaks. The overall effect for the temperature anisotropies is a uniform decrease of the amplitude of the peaks by a factor $e^{-\tau_{re}}$, where τ_{re} is the optical depth of the Universe at the moment of reionisation, for all the angular scales inside the horizon at that time. Electron scattering during reionisation also generates new large-angle polarisation, as an effect of the presence of a quadrupole at that time, giving rise to a bump in the power spectrum of $E-$modes on angular scales

$$\ell_{re} \approx 2\frac{(\eta_0 - \eta_{re})}{\eta_{re} - \eta_*}, \tag{1.11}$$

  where η_* is the comoving distance to the CMB [22]. The screening effect of reionisation on CMB power spectrum complicates the inference of the amplitude of the primordial fluctuations power spectrum from temperature data alone as this effect is degenerate with τ_{re}.

- Spectral index of the scalar perturbations n_s: this quantity represents the steepness of the power spectrum of the primordial fluctuations

$$P(k) = A_s k^{n_s - 1}, \tag{1.12}$$

  where k represents the wavenumber of the fluctuations, and A_s the amplitude of the primordial power spectrum. A value of $n_s = 1$ represents a scale invariant power spectrum, with the perturbations equally distributed on the different scales.

  Modifying this number tilts the initial part of the temperature power spectrum: as it increases, more perturbations are produced at small spatial scales; for this reason, they enter the horizon earlier, and can grow more than those at higher scales, lowering the temperature power spectrum at very low multipoles. The converse is true if n_s decreases.

- Hubble constant H_0: this is the expansion rate at the present time; it is generally referred to as a constant for its uniformity in space, as opposed to its variation as a function of time. With respect to the aforementioned parameters, H_0 is a derived parameter, i.e. it does not appear directly as a parameter in the Boltzmann equations describing CMB physics, but it is rather proportional to the square root of the sum of the abundances of the different components of the Universe at the present time[1]

$${H_0}^2 = 4\pi G \rho_0. \tag{1.13}$$

[1] Throughout this thesis, natural units $\hbar = c = k_B = 1$ with $\hbar$ the reduced PLANCK constant, c the speed of light in vacuum and k_B the Boltzmann constant will be used.

where G is the gravitational constant, and ρ_0 represents the sum of the different contributions now (baryons and DM, DE, radiation, which is negligible today, and curvature, assumed to be zero). For this reason, the effects of its variation on the CMB are composite, and cannot be shortly synthetised, as a variation of H_0 corresponds necessarily also to a variation of another parameter, or combination of parameters.

1.3 Basics of weak lensing

Even before General Relativity, the deviation of light rays by the presence of a mass had been already postulated by Newton, Laplace and Cavendish among others. Lensing by galaxies is a major sub-discipline of gravitational lensing today. The most accurate mass determinations of the central regions of galaxies are due to data coming from this effect, and the cosmic telescope effect of gravitational lenses has enabled us to study faint and distant galaxies which happen to be magnified by galaxy clusters. The statistics of gravitational lensing events is now a new probe for inferring cosmological parameters.

Within the framework of Einstein's theory of gravity, the description of the phenomenon is as follows: the path of photons is affected by the presence of a mass, that distorts space-time in its vicinities, and bends their trajectory of a certain angle, related to the (distribution of) mass encountered, as it can be seen in Fig. 1.3. The deflection can be computed knowing the deflecting mass (acting as a lens) and the distance from the source and the lens between each other and from the source and lens to the observer.

Looking closer at the subject, it is found that gravitational lensing manifests itself through a very broad and interesting range of phenomena, e.g. the magnification effect enables us to observe objects which flux would be too low to be observed without lensing; its independence from the luminosity or composition of the lens, being purely gravitational in origin, which enables us to study the distribution of the total mass of the lens; the fact that the distribution and characteristics of lensed objects depend on the age, the scale, and the overall geometry of the Universe.

The propagation of light in arbitrary curved space-times is in general a complicated theoretical problem. However, for almost all cases of cosmological relevance to gravitational lensing, we can assume that the overall geometry of the Universe is well described by the Friedmann-Lemâitre-Robertson-Walker metric

$$ds^2 = dt^2 - a(t)^2 \left[\frac{dr^2}{1-kr^2} + r^2 d\Omega \right], \tag{1.14}$$

where k is the spatial curvature of the Universe, and that the matter inhomogeneities which cause the lensing are local perturbations to the overall matter distribution.

To study the path of the light ray and compute the deflection, we can consider the trajectory as separated in three different parts: the first one, from the source

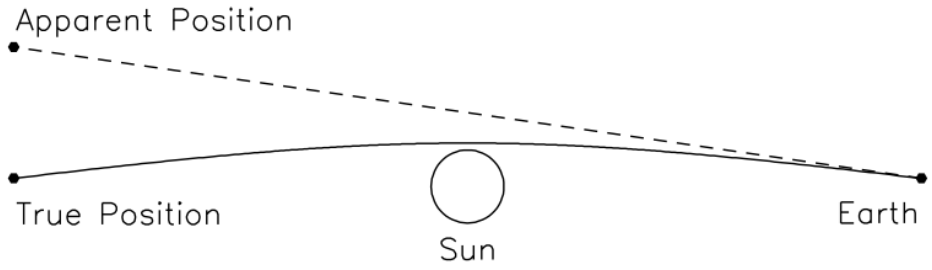

Figure 1.3: Angular deflection of a ray of light passing close to the surface of the Sun. Since the light ray is deviated by the Sun and converges to us, the apparent positions of stars appears further from the Sun with respect to their actual position. Figure from [23].

to the deflecting mass, where space-time is Minkowskian, the second one near the lens, where light is deflected, and the third one from the lens to the observer, where space-time is Minkowskian again. This approach is legitimate if the Newtonian potential generated by the lens Φ is small enough, $|\Phi| << 1$, and if the peculiar velocity of the lens is far from being relativistic, $v << 1$.

Assuming that the simplifications just discussed are reliable, we can describe light propagation close to gravitational lenses in a locally Minkowskian space-time perturbed by the gravitational potential of the lens to the first post-Newtonian order. The effect of the curvature of space-time on the light paths can then be expressed in terms of an effective index of refraction n, given by [24]

$$n = 1 - 2\Phi = 1 + 2|\Phi|. \tag{1.15}$$

Note that the Newtonian potential is negative if it is defined such that it approaches zero at infinity. A refractive index $n < 1$ implies that light travels slower than in free vacuum. Thus, the effective speed of a ray of light in a gravitational field will be reduced

$$v = \frac{1}{n} \simeq (1 + 2|\Phi|). \tag{1.16}$$

As in the case of a ray of light through a medium with different refraction index, light rays are deflected when they pass through a gravitational field; the deflection is the integral along the light path of the perpendicular component of the gradient of n to the light path

$$\alpha = -\int \overrightarrow{\nabla}_{\perp} n dl = 2\int \overrightarrow{\nabla}_{\perp} \Phi dl. \tag{1.17}$$

Let us now derive the lens equation. Consider a mass concentration in a single point, placed at redshift z_L, corresponding to an angular diameter distance of D_L, which deflects the light rays coming from the source, placed at a redshift z_S corresponding to an angular diameter distance D_S (see Fig. 1.4). Defining the optical

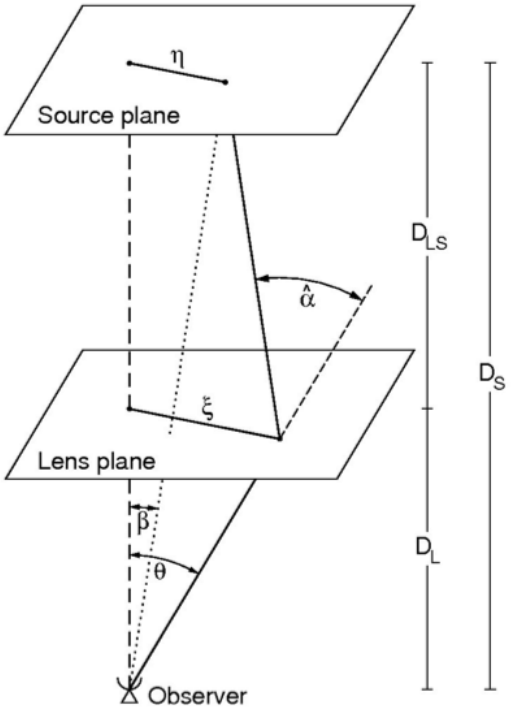

Figure 1.4: Sketch of a gravitational lensing system as described in the text. Figure from [25].

axis, indicated by the dashed line, perpendicular to the lens and source planes and passing through the observer, we can measure the angular positions on the lens and on the source planes with respect to this reference direction. The angle between the optic axis and the true source position is $\overrightarrow{\beta}$, and the angle between the optic axis and the image is $\overrightarrow{\theta}$. The (angular diameter) distances between observer and lens, lens and source, and observer and source are D_L, D_{LS} and D_S respectively. It is convenient to define the reduced deflection angle $\overrightarrow{\hat{\alpha}}$

$$\overrightarrow{\hat{\alpha}} = \frac{D_S}{D_{LS}} \overrightarrow{\alpha}. \tag{1.18}$$

From Fig. 1.4 we see that

$$\theta D_S = \beta D_S + \overrightarrow{\hat{\alpha}} D_{LS}, \tag{1.19}$$

and from this relation we can derive the lens equation

$$\overrightarrow{\beta} = \overrightarrow{\theta} - \overrightarrow{\alpha}(\overrightarrow{\theta}). \tag{1.20}$$

Considering an extended distribution of mass, we can define its effective lensing potential, obtained by projecting the 3-D Newtonian potential on the lens plane

and rescaling it appropriately

$$\psi(\overrightarrow{\theta}) = 2\int_0^{D_S} \frac{D_{LS}}{D_S D_L}\Phi(D_L\overrightarrow{\theta}, z)dz, \tag{1.21}$$

where we must remember that the angular diameter distances depend from the different geometry of the Universe:

$$D_A = \frac{f_K(\eta)}{1+z} \text{ where } f_K(\eta) = \begin{cases} K^{-1/2}\sin(\sqrt{K}\eta) & K>0 \\ \eta & K=0 \\ |K|^{-1/2}\sinh(\sqrt{|K|}\eta) & K<0 \end{cases} \tag{1.22}$$

where η is the comoving distance, and f_K expresses the dependency on the curvature of the Universe. Computing the gradient and laplacian of this quantity we find

$$\begin{aligned} \overrightarrow{\nabla_\theta}\psi &= D_S\overrightarrow{\nabla_\xi}\psi = 2\int \overrightarrow{\nabla_\perp}\Phi dz = \overrightarrow{\alpha} \\ \overrightarrow{\nabla^2_\theta}\psi &= 2\int \frac{D_L D_{LS}}{D_S}\overrightarrow{\nabla^2_\xi}\Phi dz = 2\kappa(\overrightarrow{\theta}), \end{aligned} \tag{1.23}$$

where κ is the convergence, defined as the dimensionless surface density

$$\kappa(\theta) \equiv \frac{\Sigma}{\Sigma_{cr}} \text{ with } \Sigma_{cr} = \frac{1}{4\pi G}\frac{D_S}{D_L D_{LS}}, \tag{1.24}$$

where Σ_{cr} is called the critical surface density, a quantity which characterises the lens system and which is a function of the angular diameter distances of lens and source.

To study the local properties of the lens mapping we can define the Jacobian matrix A

$$A \equiv \frac{\partial\overrightarrow{\beta}}{\partial\overrightarrow{\theta}} = \left(\delta_{ij} - \frac{\partial\alpha_i(\overrightarrow{\theta})}{\partial\theta_j}\right) = \left(\delta_{ij} - \frac{\partial^2\psi(\overrightarrow{\theta})}{\partial\theta_i\partial\theta_j}\right) = M^{-1}, \tag{1.25}$$

where, as indicated, A is the inverse of the magnification tensor M. A solid angle element $\delta\beta^2$ of the source is mapped to the solid angle element of the image $\delta\theta^2$, and so the magnification is given by

$$\frac{\delta\theta^2}{\delta\beta^2} = \frac{1}{\det A} = \det M. \tag{1.26}$$

Introducing the abbreviation $\dfrac{\partial^2\psi(\overrightarrow{\theta})}{\partial\theta_i\partial\theta_j} = \psi_{ij}$ for the Hessian matrix, we can write the Laplacian of ψ (that as seen in Eq. 1.23 is twice the convergence) as follows

$$\kappa = \frac{1}{2}(\psi_{11}+\psi_{22}) = \frac{1}{2}\text{tr }\psi_{ij}. \tag{1.27}$$

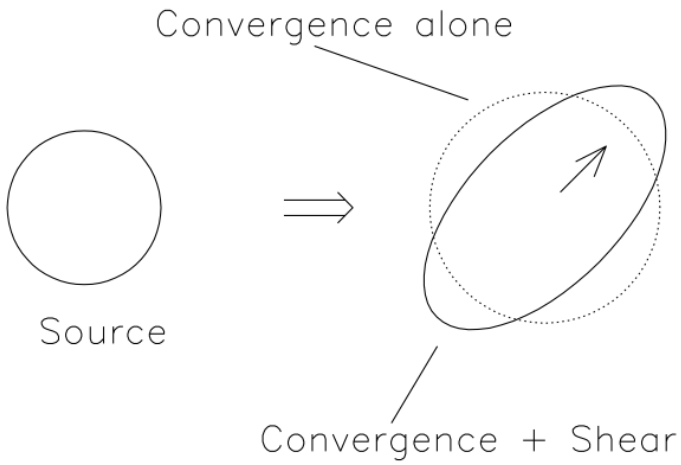

Figure 1.5: Illustration of the effects of convergence and shear on a circular source. Convergence magnifies the image isotropically, and shear deforms it to an ellipse. From [23].

Two more linear combinations of the components of ψ_{ij} are worthy of mention:

$$\begin{aligned} \gamma_1 = \frac{1}{2}(\psi_{11} - \psi_{22}) &\equiv \gamma(\vec{\theta}) \cos\left[2\phi(\vec{\theta})\right] \\ \gamma_2 = \psi_{12} = \psi_{21} &\equiv \gamma(\vec{\theta}) \sin\left[2\phi(\vec{\theta})\right]. \end{aligned} \tag{1.28}$$

With these definitions, the Jacobian can be rewritten

$$\begin{aligned} A &= \begin{pmatrix} 1-\kappa-\gamma_1 & -\gamma_2 \\ -\gamma_2 & 1-\kappa-\gamma_2 \end{pmatrix} = \\ &= (1-\kappa)\begin{pmatrix} 1 & 0 \\ 0 & 1 \end{pmatrix} - \gamma \begin{pmatrix} \cos(2\phi) & \sin(2\phi) \\ \sin(2\phi) & -\cos(2\phi) \end{pmatrix}. \end{aligned} \tag{1.29}$$

The meaning of the terms *convergence* and *shear* can be now understood more intuitively. Convergence acting alone, meaning a diagonal Jacobian, causes an isotropic focusing of light rays, leading to an isotropic magnification of a source, in analogy with what happens with an ordinary magnification lens: the source is mapped onto an image with the same shape but different size. Shear, that comes in the off-diagonal component of the Jacobian shear, introduces anisotropy into the lens mapping. The quantity $\gamma = \left[{\gamma_1}^2 + {\gamma_2}^2\right]^{\frac{1}{2}}$ represents the magnitude of the shear and ϕ describes its orientation on the celestial sphere. In the presence of both components, a circular image of unit radius from the source becomes an elliptical image with major and minor axis given by $(1-\kappa\pm\gamma)^{-1}$, oriented along the angle ϕ, and magnified of a factor $\mu = \det M = \dfrac{1}{\det A} = \dfrac{1}{\left[(1-\kappa)^2 - \gamma^2\right]}$. In Fig. 1.5 the two effects can be seen graphically.

To integrate this treatment and make it more suitable for discussing the effect of weak lensing on CMB, let us compute how this deflection influences the observed angle θ subtended by an object at comoving distance η_* we have to consider how the comoving distances are related to angles via the angular diameter distance remembering Eq. 1.22. From Eq. 1.17, we have learned that

$$\delta\alpha = -2\delta_{||}\nabla_{\perp}\Phi, \tag{1.30}$$

where $\delta_{||}$ is an infinitesimal distance along the photon trajectory.

The comoving distance that the sources appear to have moved from their actual position due to lensing is $f_K(\eta_S - \eta)\delta\alpha = f_K(\eta_S)\delta\theta$, where η_S is the comoving distance to the source. Solving for $\delta\theta$ and integrating over the whole distance between us and the last scattering surface to take into account all the deflections from all the potential gradients present on the line of sight, a total deflection in terms of the potential gradients along the line of sight can be obtained

$$\mathrm{d}(\hat{\mathbf{n}}) = \int_0^{\eta_*} d\chi \frac{f_K(\eta_* - \chi)}{f_K(\eta_*)}\nabla_{\perp}\Phi(\chi\hat{\mathbf{n}}; \eta_0 - \chi), \tag{1.31}$$

where now the comoving distance to the source is now the comoving distance to CMB. From here, we can define an integral potential called *lensing potential* from which we can compute the displacement vector applying a transverse differential operator $\nabla_{\perp}$.

$$\phi(\hat{\mathbf{n}}) \equiv -2\int_0^{\eta_*} d\chi \frac{f_K(\eta_* - \eta)}{f_K(\eta_*)}\Phi(\chi\hat{\mathbf{n}}; \eta_0 - \chi). \tag{1.32}$$

1.4 Essentials of CMB lensing

The CMB anisotropy spectra today incorporate both the primary, originated at decoupling, and secondary, after decoupling, anisotropies. Weak lensing of the CMB, which is a secondary anisotropy, is due to the LSS deflecting the CMB photons according to the distribution of matter, or, in general, of gravitational potential along their path from the last scattering surface to the observer. As we will see, lensing does not generate additional power, but rather redistributes it from large scales to smaller ones [26]. For this reason, lensing generated small scale power is correlated with the large scale gradient of the CMB. This property is an important signature for distinguishing lensing from other physical processes that give rise to a signal at small scales. If we consider the potential Φ to be Gaussian, the lensing potential ϕ defined in Eq. 1.32 is Gaussian, too, and therefore can be completely described by its power spectrum. In order to evaluate it we can expand the lensing potential in standard scalar spherical harmonics. Since the lensing potential is a statistically isotropic field, we then define its angular power spectrum in the usual way

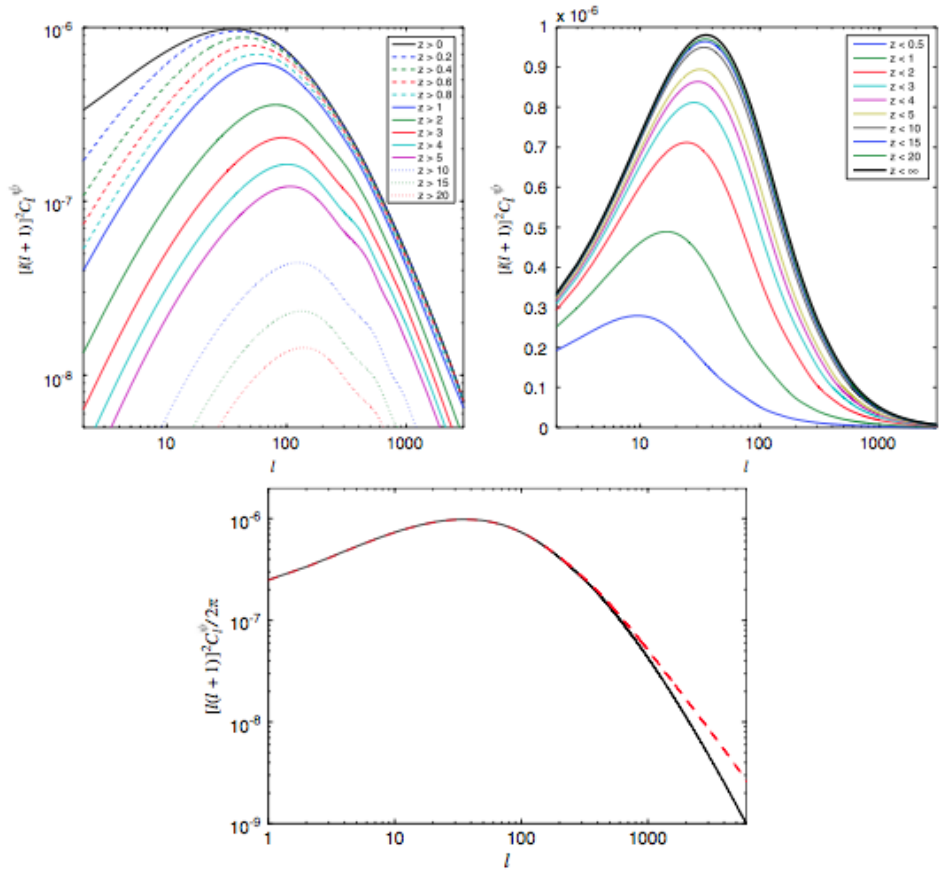

Figure 1.6: Top panel: Cumulative contribution of different redshifts to the power spectrum of the lensing potential for a concordance ΛCDM model, in log-log and log-linear scales. Note that here the lensing potential power spectrum is referred to as C_ℓ^ψ whereas in the text the same quantity is denoted as $C_\ell^{\phi\phi}$. Bottom panel: Effect of non-linear correction on lensing potential for a ΛCDM model. From [26].

$$\begin{aligned} \phi(\tau, \overrightarrow{x}, \hat{\mathbf{n}}) &= \sum_{\ell m} Y_{\ell m}(\hat{\mathbf{n}}) \phi_{\ell m}(\tau, \overrightarrow{x}) \\ \langle \phi_{\ell m} \phi^*_{\ell' m'} \rangle &= \delta_{\ell\ell'} \delta_{mm'} C_\ell^{\phi\phi}. \end{aligned} \tag{1.33}$$

In Fig. 1.6 the behaviour of the lensing angular power spectrum in the harmonic domain, computed according to Eqs. 1.32 and 1.33 is shown. DM structures, which follow closely the linear regime and with sizes of hundreds of Mpc or more, dominate the lensing power in the range $\ell \lesssim 200$. On angular scales larger than a few hundreds, it is to be expected that the assumption of a linear and Gaussian lensing potential becomes less accurate due to the non-linear evolution of ϕ at late times. This can be estimated using numerical simulations [27, 28] or

semi-analytic models like HALOFIT [29] which are expected to be accurate at few percent level for standard ΛCDM cosmologies with a power law primordial power spectra. The last scattering surface is a long way away, so the lensing potential has contributions out to quite high redshift as show in Fig. 1.6. In the low redshift Universe, potentials only contribute to the large-scale lensing, so the spectrum is only quite weakly sensitive to late time non-linear evolution [26]. The lensing potential power spectrum including non-linear corrections shows an increase of power which becomes more important on small scales while the region close to the lensing potential peak is weakly affected (cf. Fig. 1.6). The accuracy of the non-linear correction effect is however limited by the precision of the model describing the non-linear power spectrum; including non-linear corrections will not introduce a significant level of non-Gaussianity on the lensing potential. These are reduced by the fact that the a photon is deflected several times during its journey from the last scattering surface and the lensing potential is effectively more Gaussian than the gravitational potential itself. In order to calculate the effect of lensing on CMB temperature anisotropies, we can restrain ourself for sake of simplicity to a perturbative expansion of the CMB observable field. In the following the effect of lensing on CMB will be outlined on temperature and then polarisation spectra.

1.4.1 Lensing of the temperature field

Lensing remaps the CMB temperature[2] as

$$\tilde{T}(\hat{\mathbf{n}}) = T(\hat{\mathbf{n}}') = T(\hat{\mathbf{n}} + \alpha) = T(\hat{\mathbf{n}} + \nabla_\perp \phi), \tag{1.34}$$

where the symbol $\sim$ denotes the lensed quantities. This relation can be expanded as follows

$$\begin{aligned} &\tilde{T}(\hat{\mathbf{n}} + \nabla_\perp \phi) = \\ &\quad \approx \tilde{T}(\hat{\mathbf{n}}) + \nabla^a \phi(\hat{\mathbf{n}}) \nabla_a T(\hat{\mathbf{n}}) + \frac{1}{2} \nabla^a \phi(\hat{\mathbf{n}}) \nabla^b \phi(\hat{\mathbf{n}}) \nabla_a \nabla_b T(\hat{\mathbf{n}}) + \dots \end{aligned} \tag{1.35}$$

If one expands this relation in Fourier domain assuming a flat sky approximation for the sake of simplicity, it reads [26, 30, 31]

$$\begin{aligned} \tilde{T}(\boldsymbol{\ell}) = T(\boldsymbol{\ell}) - \int \frac{d^2\boldsymbol{\ell}_1}{(2\pi)^2} \boldsymbol{\ell}_1 (\boldsymbol{\ell}_1 - \boldsymbol{\ell}) T(\boldsymbol{\ell}_1) \phi(\boldsymbol{\ell} - \boldsymbol{\ell}_1) - \frac{1}{2} \int \frac{d^2\boldsymbol{\ell}_1}{(2\pi)^2} T(\boldsymbol{\ell}_1) \cdot \\ \cdot \left[\int \frac{d^2\boldsymbol{\ell}_2}{(2\pi)^2} \phi(\boldsymbol{\ell}_2) \phi^*(\boldsymbol{\ell}_2 + \boldsymbol{\ell}_1 - \boldsymbol{\ell}) (\boldsymbol{\ell}_2 \cdot \boldsymbol{\ell}_1) (\boldsymbol{\ell}_2 + \boldsymbol{\ell}_1 - \boldsymbol{\ell}) \boldsymbol{\ell}_1 \right] + \dots \end{aligned} \tag{1.36}$$

This expansion is not a good approximation on all scales. On intermediate ones, order of 30^o on the sky, the lensing deflection is of the same order of the angular scales of the anisotropies which are being deflected and a perturbative expansion in the deflection angle is not suitable for a precise estimation of the effect. Nevertheless, this simple approach is useful to understand the most important effects

[2] From now on, the temperature field will be referred to as T in the text.

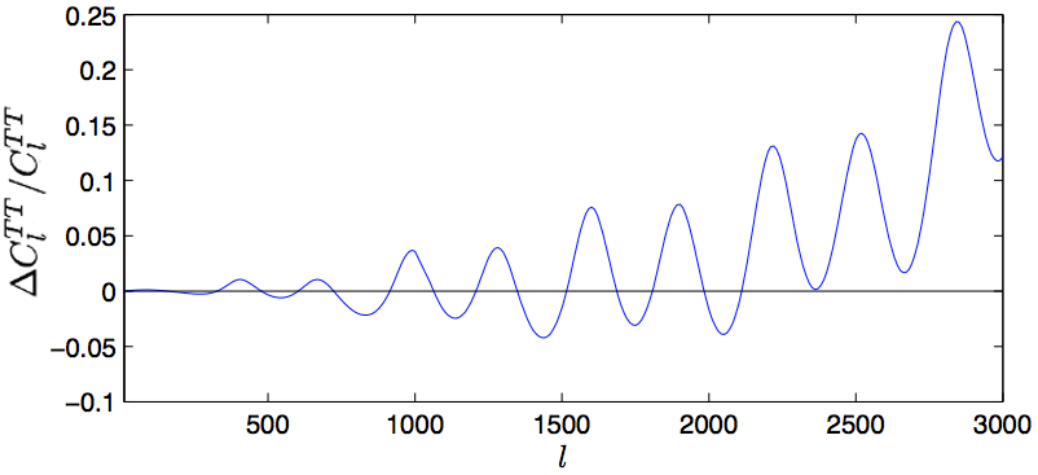

Figure 1.7: Fractional change in the power spectrum due to lensing for a ΛCDM model. Figure adapted from [26].

on a good range of angular scales: from the presence of two different $\boldsymbol{\ell}$ vectors combined together in Eq. 1.36 we understand one of the main features of CMB lensing, i.e. the coupling of different angular scales in the resulting spectrum of anisotropies. Lensing correlates different angular dimensions on the sky, redistributing power from the large to the small scales, and smearing the peaks of the power spectrum.

From Eq. 1.36 one can deduce the lensed CMB power spectrum in the usual way, as the lensing field from a statistical isotropic field does not break the statistical isotropic properties of the CMB.

$$\begin{aligned} \tilde{C}_\ell^{TT} &\approx (1-\ell^2 R^\phi) C_\ell^{TT} + \int \frac{d^2\ell}{(2\pi)^2} \left[\boldsymbol{\ell}'(\boldsymbol{\ell}-\boldsymbol{\ell}')\right]^2 C_{\ell'}^{TT} C_{|\boldsymbol{\ell}-\boldsymbol{\ell}'|}^{\phi\phi} \\ \text{where} \quad R^\phi &= \frac{1}{2}\langle|\nabla\phi|^2\rangle = \frac{1}{4\pi}\int \frac{d\ell}{\ell}\ell^4 C_\ell^{\phi\phi}. \end{aligned} \tag{1.37}$$

In the last equation we neglected the temperature-lensing potential correlation, since the $T\phi$ correlation is small on most of the angular scales and its effect on the lensed power spectrum is also small [32]. At the first order in $C_\ell^{\phi\phi}$, the lensed power spectrum differs from the unlensed coefficients by a term proportional to half of the total deflection angle power R^ϕ and by an integral term which has the form of a convolution of the unlensed temperature spectrum with the lensing potential power spectrum. This convolution effectively smooths out the main peaks and troughs of the unlensed spectrum and cause a fractional change in the power spectrum, shown in Fig. 1.7, equal to several percent at $\ell \sim 1000$. On small scales, where there is little power in the unlensed CMB because of Silk damping,

the convolution transfers power from large scales to small scales increasing the small scales power (cfr. Fig. 1.7 again).

A more exact calculation can be obtained using the curved sky approach implemented in [30, 31]; for the scales considered in this work the flat-sky approximation is an accurate description, as it will be motivated in Chapter 4.

1.4.2 Lensing of the polarisation field

The presence of a quadrupole moment at last scattering generates a polarisation signal which will also be lensed by potential gradients along the line of sight. This effect can be treated in a way similar to what has been done for lensing of the temperature field, with the further complication that polarisation is not a scalar field but a spin-2 (tensor) field. In the following, the effect of lensing on the E and B fields defined in Sec. 1.2 will be analysed as the components of the polarisation tensor.

Evaluating the polarisation power spectra is a similar process to the temperature case. We can first remap the polarisation spin-2 field with the usual lensing equation and then use a perturbative expansion to evaluate the leading term contributing to the power spectra:

$$\begin{aligned}\tilde{P}_{ab}(\hat{\mathbf{n}} + \nabla_{\perp}\phi) \approx\ & \tilde{P}_{ab}(\hat{\mathbf{n}}) + \\ & + \nabla^{c}\phi(\hat{\mathbf{n}})\nabla_{c}P_{ab}(\hat{\mathbf{n}}) + \frac{1}{2}\nabla^{c}\phi(\hat{\mathbf{n}})\nabla^{d}\phi(\hat{\mathbf{n}})\nabla_{c}\nabla_{d}P_{ab}(\hat{\mathbf{n}}) + ... \end{aligned} \quad (1.38)$$

By performing the Fourier transform of this quantity with the flat sky version of the spin-2 spherical harmonic and then computing the power spectrum would lead to a lensed E and $B-$modes polarisation power spectra

$$\begin{aligned}\tilde{C}_{\ell}^{EE} &\approx (1-\ell^{2}R^{\phi})C_{\ell}^{EE} + \int \frac{d\ell}{(2\pi)^{2}}\left[\boldsymbol{\ell}'(\boldsymbol{\ell}-\boldsymbol{\ell}')\right]^{2} C_{\ell'}^{EE} C_{|\ell-\ell'|}^{\phi\phi}\cos^{2}2(\gamma_{\ell'}-\gamma_{\ell}) \\ \tilde{C}_{\ell}^{TE} &\approx (1-\ell^{2}R^{\phi})C_{\ell}^{TE} + \int \frac{d\ell}{(2\pi)^{2}}\left[\boldsymbol{\ell}'(\boldsymbol{\ell}-\boldsymbol{\ell}')\right]^{2} C_{\ell'}^{TE} C_{|\ell-\ell'|}^{\phi\phi}\cos^{2}2(\gamma_{\ell'}-\gamma_{\ell}) \\ \tilde{C}_{\ell}^{BB} &\approx \int \frac{d\ell}{(2\pi)^{2}}\left[\boldsymbol{\ell}'(\boldsymbol{\ell}-\boldsymbol{\ell}')\right]^{2} C_{\ell'}^{EE} C_{|\ell-\ell'|}^{\phi\phi}\sin^{2}2(\gamma_{\ell'}-\gamma_{\ell}) \end{aligned} \quad (1.39)$$

where γ_{ℓ}, $\gamma\ell'$ are the angles between $\hat{\mathbf{n}}$ and ℓ, ℓ' respectively. The results above are neglecting the contribution to lensing of the primordial $B-$modes, which are expected to be small. Despite the absence of primordially generated $B-$modes, lensing induces a power spectrum in this component of polarisation from the unlensed $E-$modes. On large scales it has an amplitude which is independent of ℓ, as it can be seen in Fig. 1.8. This can be easily derived from Eq. 1.39 in the limit $|\boldsymbol{\ell}| << |\boldsymbol{\ell}'|$. Since the lensed $B-$modes result from a convolution of primordial $E-$modes in the harmonic domain the contributions to the lensing $B-$modes power come from all multipoles where there is non-zero E and lensing potential power. It is important to note that the $B-$modes generated from the lensing of $E-$modes can potentially

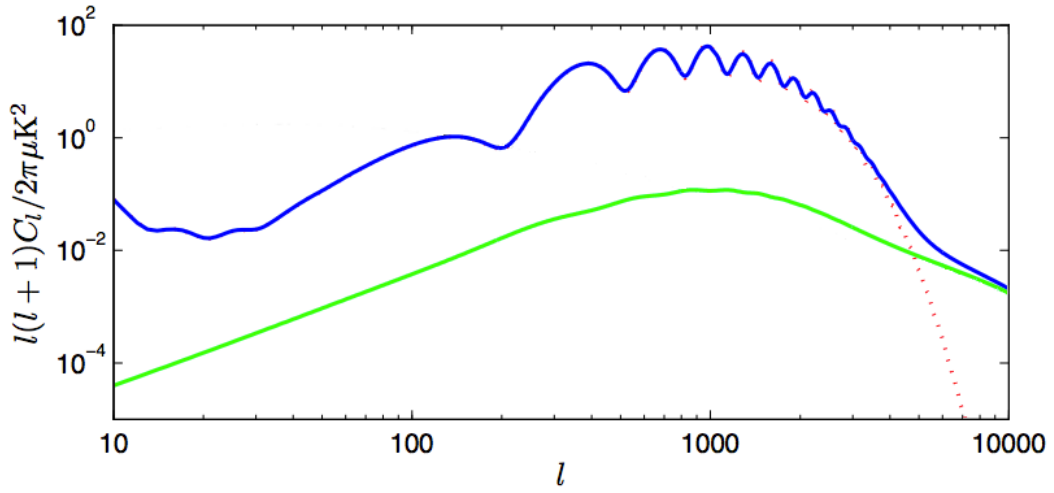

Figure 1.8: The lensed E (top solid) and lensed B (bottom solid) power spectra, compared to the unlensed E spectrum (dotted). Figure adapted from [26].

be a contaminant for the detection of the primordial $B-$modes signal generated by the gravitational waves coming from inflation [33, 34, 1]; this topic will be discussed in more detail in Chapter 3. The effect of lensing on the $E-$modes is similar to the effect on temperature as the convolution with the lensing potential smooths out the acoustic peaks and troughs of the power spectrum. Since polarisation peaks are sharper than in the temperature case, this means that the effect of lensing is quantitatively more important on the E polarisation spectrum. On very small scales, the unlensed polarisation is damped, as in the temperature case, and lensing transfers power from large to small scales, therefore in this part of the spectrum we expect to observe the same power in both E and B polarisation (see again Fig. 1.8).

1.5 Status of observations

As CMB lensing is a second order effect on the angular power spectrum of the primary anisotropies, its detection has been out of reach until very recent times, despite its relevance as a cosmological probe was already known in the scientific community since it was first proposed in 1987 [35]. The first hints of a non-zero lensing signal were found in the WMAP[3] data [36, 37], which underlined evidence of a correlation of CMB with large scale structure tracers. The first direct indication of a preference for a lensed CMB power spectrum with respect to an unlensed one

[3]Wilkinson Microwave Anisotropy Probe

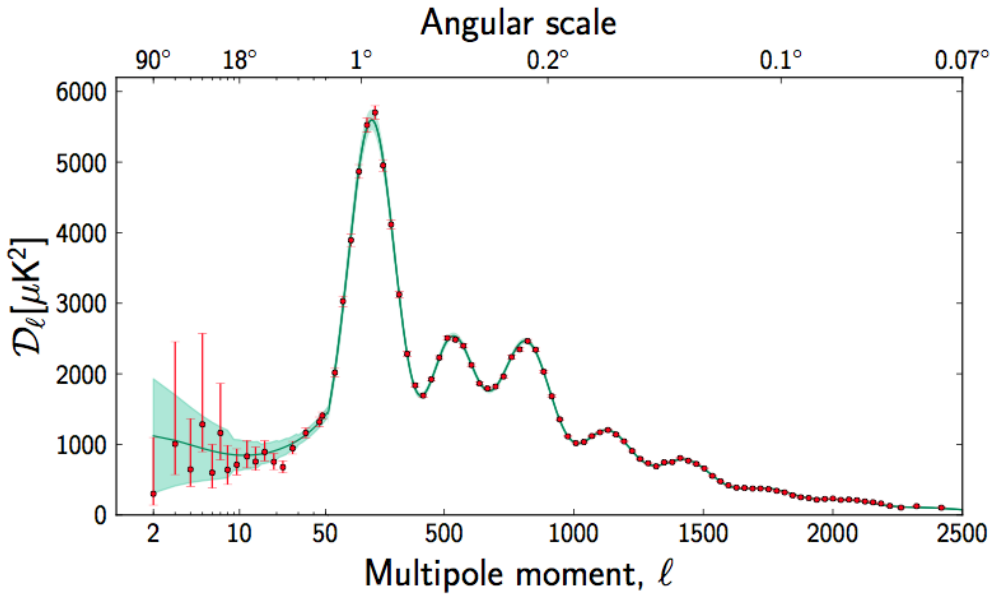

Figure 1.9: The 2013 PLANCK CMB temperature angular power spectrum. The error bars include cosmic variance, whose magnitude is indicated by the green shaded area around the best fit model. The ΛCDM framework provides an excellent model for most of the PLANCK data. Figure from [40].

were found in the ACBAR[4] data [38], but for a proper reconstruction of the lensing power spectrum, high sensitivity small scale CMB experiments like ACT [3] and SPT [4] have been necessary.

The lensing spectrum from the large scales on the sky has been delivered for the first time by the PLANCK experiment in the first scientific data release [5]; the POLARBEAR collaboration has reported a first direct detection of CMB lensing from polarised CMB [7] as well as a measurement of the cross-correlation of CMB lensing and the Cosmic Infrared Background (CIB) [39].

At the present day, not only CMB lensing has been detected both in temperature and polarisation power spectra; a continuous effort in creating new algorithms, searching for alternative models of gravity and galaxy formation, and developing innovative techniques for simulating lensed maps is being carried out for a full characterisation and cosmological exploitation of this observable.

In the following, the current state of the art about detection and measurements of CMB lensing will be reviewed.

1.5.1 Planck

The PLANCK experiment [41] delivered in 2013 all-sky temperature maps with unprecedented sensitivity, setting a milestone for the status of our understanding

[4]Arcminute Cosmology Bolometer Array Receiver

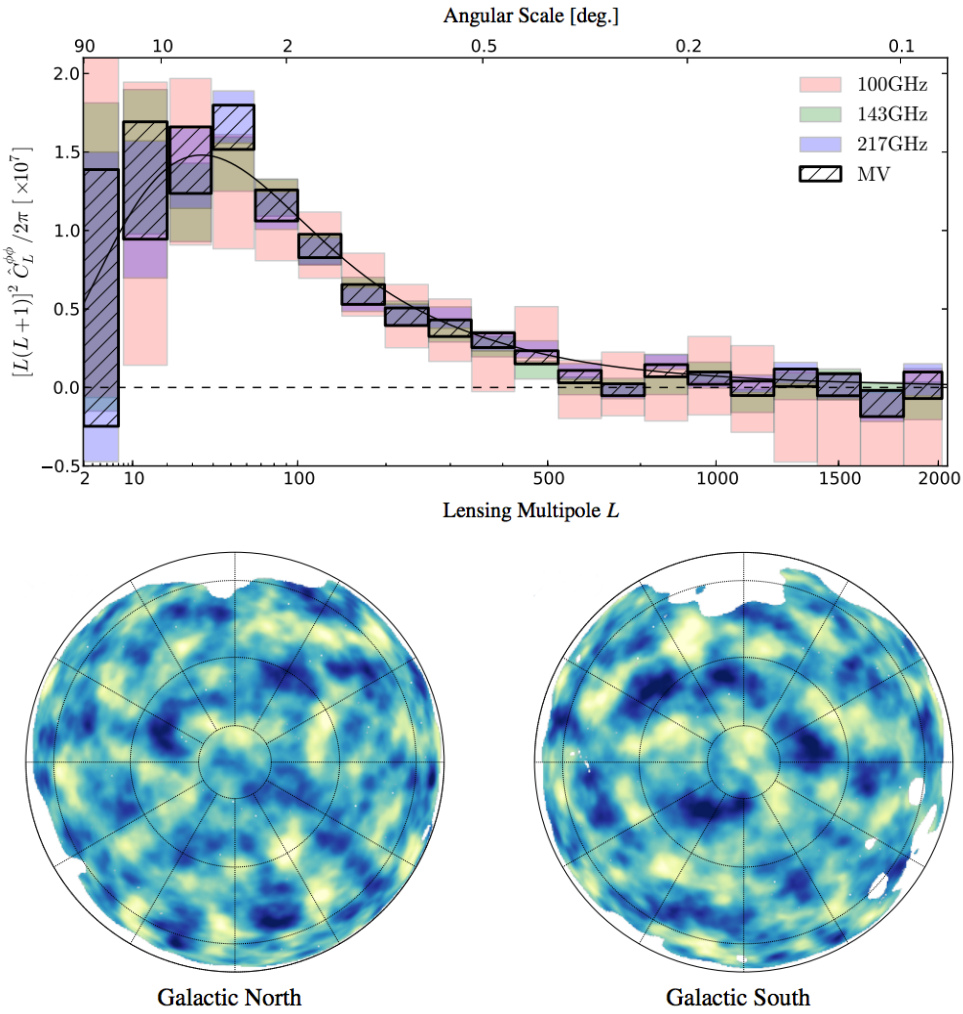

Figure 1.10: Top: Lensing potential power spectrum estimates based on the individual 100, 143, and 217 GHz sky maps. The black line is for the best-fit ΛCDM model. MV is the Minimum Variance estimator built using data from the aforementioned channels. Bottom: Wiener-filtered lensing potential estimate form the PLANCK maps in Galactic coordinates. Figures from [5].

of the Universe. The full power spectrum from temperature is shown in Fig. 1.9. These results have a great importance not only for the cosmology, but also for astrophysics, allowing to characterise not only the cosmological signal, but also the foreground astrophysical emission. Given the huge amplitude of the results yielded by the mission, the full results will not be reviewed here, focusing on the analysis lead on gravitational lensing of the CMB; the full analysis on the allowed values of cosmological parameters can be found in [13].

The PLANCK dataset allowed to reconstruct from the temperature maps for the first time not only the CMB lensing power spectrum but also the lensing potential maps (see Fig. 1.10). The lensing power spectrum data were used in combination with the CMB data to tighten constraints on cosmological parameters and break

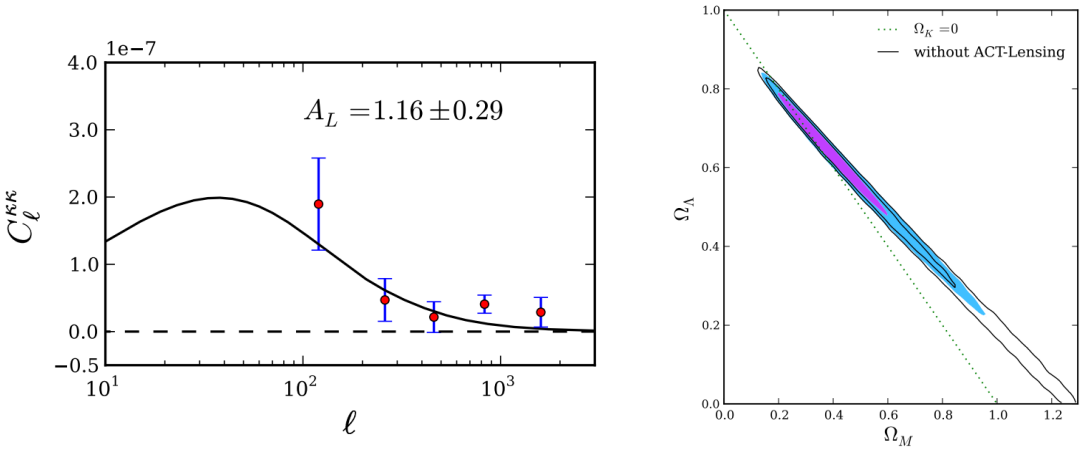

Figure 1.11: Left: Convergence power spectrum (red points) measured from ACT equatorial sky patches. The solid line is the power spectrum from the best-fit WMAP+ACT cosmological model, which is consistent with the measured points. Figure from [3]. Right: 2-D marginalised posterior probability for Ω_m and Ω_Λ. 1σ and 2σ contours are shown. Purple and blue contours consider the combination WMAP+ACT while black are for WMAP alone. The combination WMAP+ACT, which takes into account lensing data, favours a Universe with a non vanishing CC. Figure from [10].

underlying degeneracies. The reconstructed lensing potential power spectrum is found to be in good agreement with the ΛCDM prediction; the data show an evidence for a non-zero lensing effect with a 20σ confidence level [5].

To give an example of the cosmological interest of taking the information coming from CMB lensing into account, let us just note that the geometric degeneracy between DE and spatial curvature can be broken, as for instance models of closed Universe with low density of DE would produce an identical unlensed power spectrum to the ΛCDM case. The power spectrum of lensing, on the other hand, will be different, thus breaking the degeneracy. This characteristic, for PLANCK data, allows to pose simultaneous constraints on $\Omega_k = -0.0096^{+0.010}_{-0.0082}$ and $\Omega_\Lambda = 0.67^{+0.027}_{-0.023}$. This topic will be treated more extensively in Chapter 3.

1.5.2 ACT

The ground-based experiment ACT, located in Atacama desert, [42] is, with SPT, the most sensitive and highest resolution CMB temperature experiment currently operating. Both these experiments have measured the damping tail of the CMB spectrum up to ℓ of order of a few thousands, providing new insights into secondary CMB anisotropies and extragalactic point source populations that dominate the signal at small angular scales. ACT has been the first experiment to detect, at 4σ confidence level, the gravitational lensing of the CMB through a measurement of the four-point correlation function in the temperature maps [3], as shown in Fig. 1.11, left panel.

The high significance detection of CMB lensing potential also allowed for the

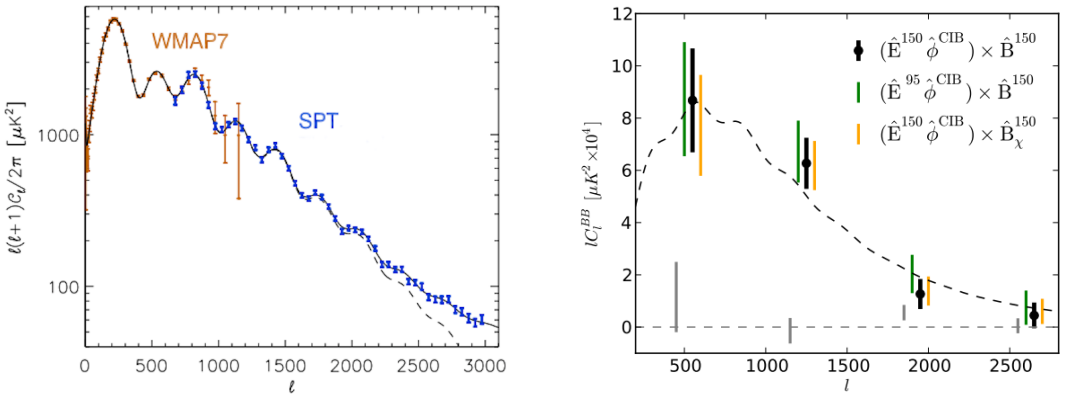

Figure 1.12: Left: The SPT bandpowers, WMAP bandpowers, and best-fit ΛCDM theory spectrum shown with dashed (CMB) and solid (CMB+foregrounds) lines The excess visible at $\ell \gtrsim 2300$ is due to residual foreground sources. Figure from [4]. Right: In black, the cross correlation of the lensing $B-$modes measured by SPTpol at 150 GHz with lensing $B-$modes inferred from CIB fluctuations measured by HERSCHEL and $E-$modes measured by SPTpol at 150 GHz. In green, same as black, but using $E-$modes measured at 95 GHz, testing both foreground contamination and instrumental systematics. In orange, same as black, but with $B-$modes obtained using the χ_B procedure described in [43]. In grey, the curl-mode null test. The dashed black curve is lensing $B-$mode power spectrum in the ΛCDM model. Figure from [6].

first time to probe the presence of a non vanishing CC using only CMB data [10], see right panel of Fig. 1.11.

1.5.3 SPT

As already said, SPT [44] is a ground-based experiment located at the South Pole, which together with ACT delivered high precision CMB maps in the small scales region of the angular power spectrum.

Using only the power spectrum of the SPT temperature data, shown in Fig. 1.12, gravitational lensing of the CMB is detected at 5σ significance [4] while the reconstruction of the convergence power spectrum using the four-point correlation function and the all-ℓ technique gave a 6.3σ detection of gravitational lensing [45]. In [46], it is further proved that adding the SPT data to the WMAP measurements improves the precision of different cosmological parameters including the possibility of breaking of the angular diameter distance degeneracy.

In 2013, a detection of gravitational lensing $B-$modes using first-season data from the polarisation-sensitive receiver on the South Pole Telescope SPT-pol (the observation strategy, calibration, and data reduction are similar to those used in [47]) and data from the infrared background provided by the HERSCHEL experiment was presented in [6]. After constructing a template for the lensing $B-$mode signal by combining E-mode polarisation measured by SPT-pol with estimates of the lensing potential from a HERSCHEL-SPIRE map of the CIB [48], it is compared to the $B-$modes measured directly by SPT-pol, with an indication for a non-zero

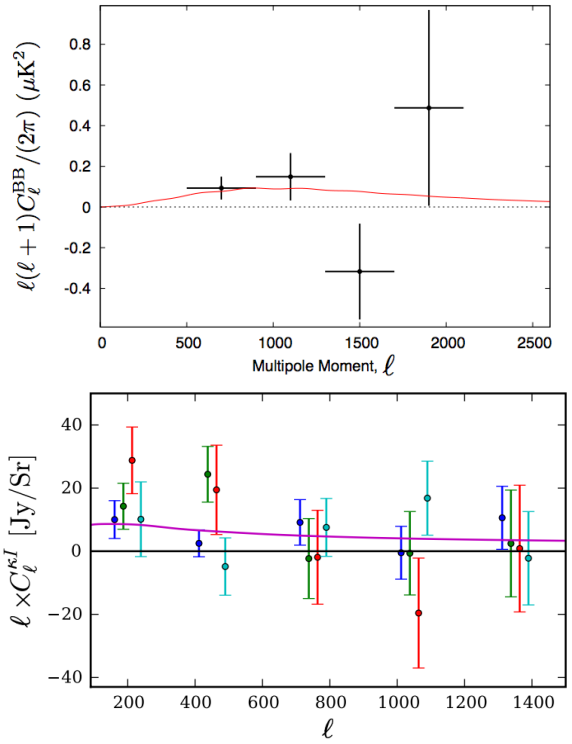

Figure 1.13: Top panel: A single estimate of the C_ℓ^{BB} power spectrum from the three POLARBEAR patches is created using the individual patch band powers and their covariance matrices. In red, the theoretical WMAP 9 years ΛCDM high-resolution C_ℓ^{BB} spectrum is shown. The uncertainty shown for the band powers is the diagonal of the band power covariance matrix, including beam covariance. Figure from [7]. Bottom panel: all four combinations of the two lensing estimators (EE, EB) applied to two different POLARBEAR maps and cross-correlated with the overlapping HERSCHEL fields. The fiducial theory curve for the lensing-CIB cross-correlation spectrum is also shown (solid line). Figure from [39].

correlation at 7.7σ significance (see again Fig. 1.12).

1.5.4 POLARBeaR

With respect to the other experiments described up to now, whose first target is the accurate measurement of the temperature spectrum at very small scales, the POLARBEAR experiment [49] was designed to specifically detect the $B-$modes of CMB polarisation on both large and small angular scales, in a range $25 < \ell < 2500$; the experiment is placed at the South Pole as for the case of SPT.

Recently, a measurement of the $B-$modes polarisation power spectrum covering the angular multipole range $500 < \ell < 2100$ based on observations of 30^{o2} of the sky with 3.5' resolution at 150 GHz was presented [7]. Including both systematic and statistical uncertainties, the hypothesis of no $B-$mode polarisation power from gravitational lensing is rejected at 97.5% confidence, and the band powers are found to be consistent with the standard cosmological model, see Fig. 1.13.

This measurement represents the first detection of lensing in the polarisation spectrum, and in particular the first direct detection of the $B-$modes of CMB polarisation at small scales, and demonstrates the possibility of future exploitation of CMB $B-$mode polarisation as a probe of both structure formation and the inflationary epoch.

In another recent work [39] the gravitational lensing convergence signal from CMB polarisation data taken by the POLARBEAR experiment and cross-correlated with CIB maps from the first data release from the HERSCHEL-Atlas survey [50] was presented, see again Fig. 1.13. From the cross-spectra, evidence for gravitational lensing of the CMB polarisation at a statistical significance of 4.0σ and for the presence of a lensing $B-$mode signal at a significance of 2.3σ are obtained.

Such measurements of polarisation lensing, made via the robust cross-correlation channel, not only reinforce auto-correlation measurements, but also represent one of the early steps towards establishing CMB polarisation lensing as a powerful new probe of cosmology and astrophysics.

2

Relevance of ΛCDM extensions in the recent expansion history

Until a few decades ago, the presence of a DE component in the Universe was not only debated, but also not accepted by the majority of the cosmological community. By the mid-1990s, Big Bang cosmology was convincingly established, but the Einstein-de Sitter model (a model with no curvature, and containing matter only) was showing numerous cracks, under the combined onslaught of data from the CMB, large scale galaxy clustering, and direct estimates of the matter density, the expansion rate H_0, and the age of the Universe; introducing a cosmological constant offered a potential resolution of many of these tensions. In the late 1990s, SuperNova (SN) surveys by two independent teams provided direct evidence for accelerating cosmic expansion [51, 52], establishing the ΛCDM as the preferred alternative to the $\Omega_m = 1$ scenario.

CMB evidence for a spatially flat Universe cemented the case for cosmic acceleration by firmly eliminating the expansion-free alternative with $\Omega_m < 1$ and $\Omega_\Lambda = 0$. Today, the accelerating Universe is well established by multiple lines of independent evidence from a tight web of precise cosmological measurements.

Despite the huge success of the current status of the model, for its predictive power and the excellent agreement with observations, some crucial issues still remain open: the nature of DE is still unknown, as well as its behaviour in time and space. This leaves room for studying extensions of the standard CC case, in order to seek for deviations from the standard Equation of State (EoS) $w = -1$, that will be investigated in Sec. 2.1, which might hint at different evolution histories of DE. In this regard, the ultimate knowledge will be reached by exploiting fully the EUCLID data. The mission, with foreseen launch date in 2020, will use cosmological probes to investigate the nature of DE, DM and gravity by tracking their observational signatures on the geometry of the Universe and on the cosmic history of structure formation. EUCLID will map LSS over the redshift range $0.3 \lesssim z \lesssim 5$, corresponding to a cosmic time covering the last 10 billion years, more than 75% of the current age of the Universe [11].

Another extension of standard physics which has interesting implications in cosmology is the inquiry for understanding the characteristics of neutrinos. Measurements of the CMB alone have led to a constraint on the effective number of neutrino species of $N_{eff} = 3.36 \pm 0.34$ [13], a value 10σ away from zero and consistent with expectations. Planned and underway experiments are prepared to

study the Cosmic Neutrino Background (CNB), resulting from the decoupling of neutrinos from the rest of matter, via its influence on distance-redshift relations and the growth of structure. Future experiments, including upcoming spectroscopic surveys EBOSS [53] and DESI [54] and a new Stage-IV CMB polarisation experiment CMB-S4, will be able to achieve a precision on the sum of neutrino masses of 16 meV and on the number of neutrino species of $N_{eff} = 0.020$. Such a mass measurement will produce a high significance detection of non-zero $\sum m_\nu$, whose lower bound derived from atmospheric and solar neutrino oscillation data is about 58 meV. If neutrinos have a normal mass hierarchy, this measurement will definitively rule out the inverted neutrino mass hierarchy, shedding light on one of the most puzzling aspects of the Standard Model of particle physics - the origin of mass. The role of neutrinos in the SM and in cosmology will be outlined in 2.2.

Such measurement of N_{eff} will allow for a precision test of the standard cosmological model prediction that $N_{eff} = 3.046$. The difference from three is due to the small amount of entropy from electron/positron annihilation that gets transferred to the neutrinos; N_{eff} is by design equal to three in the idealised case that all of this entropy is transferred to photons. Finding N_{eff} consistent with 3.046 at a high precision level would demonstrate that we understand very well the thermal conditions in the Universe just one second after the Big Bang. On the other hand, finding N_{eff} significantly different from 3.046 would be a signature of new physics.

The effects of neutrino properties on cosmology precisely appear in many observables in diverse ways, and are clearly observationally distinguishable from the effects of other cosmological parameters. Much of the sensitivity to $\sum m_\nu$ will come from measurements of the gravitational lensing of the CMB, measurements of the Baryon Acoustic Oscillation (BAO) features [55] and broadband power spectrum, and measurements of weak gravitational lensing of galaxies; it is relevant to consider different combinations of these probes, as they have completely independent systematic errors.

In this Chapter, DE (in Sec. 2.1) and the influence of neutrinos on cosmology (in Sec. 2.2) will be reviewed, with the aim of showing how these two phenomena can be relevant and worthy to be considered in a view of expanding the current knowledge of physics beyond the ΛCDM and the standard model of particle physics, and how it is possible to learn more about the relevant observables by which they are characterised using CMB lensing and other cosmological observables.

2.1 Cosmological Constant and Dark Energy

Among the solutions of Friedmann equations that are relevant for present day cosmology, an important role is played by the class of solutions including the presence of a CC. According to current available cosmological data, we identify three major components in the Universe: the baryonic matter with associated density Ω_b, the total matter, with density Ω_m, which includes the baryonic matter and the DM

components, and the DE, with energy densityΩ_Λ, which were defined in Sec. 1.2. Since from CMB we know that the Universe is very close to flatness $\Omega_k = 0$, and the sum of all baryonic and dark matter in the Universe takes into account at most for the 30% of the overall energy/matter, DE is nowadays the dominating component in the Universe and accounts for the missing energy density. The DE density is often thought to be connected to the possible existence of a CC or vacuum energy. The CC was first introduced by Einstein while looking for a static solution of Friedmann equations. For this purpose he introduced the addition of another geometrical component proportional to the metric to the field equations:

$$R_{\mu\nu} - \frac{1}{2}g_{\mu\nu} + \Lambda g_{\mu\nu} = 8\pi G T_{\mu\nu} \tag{2.1}$$

This implies that the Friedmann equations are modified as follows:

$$\begin{aligned} \left(\frac{\dot{a}}{a}\right)^2 = \frac{8\pi G}{3}\rho - \frac{k}{a^2} \quad &\Rightarrow \quad \left(\frac{\dot{a}}{a}\right)^2 = \frac{8\pi G}{3}\rho - \frac{k}{a^2} + \frac{\Lambda}{3} \\ \frac{\ddot{a}}{a} = -\frac{4\pi G}{3}(3p+\rho) \quad &\Rightarrow \quad \frac{\ddot{a}}{a} = -\frac{4\pi G}{3}(3p+\rho) + \frac{\Lambda}{3}. \end{aligned} \tag{2.2}$$

The modern point of view on the CC problem attempts to reach beyond the original geometrical hypothesis of Einstein and considers the CC as the result of the minimum energy state being at a non-zero level in Quantum Field Theory (QFT). By moving the CC term on the right hand side of Eq. 2.1 it is clear that this "vacuum energy" component behaves like a perfect fluid with an EoS $p = w\rho$ with $w = -1$. Such fluid has a constant energy density, while both matter and radiation energy density decay over time, the Ω parameters are given by

$$\Omega_\Lambda = \frac{\Lambda}{8\pi G H^2} \;\; , \;\; \Omega_m = \frac{3\rho_m}{8\pi G H^2 a^3} \;\; , \;\; \Omega_\gamma = \frac{3\rho_\gamma}{8\pi G H^2 a^4}. \tag{2.3}$$

From the above expressions in Eqs. 2.2, it follows that in a Universe with no matter or radiation components, the second order derivative of the scale factor is positive, meaning that the expansion will be accelerated. This regime is also reached at late times, as the energy-density connected to the CC tends therefore to dominate over matter and radiation energy density at late times, since the two latter components decrease in density as the Universe expands.

When the Universe becomes dominated by the CC, the expansion becomes exponentially accelerated:

$$\frac{\ddot{a}}{a} = \frac{\Lambda}{3} \Rightarrow a \propto \exp\left(\frac{\Lambda}{3}t\right)^{\frac{1}{2}}. \tag{2.4}$$

In Fig. 2.1 different evolution histories of the Universe during time can be seen depending on the combination of values of the cosmological parameters: in particular, one can see that a flat Universe containing matter only will expand at a decreasing rate, while a flat Universe with an energy contribution from a non-vanishing CC starts to expand at an accelerated rate as time progresses.

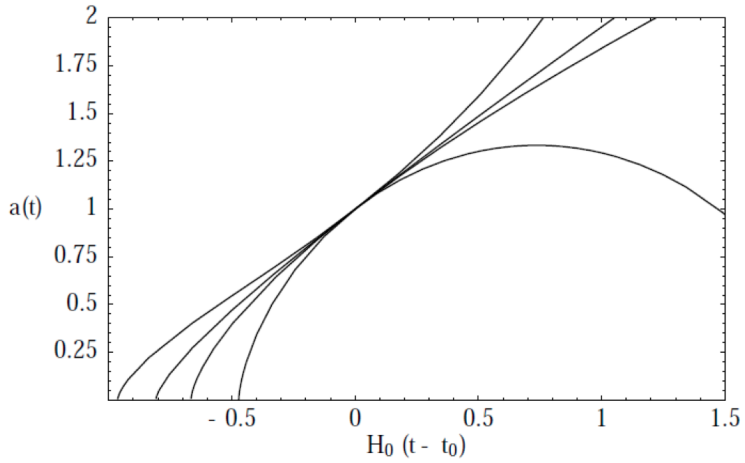

Figure 2.1: Expansion histories for different values of Ω_m and Ω_Λ. From top to bottom $(\Omega_m, \Omega_\Lambda) =$ (0.3, 0.7), (0.3, 0.0), (1.0, 0.0), (4.0, 0.0). Figure from [56].

Being w the ratio of pressure to energy density, it is also closely connected to the underlying physics. Despite the fact that the recent acceleration of the Universe is now a well-established phenomenon, the absence of a consensus model for cosmic acceleration presents a challenge in trying to connect theory with observations. If cosmic acceleration is due to new gravitational physics, the motivation for a description in terms of a constant value of w disappears; for example, this assumption does not describe scalar field or modified gravity models.

A more general treatment than adopting a constant value of $w = -1$, which provides a useful phenomenological description but does not describe a possible evolution of the energy density during time and space, is to consider a scalar filed rather than a constant. This scalar field, also known as *quintessence*, exhibits a dynamic behaviour in time as well as spatial fluctuations, and may possibly be coupled to Dark Matter [57] or to the gravitational interaction [58, 59]. For this work, we will be concerned with the time evolution of the EoS during time, see also Chapter 3.

By considering the continuity equation, we can compute the evolution of the energy density if we consider a general EoS

$$\begin{aligned} \frac{d\rho}{dt} &= -3(\rho + p)\frac{1}{a}\frac{da}{dt} \Rightarrow \frac{d\rho}{dt} = -3\rho(1+w)\frac{1}{a}\frac{da}{dt} \\ \Rightarrow \rho &= \rho_0 \exp\left(3\int_a^1 \frac{[1+w(a')]}{a'}da'\right). \end{aligned} \tag{2.5}$$

Among many possible choices for the parametrisation of the EoS, some lead to unrealistic behaviour, e.g. $w >> -1$ or $w << -1$. The parametrisation [60, 61], often referred to as Chevallier-Polanski-Linder (CPL)

$$w(a) = w_0 + w_a(1-a) = w_0 + w_a\left(\frac{z}{1+z}\right) \tag{2.6}$$

avoids this problem and leads to the most commonly used description of DE, involving three parameters Ω_{DE} the DE density at present, w_0 the value of the EoS today, and w_a represents the first order expansion in terms of the scale factor. This parametrisation does not inquire the physical nature of the variation of the DE density over time; despite this, it is a useful phenomenological tool to study possible deviations from a CC, in particular when considering more exotic models predicting a departure from $w = -1$.

The most recent constraints on the evolution of the EoS have been presented by the PLANCK Collaboration in [13]; for constraints on more exotic models, PLANCK data have been analysed in detail in [62].

The next step for constraining DE and matter clustering in general in the era of precision cosmology is represented by the EUCLID mission, conceived to measure the expansion history and growth of LSS with a precision that will allow us to distinguish time-evolving DE models from a CC, and to test the theory of gravity on cosmological scales.

The mission will directly map the DM distribution in the Universe through weak gravitational lensing by imaging 1.5 billion galaxies and providing near infrared photometry. At the same time, it will carry out a spectroscopic redshift survey of 50 million galaxies over a volume 500 times larger than the Sloan Digital Sky Survey [11].

Thanks to the information in redshift, the EUCLID datasets will be exploited to constrain the time evolution of structures, expanding our knowledge on the whole dark sector of the Universe. The process of clustering, measured at an unprecedented precision, will test our knowledge of the theory of gravity, via the quantifying of the growth factor γ, which quantifies the efficiency with which structure is built up in the Universe as a function of redshift. Using weak lensing and galaxy clustering, the sensitivity on the DE parameters w_0, w_a are forecasted to reach values of $\sigma_{w_0} = 0.05, \sigma_{w_a} = 0.16$, giving a final answer on the evolution of DE [63].

2.1.1 Experimental evidences for Dark Energy

We have seen how adding a CC to the Einstein field equations determines an accelerated expansion phase of the Universe as the scale factor drops significantly; in order to establish the presence or absence of such an energy component in the Universe, whose existence can be only inferred indirectly through its effects on cosmological evolution, we need too find observables suitable for investigating the matter.

Looking again at the Friedmann equations (Eqns. 2.2), it is possible to calculate from the first one the age of the Universe as a function of the different abundances of the cosmological species, while the second one allows to analyse the effect of an accelerated expansion on the luminosity distance and to compare the theoretical calculations with observational data.

A lower limit to the age of the Universe can be placed dating the oldest known stars, such as the low metallicity stars inside globular clusters. Studying their

evolutionary stage, the age of Universe is constrained to be [64]

$$t_0 > 13.5 \pm 2 \text{ Gyrs.} \tag{2.7}$$

Let us now calculate theoretically the time t_0 from the Big Bang (when $a = 0$) to the present time; this will vary as a function of the cosmological parameters. Considering a flat Universe composed by matter only $\Omega_m = 1$, solving the first Friedmann equation gives

$$\left(\frac{H}{H_0}\right)^2 = \frac{1}{a^3} \Rightarrow \sqrt{a}\, da = H_0\, dt. \tag{2.8}$$

Integrating between $0 < t < t_0$ and $0 < a < 1$, and assuming $H_0 \simeq 70$ km/(s Mpc) we find

$$t_0 = \frac{2}{3} {H_0}^{-1} \approx 9.3 \text{ Gyrs.} \tag{2.9}$$

Therefore, if non-relativistic matter is the only component of the Universe, the predicted age is too small to agree with the age of globular clusters. If one considers a Universe composed only by radiation, the resulting age of the Universe would be $t_0 = (2H_0)^{-1} \approx 7$ Gyrs. For this reason it is not possible to account for the observed age of the Universe with matter and radiation as the only components present in the Universe. If we now calculate the age of a flat Universe composed by matter and with a non-vanishing CC ($\Omega_\Lambda = 1 - \Omega_m$), we obtain

$$t_0 = \frac{2}{3} \frac{{H_0}^{-1}}{\sqrt{1-\Omega_m}} \ln \left[\frac{\sqrt{1-\Omega_m}+1}{\sqrt{\Omega_m}} \right]. \tag{2.10}$$

If we set $\Omega_m = 0.25$ and $H_0 \simeq 70$ km/(s Mpc) we obtain $t_0 \approx 14.2$ Gyrs; this shows that a model with a matter content and a CC whose energy densities are comparable, is in agreement with the lower age limit obtained by the observations of globular clusters.

The cosmological evidence of the current accelerated expansion of the Universe was made possible by accurate distance measurements of SuperNovae (SNe) [52]. This class of exploding stars was first studied extensively during the first half of the XX century by Zwicky and his collaborators, who first pointed out that these luminous outbursts can be classified into different types according to their optical spectra and their light curve. In particular, SNe classified as type Ia (SNe Ia), which show no Hydrogen and Silicon lines in their spectra, appeared to be a physically distinct class from the other SNe. Stellar evolution theory identifies this type of objects as the result of the thermonuclear explosion of white dwarfs accreting mass from a binary companion approaching the Chandrasekhar mass limit. On the other hand, other types of SNe are generated from the core collapse of evolved massive stars.

Even though the mechanism which triggers the explosion is still uncertain, SNe Ia appear to have homogeneous observational properties in terms of spectral features, rate and decay times. In the effort of building a further step of the distance

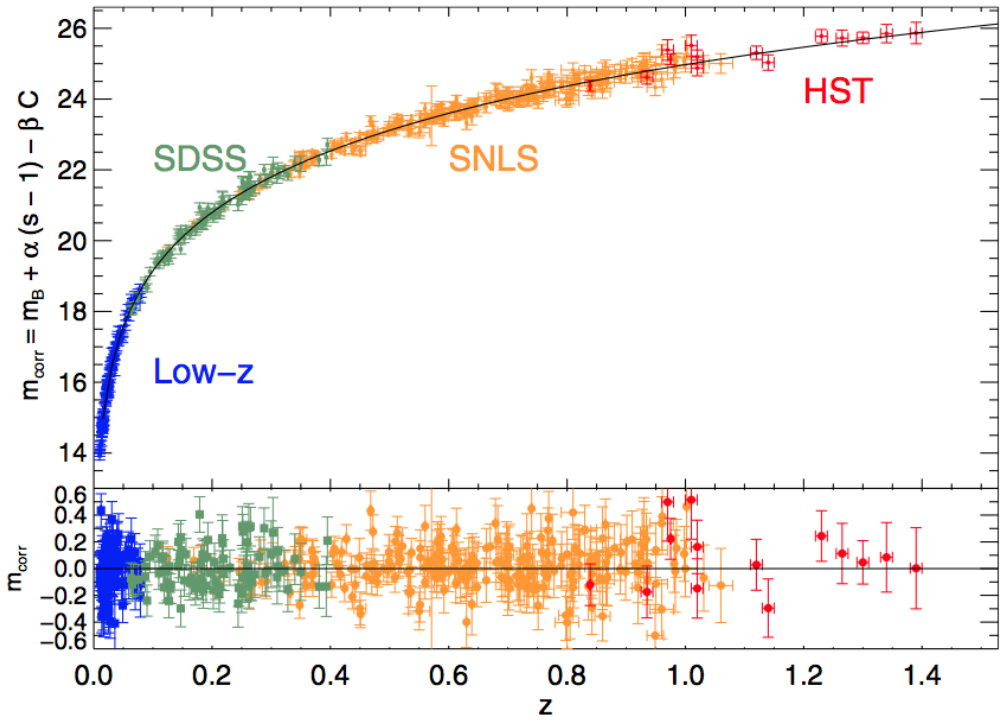

Figure 2.2: State of the art of luminosity distance measurements using SNe Ia in terms of apparent magnitude (top) and residuals from the best fit cosmological model (bottom) using data from different surveys. Thanks to the good statistics accumulated, the uncertainties on the cosmological parameter estimations from SNe measurements are now dominated by systematic errors. Figure from [65].

ladder, it has been possible to establish the correlation between the peak brightness of SNe Ia and the decline rate of the luminosity after the peak [66], making then the SNe Ia "standardizable" candles for distance measurements.

The measured energy flux f of the light emitted by a source having an intrinsic luminosity L is reduced by the expansion of the Universe which redshifts the photon energy and of the emitted photons and delays their arrival time. Since the expansion history of the Universe depends on the cosmological parameters it is possible to connect distance measurements of objects which have the same intrinsic luminosity to the underlying cosmology. The quantity encoding the dependency on the cosmological parameters is the luminosity distance $D_{L_*} = D_{L_*}(z, \Omega_m, \Omega_\Lambda, w)$ which is connected to the observed flux of a source as

$$f = \frac{L}{4\pi {D_{L_*}}^2}. \tag{2.11}$$

In case of a Universe dominated by a CC, the expression for the luminosity distance

reads [21]

$$D_{L_*}(z,\Omega_m,\Omega_\Lambda,w) \propto \frac{1+z}{H_0\sqrt{|\Omega_k|}} \int_{\frac{1}{1+z}}^{1} \frac{\sqrt{|\Omega_k|}}{a^2\sqrt{\Omega_m a^{-3}+\Omega_\Lambda+\Omega_k a^{-2}}} da. \tag{2.12}$$

For standard candles with known spectra, the measurements of $D_L(z)$ are able to constrain the cosmological parameters. This can be done directly for low redshift SNe, which will be used to calibrate the observation of farther objects whose absolute luminosity is unknown.

2.1.2 Fine tuning and coincidence problem

Despite the good agreement with data and the interest, the CC suffers a few theoretical problems, mainly the coincidence and fine tuning problems. The first problem arises from the fact that the energy densities of matter and CC are comparable at present time, even if their ratio changes quickly with time:

$$\frac{\rho_\Lambda}{\rho_m} = a^3. \tag{2.13}$$

At past times in fact, matter energy density was strongly dominant with respect to the energy density given by the CC, for example at Planck time $t_P = \sqrt{G} = 5.3906 \cdot 10^{-44}$ s after the Big Bang, their ratio was $\frac{\rho_\Lambda}{\rho_m} \approx 10^{-123}$. Knowing from the first Friedmann equation how the two components evolve with redshift, we can calculate the redshift z_T where the contributions of matter and CC become equivalent:

$$(1+z_T) = \left(\frac{\Omega_\Lambda}{\Omega_m}\right)^{\frac{1}{3}} \Rightarrow z_T \approx 0.4 \tag{2.14}$$

Thus, the equivalence between the two species happened really close to the present time from a cosmological point of view, but there is no physical mechanism able to predict the transition from the matter to the CC dominated regime, as the latter has a constant energy density. Therefore the value of the CC is exactly the one needed to switch at present time from the past matter-dominated regime to the period of CC dominance, but there is no way to explain why we are living in such a special moment of the life of the Universe.

Another issue concerning the CC arises from its physical interpretation; this component in fact behaves like a fluid whose energy density keeps constant as the Universe expands. For this reason, one can think that the CC is connected with vacuum energy, which obeys the same property. It is possible to show that the vacuum energy behaves like a CC, as computing the mean value of the stress-energy tensor on the vacuum state in Minkowski space-time, we obtain an invariant symmetric tensor, thus proportional to the metric. This applies also to curved space-times if we neglect higher order terms, therefore

$$\langle T_{\mu\nu}\rangle_{vac} = \rho_{vac}\, g_{\mu\nu}. \tag{2.15}$$

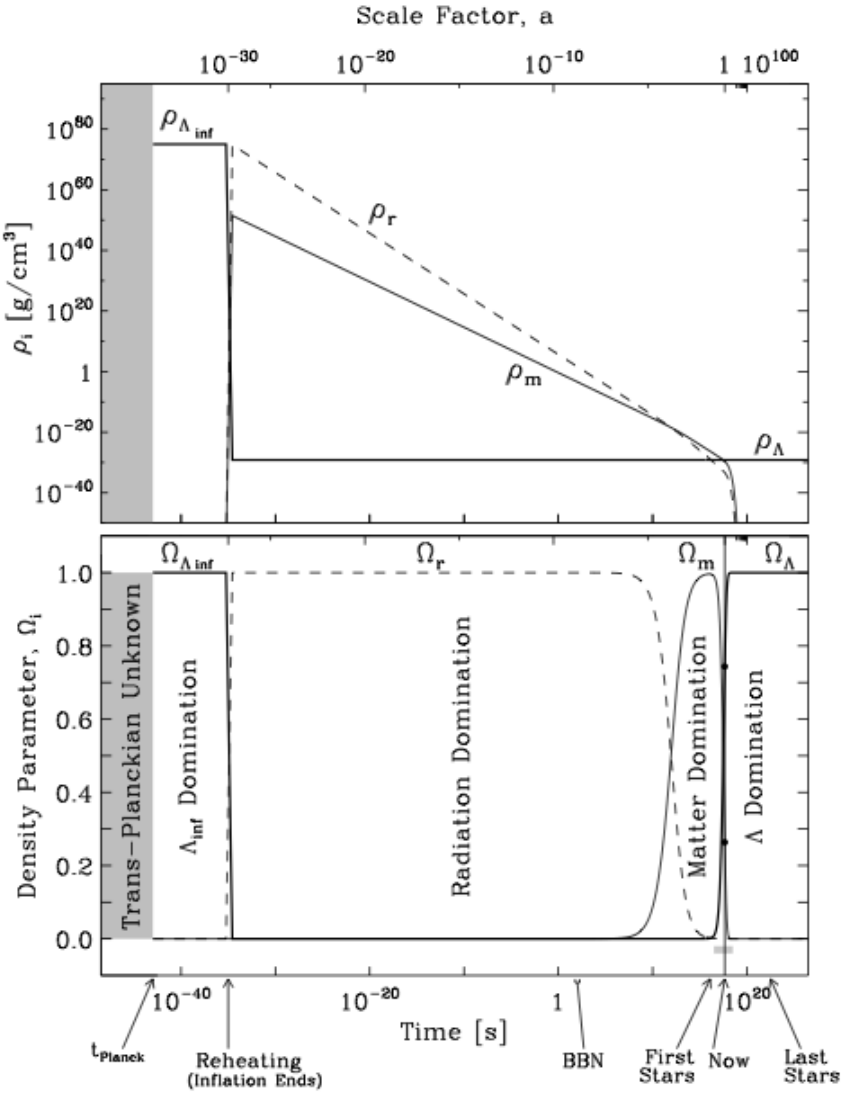

Figure 2.3: Time dependence of the densities of the major components of the Universe. Given the observed Hubble constant, H_0 and energy densities in the Universe today (Ω_r radiation, Ω_m matter, and Ω_Λ CC), the Friedmann equation is used to plot the temporal evolution of the components of the Universe in g/cm^3 (top panel), or normalised to the time-dependent critical density ρ_{crit} (bottom panel). Figure from [67].

The effective CC which enters the Friedmann equations is given by [68]

$$\Lambda = 8\pi G\rho_{vac} + \Lambda_0, \tag{2.16}$$

where Λ_0 is a bare CC in Einstein's field equations. We know that, as the Universe is flat, $\rho_\Lambda \equiv \Lambda/8\pi G$ cannot exceed the critical energy density ρ_c:

$$\rho_\Lambda < \rho_c = \frac{8{H_0}^2}{8\pi G} \approx 8 \cdot 10^{-47}{h_0}^2 \text{ GeV}^4. \tag{2.17}$$

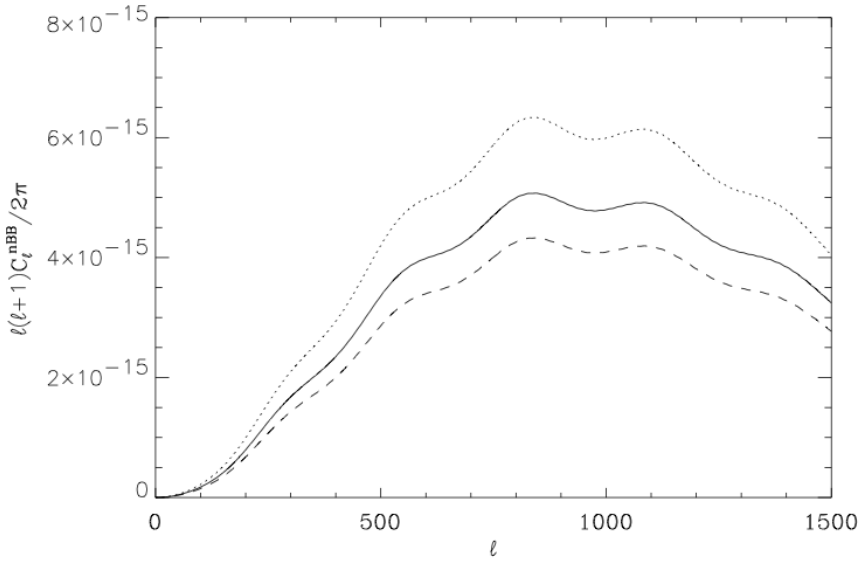

Figure 2.4: Lensed $B-$modes power spectra for DE models with a time-varying EoS. The curves represents models with $w_0 = -0.9$, $w_a = 0.5$ (solid line), $w_0 = -0.965$, $w_a = 0.665$ (dashed line), $w_0 = -0.8$, $w_a = 0.24$ (dotted line). Figure from [9].

Hence, in order to explain the CC as a vacuum energy, we need to balance the term $8\pi G\rho_{vac}$ tuning Λ_0 in order to obtain a small, but non vanishing, value of Λ today.

There is no specific reason why the two terms in Eq. 2.16 should sum up to the observed value; moreover, to this day we are unable to calculate the vacuum energy density in QFTs like the Standard Model (SM) of particle physics. There are no theoretical convincing arguments for expecting a particular value of ρ_{vac}. On the other hand, if the association between the CC and the energy ground state of vacumm occurs at the Planck scale, the latter would be of the order of magnitude of the Planck energy density $\rho_{Planck} \approx \sqrt{\frac{1}{G^2}}$, which is about 123 orders of magnitude larger than the present critical density in 2.17. This is one of the most problematic aspects of the interpretation of DE as vacuum energy at a quantum level, and yet among the most fascinating ones, as it is shedding light on our inaccurate knowledge of both cosmology and QFT.

2.1.3 CMB lensing constraints on Dark Energy

The cross-correlation of the lensing potential with the lensed CMB can help constraining curvature and the DE model through the ISW effect. These probes are however not very precise as they are plagued by cosmic variance uncertainties, which is high at low ℓ multipoles. A more direct imprint of DE can be inferred

from the lensing potential itself since it is affected by the growth function of the LSS [9].

In particular, CMB lensing is capable of picking up the DE abundance at the onset of acceleration, as the cross section is zero if the lens is coincident with the observer or the source, becoming instead maximum in intermediate regions [25]; in particular, if the source can be considered at infinity the lensing cross section is non-zero at redshifts in the range $0.1 \lesssim z \lesssim 10$, peaking at $z \approx 1$, rather independently of the particular cosmological model considered, and thus most relevant to study the Universe at the corresponding epoch. The sensitivity to a broad range of redshifts also implies that CMB lensing is a unique probe of DE (or, more generally, of clustering) at $z \gtrsim 2$. In Chapter 3 it will be shown how different evolving DE models influence not only the expansion history, but also the clustering of structures and therefore affect the lensing signal, modifying its amplitude in the $B-$modes of CMB (see Fig. 2.4); for this reason, this measurement is able to break the projection degeneracy, since it alters the position of the acoustic peaks, together with modifying the amplitude of the B polarisation.

Using CMB and lensing potential can help constraining time dependent DE EoS, and/or the presence of early DE [69]. These early DE models follow from physics where DE traces the energy density of the dominant component of the Universe, as for example in high energy physics and string theory models (see, e.g., [70] and references therein). The presence of a non-negligible component of DE at early times has important impacts on the sound horizon scale, structure formation, and secondary anisotropies and a joint CMB plus lensing analysis can become a good probe for this kind of models as this combination is sensitive to all the effects. The constraints can also be improved using additional external data from weak lensing and DE optical surveys ([71], and references therein) or, in the future, from 21 cm emission lines observations [72, 73].

2.2 Neutrino cosmology and the Standard Model

The historic discovery of neutrino flavor oscillations provided one of the most important signatures for new physics beyond the SM. Namely, it implied that neutrinos exhibit distinct, non-zero masses and that the propagating mass eigenstates in general are different from the flavor eigenstates produced and detected in experiments. While by now solar and atmospheric oscillation experiments have provided us with a fairly good knowledge of both neutrino mass squared differences and mixing angles (for a recent review see [74] and references therein), they are insensitive to one crucial, still outstanding input - the absolute neutrino mass scale. So far, only upper limits exist which are derived from the experiments aiming to measure of neutrinoless β decay $0\nu\beta\beta$ and endpoint spectrum studies of β decay as well as from cosmological measurements sensitive to neutrino masses.

In this section, the main aspects of the SM in relation to neutrinos will be reviewed, along with the physical effects arising from the presence of neutrinos in the cosmological framework.

	Name	l	Q	L_e	L_μ	L_τ
First	electron	e	-1	1	0	0
generation	e neutrino	ν_e	0	1	0	0
Second	muon	μ	-1	0	1	0
generation	μ neutrino	ν_μ	0	0	1	0
Third	tauon	τ	-1	0	0	1
generation	τ neutrino	ν_τ	0	0	0	1

Table 2.1: The three generations of leptons.

2.2.1 The Standard Model

All the phenomena observed up to now in fundamental physics are described with high accuracy by the SM of elementary particles and fundamental interactions. With the observation of the Higgs boson of mass ~ 125 GeV by the ATLAS[1] and CMS[2] collaborations at the Large Hadron Collider [75, 76], the whole set of particles foreseen in the framework of the SM has been detected, confirming its validity as one of the most predictive theories currently at our disposal.

From the theoretical point of view the SM is a QFT based on gauge symmetry $SU(3)_C \times SU(2)_L \times U(1)_Y$. This gauge group includes the symmetry groups of strong interaction $SU(3)_C$, and of electroweak interaction $SU(2)_L \times U(1)_Y$. The symmetry group of electromagnetic interaction $U(1)_{em}$, appears in the SM as a subgroup of $SU(2)_L \times U(1)_Y$, since electromagnetic and weak interactions are unified.

In this context all matter is made out of three kinds of elementary particles: leptons, quarks and gauge bosons. There are six leptons with half-integer spin, obeying then to Fermi-Dirac statistics, classified according to their charge expressed in unities of electron charge (Q) and lepton number (L). They are divided into three *families*, or *generations*, each of them having its own lepton number (see Tab. 2.1). Every lepton has its antilepton, with same characteristics but opposite sign of charge. Similarly, there are six flavours of quarks, which are fermions too, classified according to charge, isospin (I), strangeness (S), charm (C), beauty (B), and truth (T). The quarks belong as well to three generations (see Tab. 2.2) and like leptons the charges of antiquarks are reversed. Quarks are described by a further quantum number, the *colour* C: every quark and antiquark can come in three different colours and anticolours (red, green, blue, and their corresponding anticolours), for a total of 36 quarks and antiquarks and 12 leptons. Since all particles observed come with no colour, the quarks must be confined into matter particles in a singlet state of colour. Baryons are composed by three quarks qqq or three antiquarks $\bar{q}\bar{q}\bar{q}$, e.g. the proton $p = uud$, while the mesons are bound states of a quark and an antiquark $q\bar{q}$, e.g. the pions $\pi^+ = u\bar{d}$ and $\pi^- = d\bar{u}$.

[1] A Toroidal Lhc ApparatuS
[2] Compact Muon Solenoid

	Name	q	Q	I	S	C	B	T
First	down	d	-1/3	-1/2	0	0	0	0
generation	up	u	2/3	1/2	0	0	0	0
Second	strange	s	-1/3	0	-1	0	0	0
generation	charm	c	2/3	0	0	-1	0	0
Third	bottom	b	-1/3	0	0	0	-1	0
generation	top	t	2/3	0	0	0	0	-1

Table 2.2: The three generations of quarks.

The picture is still not complete, since the mediators for the fundamental interactions (excluding gravity, which is not described by the SM), bosons with spin $s = 1$, are still to be introduced. All interactions, electromagnetic, weak and strong, happen with the exchange of an elementary particle (the photon γ for e.m. force, the 8 gluons g_α for the strong force between quarks and the three bosons $W^\pm$ and Z_0 for the weak force). A synthetic table can be seen in Fig. 2.5.

The *gauge sector* of the SM is composed by the 8 gluons, and the particles γ, $W^\pm$ and Z_0. The main characteristics of gluons are that they are massless, neutrally charged and carry colour charge. Gluons can be found in 8 different colour charge states:

$$r\bar{b},\ r\bar{g},\ b\bar{r},\ b\bar{g},\ g\bar{r},\ g\bar{b},\ \frac{r\bar{r}-b\bar{b}}{\sqrt{2}},\ \frac{r\bar{r}+b\bar{b}-2g\bar{g}}{\sqrt{6}}$$

As a consequence of having a colour charge, gluons can either interact with quarks or self-interact; $W^\pm$ and Z_0 are massive and self-interacting, with $Q(W^\pm) = \pm 1$ and $Q(Z_0) = 0$, while γ is massless, neutrally charged and not self-interacting.

In the standard model, the Higgs field is an $SU(2)$ doublet, a complex scalar. The Higgs field, through the interactions specified by its potential, induces spontaneous breaking of three out of the four generators of the gauge group $SU(2)\times U(1)$ mixing with the three $W^\pm$ and Z bosons which now become massive. The one remaining degree of freedom becomes the Higgs boson - a new scalar particle.

The *fermionic sector* of quarks and leptons is organised in three generations that have identical properties, differing from each other only in mass. The particles in every generation are respectively

$$\begin{pmatrix}\nu_e\\ e\end{pmatrix}_L, e_R; \qquad \begin{pmatrix}u\\ d\end{pmatrix}_L, u_R, d_R$$
$$\begin{pmatrix}\nu_\mu\\ \mu\end{pmatrix}_L, \mu_R; \qquad \begin{pmatrix}c\\ s\end{pmatrix}_L, c_R, s_R$$
$$\begin{pmatrix}\nu_\tau\\ \tau\end{pmatrix}_L, \tau_R; \qquad \begin{pmatrix}b\\ t\end{pmatrix}_L, b_R, t_R$$

and their corresponding antiparticles. The chiral operator γ_5 is introduced [78]

$$\gamma_5 = i\gamma_0\gamma_1\gamma_2\gamma_3$$

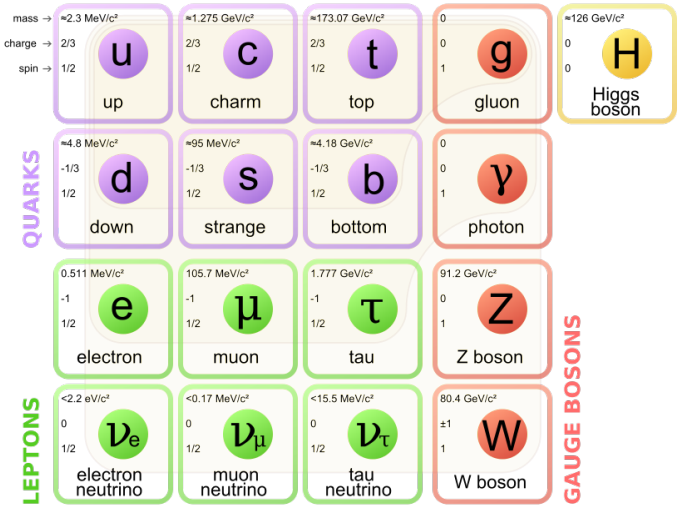

Figure 2.5: Particle content of the Standard Model of particle physics. Figure from [77].

because weak interaction only couples to the left-handed component of particles. The *chirality*, denoted by the subscripts L and R, is defined by the chiral operator γ_5 in the following way:

$$e_L = \frac{1}{2}(1-\gamma_5)e$$

$$e_R = \frac{1}{2}(1+\gamma_5)e$$

The chiral operator is introduced because weak interaction couples only to the left-handed component of particles.

There is no experimental reason of introducing a right-handed neutrino; there have been experiments aimed to measure neutrino helicity from Goldhaber et al. proving that neutrinos can only have left-handed helicity, and subsequently antineutrinos can only have right-handed helicity [79].

2.2.2 Massive neutrinos and flavor oscillation

In the framework of the SM of particle physics, right-handed neutrinos are not required by electroweak theory and thus the left-handed chiral neutrinos are the only fermions without right-handed partners in the theory. Accordingly, since Dirac mass terms necessitate fields of opposite chirality, neutrinos are massless in the SM as opposed to quarks and charged leptons.

However, experiments not only suggest that neutrinos are massive, but also that their masses are in the (sub-) eV range and thus orders of magnitude smaller than any other SM masses. Probably the most elegant and natural explanation beyond the SM description is provided by the so-called *see-saw mechanism* [80, 81, 82, 83]. In the framework of the see-saw mechanism, the SM Lagrangian is

augmented to include three fermions which play the role of "right-handed neutrinos" N (with $\nu^T = (\nu_{eL}^T, \nu_{\mu L}^T, \nu_{\tau L}^T)$), and are singlets under the SM gauge group. Consequently, for them, unlike for their left-handed partners, a lepton-number violating Majorana mass term is not protected by symmetries and is thus permitted. In addition, they can have a Yukawa interaction λ allowing for a Dirac mass term, possibly generated by the standard Higgs-mechanism [84]

$$\mathscr{L} = \mathscr{L}_{SM} + \bar{N}_i i\partial\!\!\!/ N_i + (\lambda_{ij} N_i L_j H - \frac{1}{2} M_{ij} N_i N_j + h.c.) \tag{2.18}$$

where $\mathscr{L}_{SM}$ $i, j = (1-3)$ denote the family-number indices, L_i are the $SU(2)$ lepton doublets, H is the ordinary Higgs doublet, the Majorana mass matrix M and the Yukawa matrix λ are 3×3 flavor matrices. The new scale introduced by the elements of M in Eq. 2.18 is assumed to be related to some "fundamental" physics at ultra-high energies beyond the low-energy description of the SM, e.g. to some symmetry breaking in the framework of grand unified theories. It thus seems natural to expect the eigenvalues of M to be much larger than those of the Dirac mass matrix M_D, since it is not protected by the SM gauge symmetries. Under this assumption, after integrating out the heavy right-handed neutrinos, one obtains the effective Lagrangian [85]

$$\mathscr{L} = \mathscr{L}_{SM} + \frac{1}{2} \sum_k (\lambda_{ik}^T M_k^{-1} \lambda_{kj})(L_i H)(L_j H) + h.c. \tag{2.19}$$

which only contains observable low-energy fields. After spontaneous electroweak symmetry breaking [84], the Higgs field acquires a vacuum expectation value, $\langle H \rangle \simeq 246$ GeV, which generates the following 3×3 Majorana mass matrix for light neutrinos,

$$(m_\nu)_{ij} \simeq -(M_D^T M^{-1} M_D)_{ij} \text{ with } M_{D_{ij}} = v\lambda_{ij} \tag{2.20}$$

From naturalness arguments it should be expected that the Dirac mass for each generation of neutrinos is of the same order of magnitude as the mass of the corresponding quark or charged fermion. Accordingly, the see-saw mechanism naturally ascribes the relative smallness of neutrino masses to the suppression of the Dirac mass matrix M_D by the small matrix factor $M_D^T (M)^{-1}$; in addition, the neutrinos ν_i with definite masses m_{ν_i} are predicted to be Majorana particles. This implies that they possess only half of the four independent components of Dirac particles and are their own charge conjugates

$$\nu_i = \mathscr{C} \bar{\nu}_i^T \equiv \nu_i^c \tag{2.21}$$

with $\mathscr{C}$ denoting the charge conjugation matrix. Importantly, the predicted Majorana nature of neutrino masses is a clear signature for the see-saw mechanism and implies the existence of a new fundamental scale in nature $\Lambda \simeq v^2/m_\nu \simeq 10^{14} - 10^{15}$ GeV for $m_\nu \sim 10^{-2} - 10^{-1}$ eV.

Since the neutrino mass matrix is not diagonal when expressed in terms of the flavor eigenstates, one is led to the concept of neutrino flavor oscillations.

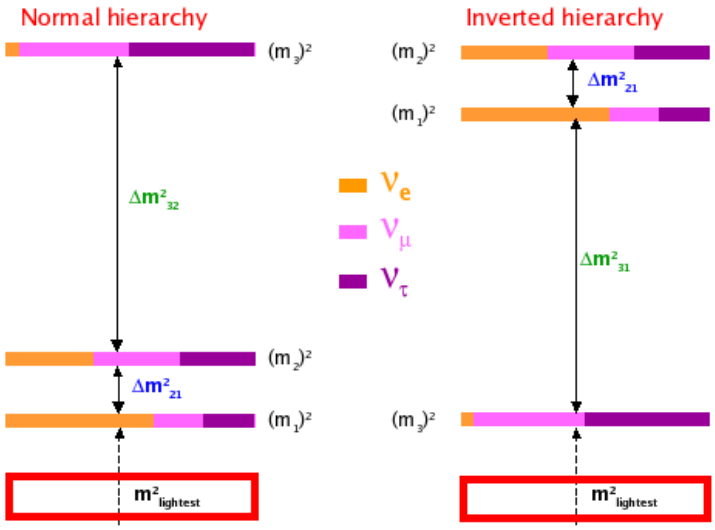

Figure 2.6: The different possible neutrino mass hierarchies. Figure from [87].

In other words, the flavor eigenstates ν_α participating in weak interactions are superpositions of the propagating neutrino states ν_i of definite mass m_i

$$|\nu_\alpha\rangle = \sum_{i=1}^{3} U^*_{\alpha_i} |\nu_i\rangle \tag{2.22}$$

where $\alpha = e, \mu, \tau$ and the 3×3 neutrino mixing matrix U is determined by the condition

$$U^T m_\nu U = \text{ diag } (m_1, m_2, m_3) \tag{2.23}$$

The most common parameterisation of the mixing matrix in components, U_{α_i} is the so called standard parametrisation [86]

$$\begin{array}{c} \\ \nu_e \\ \nu_\mu \\ \nu_\tau \end{array} \begin{array}{c} \begin{array}{ccc} \nu_1 & \nu_2 & \nu_3 \end{array} \\ \begin{pmatrix} c_{12}c_{13} & c_{13}s_{12} & s_{13}e^{-i\delta} \\ -c_{23}s_{12} - c_{12}s_{13}s_{23}e^{i\delta} & c_{23}c_{12} - s_{12}s_{13}s_{23}e^{i\delta} & c_{13}s_{23} \\ s_{23}s_{12} - c_{12}s_{13}c_{23} & -c_{12}s_{23}e^{i\delta} - s_{12}s_{13}c_{23}e^{i\delta} & c_{13}c_{23} \end{pmatrix} \end{array}$$
$$\times \text{ diag } (1, e^{i\alpha_{21}/2}, e^{i\alpha_{13}/2}) \tag{2.24}$$

with $c_{ij} \equiv \cos\theta_{ij}$, $s_{ij} \equiv \sin\theta_{ij}$, where $\theta_{12}, \theta_{23}, \theta_{13}$ are the three mixing angles, δ is the Dirac phase and α_{21} and α_{13} are the Majorana phases.

In case neutrinos are Dirac particles, the Majorana phases can be eliminated by a rephrasing of the massive neutrino fields. All of the three complex phases in the mixing matrix generate violations of the CP symmetry.

Let us consider in the following a neutrino produced and detected with definite flavor in weak charged-current interactions after propagating a time T and a

distance L in vacuum. The normalised neutrino state at the production point is related to the state $|\nu_\alpha(L,T)\rangle$ at the detection point by the Schrödinger equation as follows:

$$|\nu_\alpha(L,T)\rangle = \sum_{\beta=e,\mu,\tau} \left[\sum_{i=1}^{3} U^*_{\alpha_i} e^{-iE_iT+ip_iL} U_{\beta_i} \right] |\nu_\beta\rangle, \tag{2.25}$$

where E_i and p_i, respectively, are the energy and momentum of the massive neutrino ν_i. Consequently, at detection the state describes a superposition of different neutrino flavors giving rise to the possibility of flavor change in vacuum with associated probability $P_{\nu_\alpha\to\nu_\beta}$ [74]

$$\begin{aligned} P_{\nu_\alpha\to\nu_\beta} &= |\langle\nu_\beta|\nu_\alpha(L)\rangle|^2 = \left| \sum_{i=1}^{3} U^*_{\alpha_i} e^{-i\frac{\Delta m^2_{ij}L}{2E}} U_{\beta_i} \right| \\ &= \sum_{i=1}^{3} |U_{\alpha_i}|^2 |U_{\beta_i}|^2 + 2\,\mathrm{Re} \sum_{i>j} U^*_{\alpha_i} U_{\beta_i} U_{\alpha_j} U^*_{\beta_j} e^{-i\frac{\Delta m^2_{ij}L}{2E}}, \end{aligned} \tag{2.26}$$

where $\Delta m^2_{ij} = m^2_i - m^2_j$ and the dependence on T has been expressed in terms of the neutrino masses and energy. Accordingly, the neutrino mass squared differences as well as the mixing matrix are the fundamental inputs which determine neutrino oscillations. Neutrino oscillation experiments are characterised by a different neutrino energy E and propagation distance L.

It should be noted that the vacuum transition probability $P_{\nu_\alpha\to\nu_\beta}$ in Eq. 2.26 gets modified by neutrino interactions resulting from the propagation through matter. While neutral current interactions are common to all neutrino flavors, only electron neutrinos can additionally have charged current interactions with electrons composing the matter besides nucleons (or quarks). As a result, with respect to the other flavors, the time development of electron neutrinos is altered by a phase which is determined by the electron density of the medium of propagation.

It is to be noted that since the neutrino oscillations have been observed and measured, this implies that neutrinos should have a mass, albeit very small. A huge effort is being devoted in the particle physics community to unveil the neutrino properties.

Let us now briefly review the results of a global analysis of recent experimental data on the neutrino mixing parameters and the mass differences gained from neutrino oscillation experiments. The current values obtained from the global fit analysis of neutrino oscillations data are presented in Table 2.3.

One of the key achievements of neutrino oscillation experiments is the provided knowledge on the neutrino mass squared differences $\Delta m^2_{ij} = m^2_i - m^2_j$. Solar neutrino and reactor antineutrino experiments as well as atmospheric and long-baseline accelerator neutrino experiments allow to interpret the oscillation data in terms of three-neutrino mixing (see again 2.3) So far, both the sign of Δm^2_{31}, and the absolute neutrino mass scale are not known, thus leaving undetermined which of the following three possible neutrino mass schemes are realised in nature, see also Fig. 2.6:

Parameter	Best fit	1σ range
Mass splittings		
$\delta m^2/10^{-5}$ eV^2 (Normal or inverted hierarchy)	7.54	7.32 – 7.80
$\Delta m^2/10^{-3}$ eV^2 (Normal hierarchy)	2.43	2.37 – 2.49
$\Delta m^2/10^{-3}$ eV^2 (Inverted hierarchy)	2.38	2.32 – 2.44
Mixing angles		
$\sin^2\theta_{12}/10^{-1}$ (Normal or inverted hierarchy)	3.08	2.91 – 3.25
$\sin^2\theta_{13}/10^{-2}$ (Normal hierarchy)	2.34	2.15 – 2.54
$\sin^2\theta_{13}/10^{-2}$ (Inverted hierarchy)	2.40	2.18 – 2.59
$\sin^2\theta_{23}/10^{-1}$ (Normal hierarchy)	4.37	4.14 – 4.70
$\sin^2\theta_{23}/10^{-1}$ (Inverted hierarchy)	4.55	4.24 – 5.94

Table 2.3: Summary of present information on neutrino masses and mixing from oscillation data from [88]. Here $\delta m^2 \equiv \Delta m^2_{21}$, $\Delta m^2 \equiv \Delta m^2_{31} - \Delta m^2_{21}/2$.

- Degenerate spectrum: $m_1 \sim m_2 \sim m_3 >> |m_i - m_j|$.
- Normal hierarchy: $m_3 >> m_{2,1}$ ($\Delta m_{31} > 0$) in analogy to quarks and charged leptons.
- Inverted hierarchy: $m_1 \sim m_2 >> m_3$ ($\Delta m_{13} < 0$).

Since neutrino oscillation experiments are only sensitive to neutrino mass squared differences but not to the absolute neutrino mass scale, they can only provide lower limits, $\sqrt{\Delta m^2_{ATM}} \simeq 0.05$ eV and $\sqrt{\Delta m^2_{SOL}} \simeq 0.01$ eV, where the pedices *ATM* and *SOL* stand for bounds from atmospheric and solar experiment respectively, for two of the neutrino masses.

Bounds on the absolute neutrino mass scale can be obtained from β decay and neutrinoless double β decay experiments (if neutrinos are Majorana particles) as well as from cosmological measurements, which will be reviewed in subsec. 2.2.3.

- β decay: The neutrino mass m_{ν_e} distorts the energy spectrum of electrons emitted in the β decay of a nucleus (the most sensitive choice being tritium). The analysis of the electron spectrum near the end-point allows for a robust kinematical measurement of $m^2_{\nu_e} = \sum_i |U_{ei}|^2 m_i^2$. The most stringent upper bound on the electron neutrino mass derived from tritium beta decay is m_{ν_e} <2.0 eV [89, 90] at 95% confidence level. Assuming CPT-invariance, combined with the observed oscillation frequencies, this mass bound applies to all active neutrinos. The future experiment KATRIN [15] is expected improve the sensitivity to by one order of magnitude down to about 0.2 eV.
- Neutrinoless double β decay: Less direct information on the absolute neutrino mass scale can be inferred from neutrinoless double β decay which is, however, only allowed if neutrinos are Majorana particles. Thus, the

importance of its discovery would mainly lie in the establishment of lepton number violation of 2 units as well as the Majorana nature of neutrino masses [86]. The measured decay amplitude not only depends on the Majorana effective mass $m_{ee} = \sum_i |U_{ei}|^2 m_i$, but also on the $0\nu2\beta$ nuclear matrix elements, which are affected by sizeable theoretical uncertainties. Present limits on the effective electron neutrino mass are $|m_{ee}| <$ (0.105 - 0.840) eV [91, 92, 93], $|m_{ee}| <$ (0.114 - 0.912) eV [91, 92, 94], $|m_{ee}| <$ (0.168 - 1.134) eV [91, 95, 96]. The controversial claim in [91] of a 4.2σ evidence for $0\nu2\beta$ (see [97] and references therein) has been disfavoured by the GERDA experiment after Phase I of data collection, setting an upper bound of $|m_{ee}| < 0.2 - 0.4$ eV [98]. If confirmed, the signal would be interpreted in terms of quasi-degenerate neutrino masses of 0.1 - 0.9 eV $\left(\sum m_{nu} > 1.2 \text{ eV at } 2\sigma\right)$.

2.2.3 Effects of neutrinos in cosmology

Assuming that the thermal history of the Universe proceeds according to the Big Bang theory predictions, it is possible to derive the contribution given by the presence of massive neutrinos to the overall budget of the Universe defining a density parameter Ω_ν [21]

$$\Omega_\nu = \frac{\sum m_\nu}{94 h^2 \text{eV}} \qquad m_\nu \neq 0, \tag{2.27}$$

The fractional contribution to the mass contribution f_ν is then

$$f_\nu = \frac{\Omega_\nu}{\Omega_m} \approx 0.08 \frac{\sum m_\nu}{\text{eV}}. \tag{2.28}$$

The bounds reviewed in subsec. 2.2.2 suggest that the neutrino mass is small enough to be relativistic at the time of recombination; subsequently, the evolution of the neutrino component will be substantially different from the baryonic and Dark Matter components, see Fig. 2.7. Neutrinos can thus contribute to the overall pressure and lead to a smearing out of over-dense regions. At a given epoch the neutrinos can stream freely for a comoving distance set by [12]

$$\lambda_\nu^{FS}(z) \approx 7.7 \frac{1+z}{\Omega_\Lambda + \Omega_m (1+z^3)} \left(\frac{1 \text{ eV}}{m_\nu}\right) \frac{1}{h} \text{ Mpc} \approx \frac{0.04}{f_\nu h \sqrt{a}} \text{ Mpc}, \tag{2.29}$$

below which neutrinos will not clump significantly. On these scales, the density dilution of neutrinos due to the expansion of the Universe prevents the accretion due to gravitational instability, and gravitational potential wells decay leading to a slower structure formation rate in the intervening time scales. Structures on scales smaller than ≈ 0.1 Mpc$/f_\nu$ are suppressed for every epoch, while scales larger than 100 Mpc are never affected, leading to a decrease in the power spectrum of the matter distribution for small scales, while the structure on large scales is essentially unmodified. It has been shown [100] that the fractional suppression of

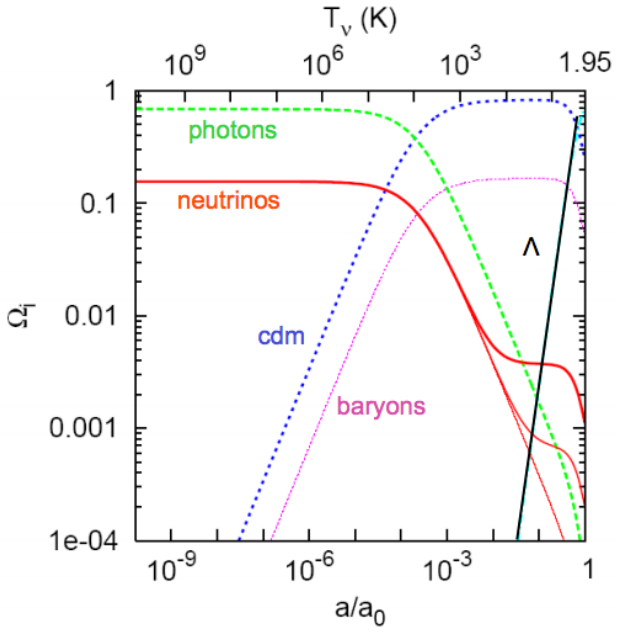

Figure 2.7: Evolution of the background energy densities in terms of the fractions Ω_i from $T = 1$ MeV until now, for each component of a flat Universe with $h = 0.7$ and current density fractions $\Omega_\Lambda = 0.70$, $\Omega_b = 0.05$ and $\Omega_{CDM} = 1 - \Omega_\Lambda - \Omega_b - \Omega_\nu$. The three neutrino masses are $m_1 = 0, m_2 = 0.009$ eV and $m_3 = 0.05$ eV. Figure from [99].

the matter power spectrum $P(k)$, with k the spatial wavenumber, is of the order of $\Delta P(k)/P(k) \sim -10 f_\nu$ for scales $k \sim 0.5 - 1h$ Mpc^{-1}, see also Fig. 2.8.

There is a number of ways to probe the role of the neutrino mass on cosmological scales which resort to a mapping of matter distribution. The most widely used tracers are the galaxies and galaxy clusters distribution, the neutral hydrogen mapping through Lyman$-\alpha$ 21 cm line absorption or emission processes and weak gravitational lensing in the optical wavelength range. Each one of these probes is subject to different systematics related, e.g., to the lack of knowledge about the bias of galaxy distribution, effects of non-linear evolution, foreground modelling, and many other possible contaminants of astrophysical origin.

The CMB is also sensitive to the massive neutrinos as they increase the anisotropy on small scales because the decaying gravitational potentials enhance the photon energy density fluctuation through an early ISW effect [102]. Furthermore, neutrinos modify the sound horizon at recombination θ_* and thus the position of the acoustic peaks shifts. For light masses, the change in the sound horizon is small; on the other hand, keeping all the other parameters fixed, defining our cosmological model (as the sound horizon is degenerate with Ω_Λ, H_0 and w), the value of θ_* drops significantly with increasing mass due to the increased expansion rate at late times, which in turn makes the last scattering surface look closer and anisotropies shifted to larger angular scales. In Fig. 2.7 the effect on the CMB temperature spectrum of increasing the neutrino mass while keeping the redshift at equivalence and

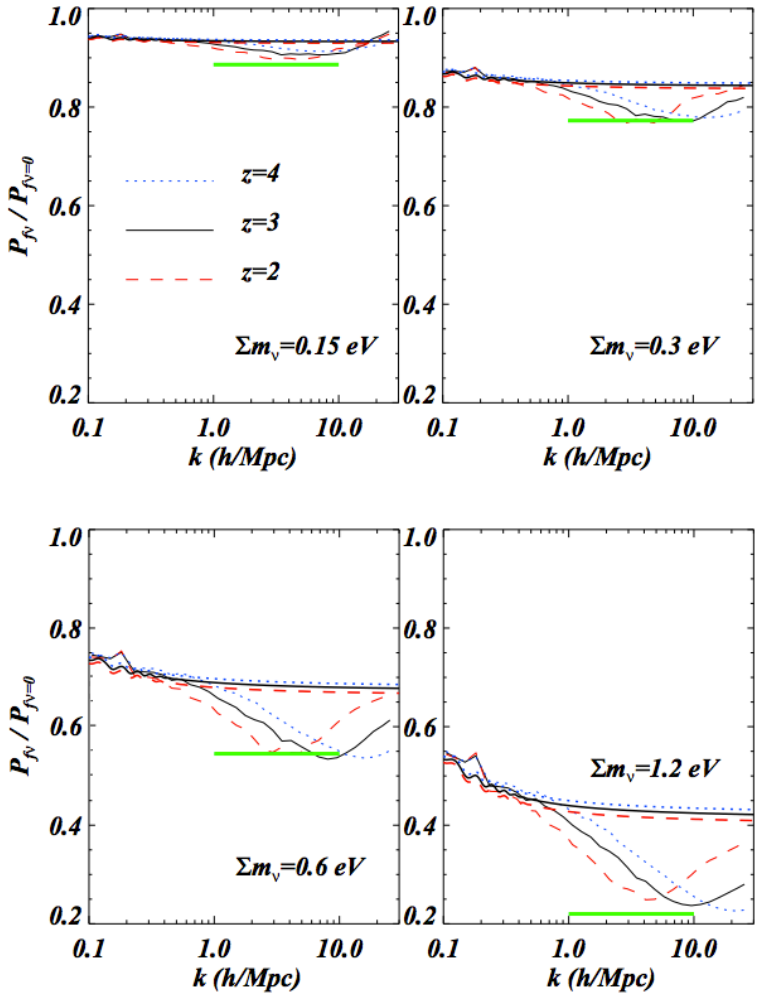

Figure 2.8: Effect of different values of f_ν on the matter power and comparison with linear prediction. The ratio between matter power spectra for simulations with and without neutrinos for four different values of the neutrino mass is shown $\sum m_\nu = 0.15$, 0.3, 0.6, 1.2 eV (from left to right, top to bottom). Different line-styles refer to different values of the redshift: $z = 2$ (red dashed), z =3 (black continuous) and $z = 4$ (blue dotted). The predictions of linear theory are shown as the thick curves. An estimate of the overall suppression based on the hydrodynamical simulations is shown as a thick short green line, $\Delta P/P \sim 10.5 f_\nu$. Figure from [101].

the angular distance to the last scattering surface fixed is shown: the only observed differences are then for $2 < \ell < 50$ (late ISW effect due to neutrino background evolution) and for $50 < \ell < 200$ (early ISW effect due to neutrino perturbations). By looking at the modifications induced on the spectra, and considering that the signal at low ℓ is heavily affected by cosmic variance, one can argue that the CMB alone is not a very powerful tool for constraining sub-eV neutrino masses, and should be used in combination with other datasets, e.g. measurements of the LSS power spectrum, for instance from galaxy clustering, galaxy lensing or CMB lens-

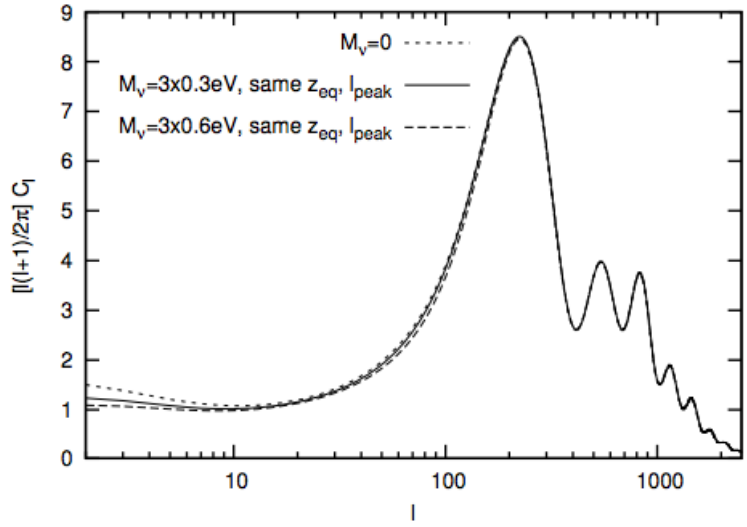

Figure 2.9: CMB temperature spectrum with different neutrino masses. Some of the parameters of the ΛMDM model (Mixed Dark Matter, where Mixed refers to the inclusion of some hot Dark Matter component) have been varied together with M_ν in order to keep fixed the redshift of equality and the angular diameter distance to last scattering. Figure from [99].

ing [102].

The effects induced by having massive rather than massless neutrinos are degenerate with the effective number of relativistic species N_{eff}, which can be considered a contribution to the radiation density, as the effect would mimic the presence of a relativistic neutrino. The standard model predicts $N_{eff} = 3.046$ but recent data from SPT [103] lead to an evidence of an extra dark radiation component $N_{eff} = 3.93 \pm 0.68$, which is in tension with the result coming from ACT data, $N_{eff} = 2.74 \pm 0.47$ [104] and the standard model value, but in agreement with the existence of a hypothetical sterile neutrino. The effect of an extra radiation component on the CMB is a shift in the acoustic peaks due to a delayed matter-radiation equality which modifies the sound horizon and the height of acoustic peaks and a modified early ISW contribution. As a result, the position of the matter power spectrum shifts at smaller scales because matter radiation-equality is shifted to later times and modifies thus the lensing potential.

On the polarisation level, however, the difference is more important, especially in the $B-$modes spectrum, as the lensing potential is sensitive to the neutrino mass since it consists of an integral of the matter perturbation along the line of sight and is affected by the damping in the matter power spectra. As previously argued, increasing neutrino mass has the effect to increase the expansion rate at $\gtrsim 1$ and so suppresses clustering on scales smaller than the horizon size at the non-relativistic transition [14, 105]. The net effect for lensing is a suppression of the CMB lensing potential and, as an estimate, by $\ell \approx 1000$ the suppression is around 10% in power for $\sum m_\nu \approx 0.66$ eV [13]. Bounds on neutrino mass can therefore be derived using

the lensing potential reconstructed from CMB and lensed $B-$modes power spectra up to an ultimate limit of 35 meV which can be reached in the case of a cosmic variance limited full-sky CMB polarisation survey, always keeping in mind that this quantity is degenerate with other parameters which enter the structure formation, and that cross-correlation of different datasets are able to lift these degeneracies [14].

Current limits on the total neutrino mass $\sum m_\nu$ from cosmology are rather model dependent and vary strongly with the data combination adopted. The tightest constraints for flat models with three families of neutrinos are of the order of 0.3 eV (95% CL; e.g., [106]). Since $\sum m_\nu$ must be greater than approximately 0.06 eV in the normal hierarchy scenario and 0.1 eV in the degenerate hierarchy scenario [107], the allowed neutrino mass window is already quite tight and could be closed further by current or forthcoming observations [108, 109]. The PLANCK collaboration reported an upper limit on the sum of neutrino masses $\sum m_\nu < 0.23$ eV, and for the effective number of species the result is well consistent with what predicted by Big Bang nucleosynthesis $N_{eff} = 3.30 \pm 0.27$ [13].

3

Prospects for B-mode power spectra measurements

After 50 years from the first detection of the CMB radiation, and subsequently the turning of cosmology from a speculative to a quantitative and predictive discipline, the last stand for this branch of astrophysics still lies in the relic radiation from the Big Bang, which has been characterised from the very large superhorizon scales down to $\ell \sim 4000$ in total intensity, but despite the fact that a lot of efforts have been made in the recent years, a full observation of the polarised emission from the last scattering surface is still not available.

In the signal coming from the polarised $B-$modes the signature of inflation is encoded, the highly accelerated expansion phase taking place in the first infinitesimal fraction of the life of the Universe. This theory, first proposed around thirty years ago in [110], would provide, together with the description of the initial evolutionary phase of the Universe, also the spectrum of primordial perturbation which, following the gravitational attraction, grow into the structures we observe today.

In Sec. 1.1 the presence of both the tensor signal coming from inflation, and the weak lensing of CMB in the $B-$modes was discussed. The coexistence of both components in the same ℓ range, a primordial and a late-time one, might induce an additional noise source when trying to estimate the amplitude of the inflationary perturbations. This issue might become even more important when considering non-standard histories of evolving DE; the case for a possible deviation from the standard ΛCDM model has been made in Sec. 2.1.

A number of sub-orbital experiments are planned and have been observing selected regions of the sky and frequency spectrum, looking for arcminute and sub-arcminute scale anisotropies in total intensity, as well as polarisation[1]. These observations will target most important and yet still undetected effects, dominating the curl component ($B-$modes) of the linear polarisation pattern in CMB anisotropies [16, 17]. On arcminute angular scales, the latter are dominated by the gravitational lensing of the anisotropies at last scattering by means of forming cosmological structures along the line of sight, as argued in Sec. 1.4. The lensing effect coming from the power spectrum of the underlying DM distribution, and the

[1] see `http://lambda.gsfc.nasa.gov/` for the list of operating or planned sub-orbital CMB experiments.

primordial $E-$modes, produce a characteristic and broad lensing peak located at $\ell \simeq 100$ in the $B-$modes power spectrum.

Gravitational lensing has been recently detected in the damping tail of the temperature power spectrum by several groups, also cross-correlating the lensing with observed structures, while for the $B-$modes some first measurements have been presented by the SPT and POLARBEAR collaborations. The latest observational results have been presented in Sec. 1.5, and will not be recalled here. On the degree angular scales on the other hand, a primordial spectrum of tensor anisotropies or Primordial Gravitational Waves (PGWs) would produce a narrow peak, rapidly vanishing on sub-degree angular scales, not supported by radiation pressure from massive particles, as is instead the case for T and $E-$modes. On large angular scales, corresponding to several degrees in the sky, the decay of the PGWs tail in the $B-$modes can be re-amplified though re-scattering onto electrons in the epoch of cosmic reionisation.

The two effects compete for detection, and their different origin, primordial and linear for PGWs, late and second order for lensing, has been exploited for designing separation techniques [34]. Furthermore, it has been analysed in the past how an accelerated expansion modifies the shape of the spectrum of PGWs as a result of propagation in a different space-time [111].

The lensing peak of $B-$mode anisotropies strongly depends on the history of cosmic expansion. It has been shown [9] that its amplitude may undergo variations of order 10% if the DE is dynamical at the epoch corresponding to the onset of acceleration, i.e. about $z \in [1-3]$, in which its actual amplitude is poorly constrained by existing measurements of the CMB or LSS. The $B-$mode lensing peak as a DE probe has been investigated by several authors [8, 9], who in particular have shown how the lensing is capable of breaking the projection degeneracy affecting CMB anisotropies at the linear level, as it was recently confirmed in the context of lensing detection for sub-orbital $T-$mode experiments [5, 10].

On the other hand, the detection thresholds for PGWs as well as the accuracy on DE constraints from CMB observations have never been given by taking into account the full set of degrees of freedom, represented not only by the amplitude of PGWs, but also by those related to the expansion history, parametrised through suitable DE models. The release of the latter degrees of freedom in the context of experiments aiming at the detection and characterisation of $B-$mode anisotropies is expected to have a direct impact in the quoted detection thresholds of PGWs.

Recently, the PLANCK Collaboration published an upper limit on $r < 0.11$ at 95% CL, obtained from the analysis of the spectrum of the temperature data [112]; this result shall be improved with the next data release containing also polarisation data. Moreover, the BICEP2[2] Collaboration claimed in [113] a first detection of the degree scale $B-$modes setting a tentative measurement of $r = 0.2^{+0.07}_{-0.05}$. This result is currently being reviewed by the astrophysical community, in particular concerning the residual foreground emission of polarised sources at high galactic latitudes [114].

[2]Background Imaging of Cosmic Extragalactic Polarisation

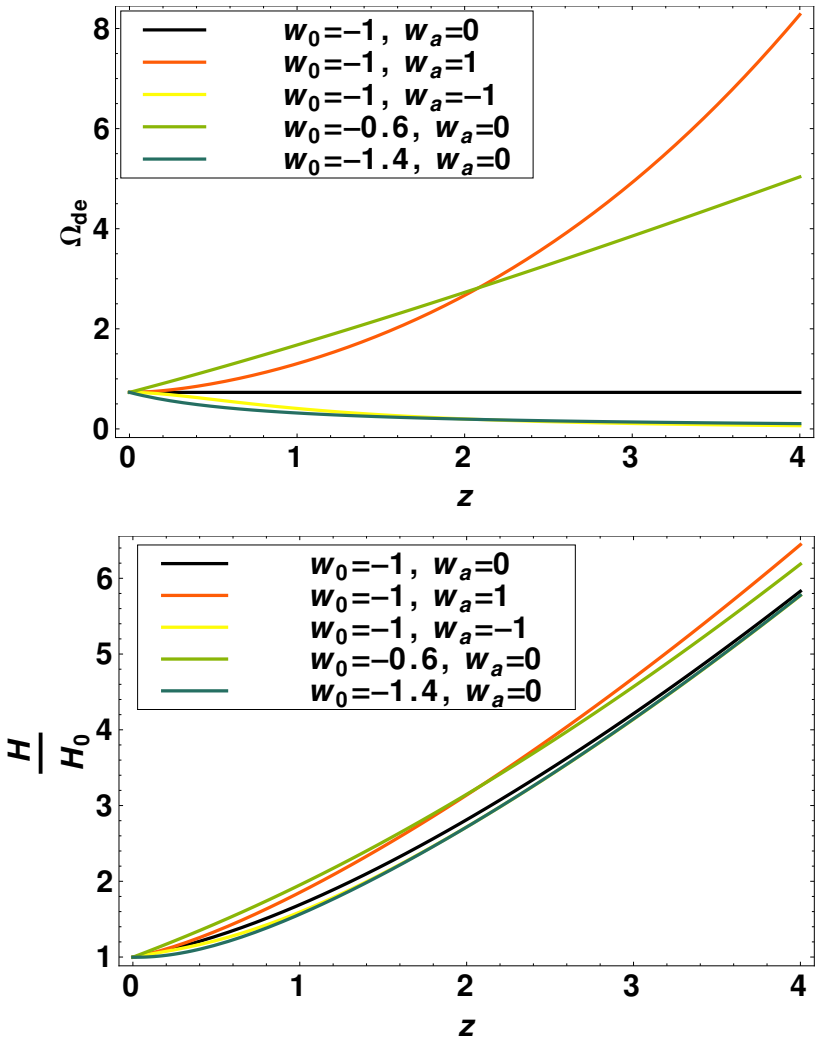

Figure 3.1: Top panel: redshift evolution of the DE component with different values of w_0, w_a. As the sum w_0, w_a get above -1, the DE term becomes increasingly important in the past. Bottom panel: corresponding evolution of the Hubble parameter with redshift with the same expansion histories considered in the left panel.

In this Chapter, following the work presented in [1], a procedure of simultaneous forecasting of both the tensor-to-scalar ratio r and evolving DE histories is illustrated. This will serve as a guidance for quantifying how the cosmological constraints on the very early Universe and on cosmic acceleration depend on each other. For simplicity, our lensing description here is based on the effects on the $B-$modes of the CMB, even if we also provide comparisons with the cases of forecasted direct lensing measurements, which will be the subjects of Chapter 4.

The sensitivity of forthcoming $B-$mode probes on PGWs abundance as well as DE dynamics is investigated, keeping in mind that all the physical degrees of freedom shaping the $B-$mode power spectrum should be considered and treated jointly. In this context in particular the interplay between satellite measurements,

accessing large scale polarisation and extracting lensing mainly from T and E measurements, and the case of sub-orbital ones, directly probing lensing $B-$modes, is considered. We will take as reference two among the most important operating $B-$mode probes, EBEX[3] [115] and POLARBEAR [116] as well as the all-sky measurements featuring the nominal capabilities from PLANCK[4] [117].

The work will be presented as follows: in Sec. 3.1 the impact of a modified expansion history on the CMB lensing power is illustrated, proceeding in Sec. 3.2 to the description of the simulated datasets as well as the considered reference experiments. In Sec. 3.3 the obtained results are shown and discussed, while in Sec. 3.4 the conclusions are presented.

3.1 Generalised expansion histories: how lensing affects the CMB spectra

In the context of this work, models of expansion history corresponding to a CC and its generalisation through the equation of state $w = p/\rho$ of the DE evaluated at present are considered, as well as its first derivative in the scale factor [60, 61], already presented in Sec. 2.1. In this modelisation, the DE equation of state and the ratio Ω_{DE} of its energy density with respect to the cosmological critical density are given by (recalling Eqns. 2.5, 2.6)

$$p = \left[w_0 + (1-a)w_a\right]\rho \quad , \quad \Omega_{DE}(z) = \Omega_{DE,0}\exp(3\int_0^z dz' \frac{1+w(z')}{1+z'}) \, . \tag{3.1}$$

Such a parametrisation allows for a large set of dynamics in the cosmic acceleration, and in particular an increased DE abundance at the equivalence with CDM and the onset of acceleration. In the following we will see how the evolution of DE with time affects the CMB lensing because of its influence on the structures generating the gravitational potential responsible for the deflection. In Fig. 3.1, top panel, one can see how the DE density evolves with time as the w_0, w_a parameters vary. In order to get a glimpse on how the lensing process is modified by different expansion histories, let us look again at Eq. 3.1 and consider how this influences the evolution with redshift of the Hubble parameter $H(z)$, which we can see in Fig. 3.1 (bottom panel).

Gravitational lensing deflection angle is related to the lensing projected potential ϕ (see e.g. [118, 119]) through the relation

$$\mathrm{d}_\ell^m = -i\sqrt{\ell(\ell+1)}\phi_\ell^m. \tag{3.2}$$

It is characterised by the lensing deflection power spectrum C_ℓ^{dd}, which is defined through the ensemble average

$$\langle \mathrm{d}(a,b)_L^{M*}\mathrm{d}(a',b')_{L'}^{M'}\rangle \equiv \delta_L^{L'}\delta_M^{M'}(C_L^{dd} + N_L^{aa'bb'}) \, , \tag{3.3}$$

[3] E and B EXperiment

[4] When this work was conceived and published, the 2013 PLANCK dataset had not yet been released; for this reason, the nominal capabilities from the Scientific Programme of PLANCK we used, rather than performing the analysis on the actual dataset.

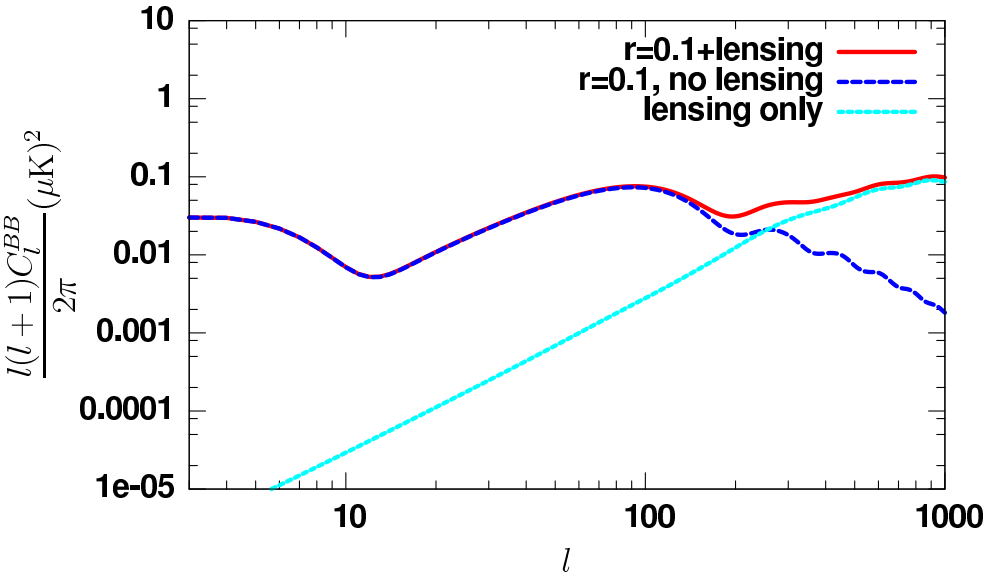

Figure 3.2: $B-$modes for CMB polarisation anisotropies with different contributions given by primordial tensor modes only with $r = 0.1$ (green), by lensing only (blue), and the total for both lensing and $r = 0.1$ tensor modes.

where $N_\ell^{aa'bb'}$ is the noise power spectrum, which reflects the errors in the deflection map reconstruction, and can be estimated for a given combination of lensing extraction technique and experiment.

Following [120], the lensing deflection angle can be inferred by the observed CMB anisotropies through

$$\mathrm{d}(a,b)_L^M = n_L^{ab} \sum_{\ell\ell' mm'} W(a,b)_{\ell\ \ell'\ L}^{mm'M} a_\ell^m b_{\ell'}^{m'} \ , \tag{3.4}$$

where a, b are the CMB T, E, B modes, n_L^{ab} is a normalisation factor introduced to obtain an unbiased estimator and $W(a,b)$ is a weighting factor which leads to the noise $N_L^{aa'bb'}$ on the power spectrum[5].

Let us now describe from a physical point of view the CMB lensing process and its sensitivity to the underlying expansion history. For a full mathematical treatment we refer to earlier works [25, 30, 121]. As the Hubble expansion rate grows in the past with respect to ΛCDM, the cosmic expansion rate increases. Its value at the epoch of structure formation will determine how efficient the process of structure formation is, and consequently the abundance of available lenses: the lower is the Hubble rate in that epoch, the lower the friction represented by the expansion with respect to structure formation, the higher the number of lenses will be. As noticed by [9], the latter occurrence is rather sensitive to the DE abundance at the epoch at which lensing is most effective, $z \in [1,3]$, and rather independent of the

[5]We will specify the extraction method followed here (and therefore our choice of W) in the next Section.

DE properties at earlier and later epochs than that, simply because by geometry, the lensing cross section peaks about halfway between sources and observer.

The distribution of lenses, following the power spectrum of density perturbations, as well as the geometrical properties mentioned above, determine the efficiency of CMB lensing to peak on arcminute angular scales, corresponding to structures from a few to about 10^2 comoving Mpc. Being a non-linear effect, lensing redistributes primordial anisotropy power of single multipoles at last scattering on a finite interval of scales. The net effect on T and E is a smearing of acoustic peaks and the dominance in the damping tail region, corresponding to multipoles of $\ell \gtrsim 1000$, where primordial anisotropies die out because of diffusion damping, and the only power comes from larger scales because of lensing.

As already discussed previously, for $B-$modes the effect is rather different. In Fig. 3.2 the various contributions to $B-$modes are shown, coming from PGWs on degree and super-degree angular scales, and from lensing on arcminute ones. The latter effect arises because a fraction of $E-$modes is transferred to B because of the deflection itself. The sensitivity of this process to the underlying DE properties is described in Fig. 3.3, where the T and B spectra are shown for various cases. The geometric shift in T is due to the change in comoving distance to the last scattering, given by the generalisation of Eq. 2.12

$$D_L = H_0^{-1} \int_0^{z_{LS}} dz \left[\Omega_m (1+z)^3 + \Omega_{DE,0} e^{3 \int_0^z dz' \frac{1+w(z')}{1+z'}} \right]^{-1/2} \tag{3.5}$$

where H_0 is the Hubble parameter, Ω_m is the matter abundance today relative to the critical density and the contributions from radiation and curvature are neglected. Clearly, the same value of D_L can be obtained with various combinations of parameters, including DE, creating the so called *projection degeneracy*, already addressed in [9]. The lensing, for $B-$modes in particular, shown in the right panel, is capable of breaking it, because of its sensitivity to the DE abundance at the epoch in which its cross section is non-zero. Indeed, looking again at Fig. 3.1, we see that the DE density at the epoch we are considering follows an opposite behaviour with respect to the curves represented in Fig. 3.3: the lower the curve, the higher the value of the expansion rate at the relevant epoch for lensing leading to an increasing suppression of the power, the higher the DE density, as already discussed above.

It is already well known [34] that the gravitational lensing signal constitutes a fundamental contaminant in the PGWs spectrum. The latter is parametrised by the ratio between the tensor and scalar power in the primordial perturbation power spectra, r. As for scalars, the power spectrum of PGWs is also characterised by a spectral index. We work here in the hypothesis of single field inflationary models, which relate the tensor spectral index to r, without introducing any additional parameter; a discussion on parameter estimation without this assumption may be found in [122, 123].

The aim of this analysis is trying to infer how a simultaneous constraint can be affected by the presence of both signals in data, and in particular to determine

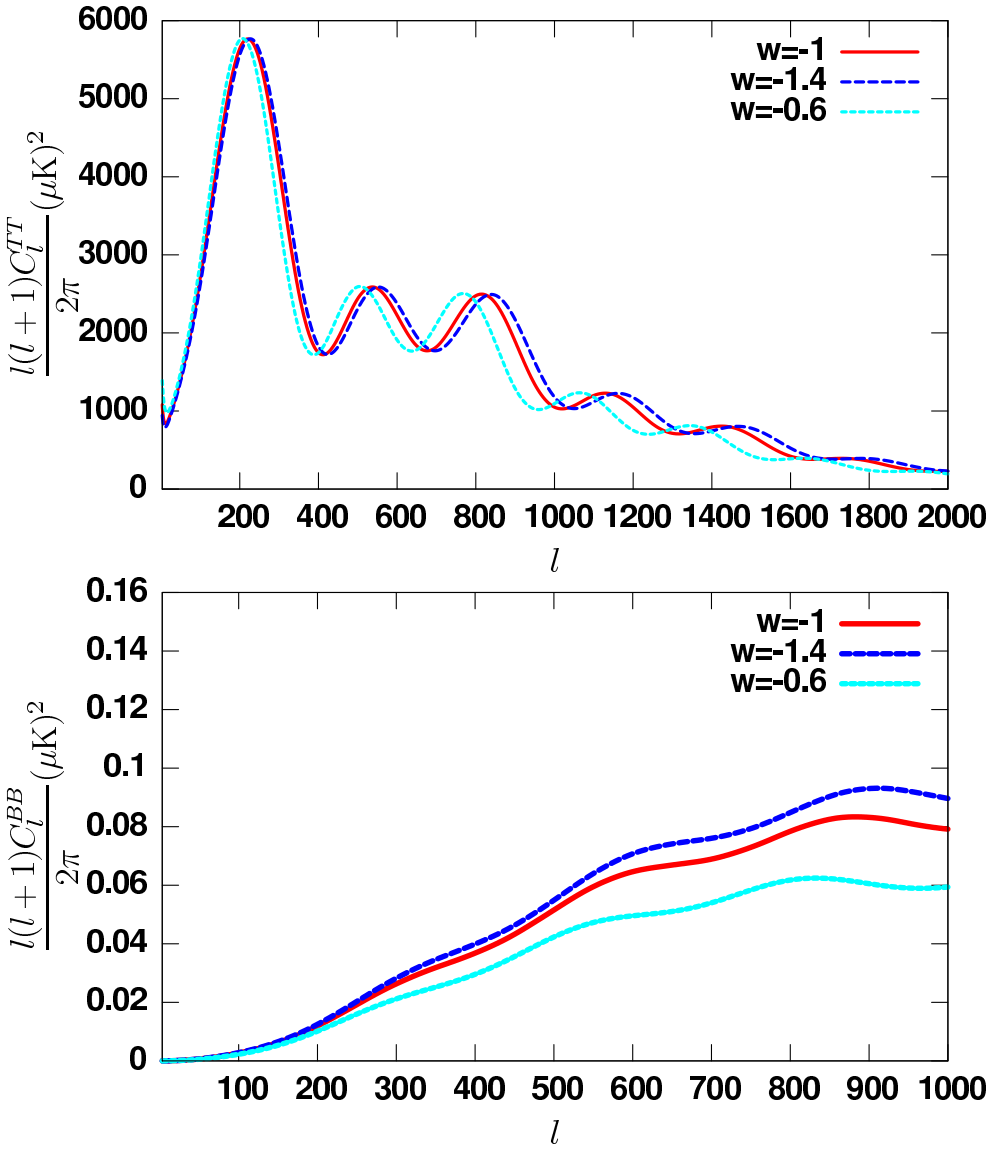

Figure 3.3: Top panel: Variation of the $T-$mode spectrum with different values of w. Bottom panel: Variation of the $B-$mode spectrum with different values of w.

the degradation, if any, of the constraint on r as the background expansion is allowed to vary according to a CPL parametrisation. As we have seen, this heavily affects the lensing peak of the CMB: for a better quantification of this point, it is shown in Fig. 3.4 how the ratio of the two contributions at the peak of the PGWs power, corresponding to $\ell \simeq 100$, can vary macroscopically because of the variation in the DE dynamics, reaching 50%. It is clear that it is necessary to study the parameter space represented by r, w_0, w_a jointly, in order to understand the constraining power based on data on CMB $B-$modes.

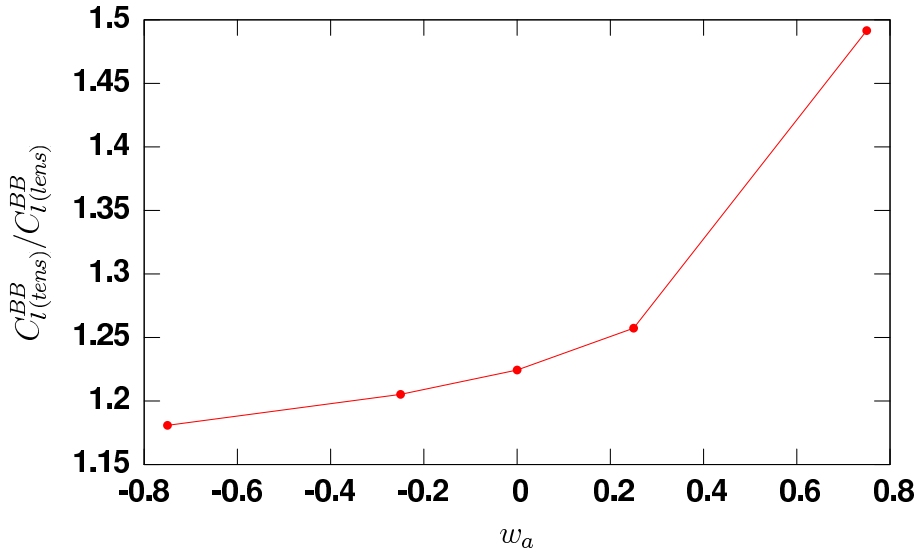

Figure 3.4: Ratio between the primordial $B-$modes ($r = 0.05$) and lensing generated $B-$modes at $\ell = 100$ with different expansion histories with w_0 fixed to -1.

3.2 Simulated data and analysis

In order to obtain a forecast for different parameters using nominal instrumental performances, a Fisher matrix approach is often adopted for estimating covariances. However, this approach is rigorously valid only if the likelihood shape of parameters is Gaussian. In this case, as it will be shown, the shape of the likelihood for r deviates substantially from a Gaussian; in order to avoid inaccuracies, as it was pointed out in recent works [124] such a simplification is here avoided. Another reason for doing so is that different datasets are considered here, described later in this Section, and it cannot be assumed that no degeneracies will arise from this combination. For these reasons, our approach consists in computing the full likelihood shapes by using a Markov chains approach. We exploited extensively the publicly available software package `cosmomc`[6] for Markov Chain Monte Carlo (MCMC) analysis of CMB datasets [125].

We create simulated CMB datasets for T, E and $B-$modes, adopting the specifications of PLANCK [41], EBEX [115] and POLARBEAR [116] experiments. In Table 3.2 the relevant parameters adopted are listed. The fiducial model for the standard cosmological parameters is the best fit from the WMAP seven years analysis [126], concerning flat ΛCDM parametrising the abundances of CDM and baryons plus leptons ($h^2\Omega_c$, $h^2\Omega_b$, respectively), $100 \cdot \theta_*$ (we had defined θ_* as the ratio of the sound horizon to the angular diameter distance), the optical depth τ of cosmological reionisation, the spectral index n_s and amplitude A_s of the primordial power spectrum of density perturbations, the parameters for evolving DE w_0, w_a. In the considered case the effects that a generalised expansion history has on the

[6] `http://cosmologist.info`

cases of a null as well as a positive detection of r are addressed. In Table 3.1 the values used to compute the simulated spectra are shown.

$h^2\Omega_b$	$h^2\Omega_c$	$100 \cdot \theta_*$	τ	n_s	A_s	w_0	w_a
0.02258	0.1109	1.0388	0.087	0.963	$2.43 \cdot 10^{-9}$	-1	0

Table 3.1: Set of cosmological parameters and adopted values for the cases $r = 0$ and $r = 0.05$ of simulated data.

Therefore, two different fiducial models were adopted concerning the amplitude of PGWs, corresponding to their absence ($r = 0$) and to $r = 0.05$. The latter case corresponds to a detectable value also in a more realistic case in which data analysis includes foreground cleaning and power spectrum estimation is chained to the MCMCs [127, 128].
Using these sets we compute the fiducial power spectra C_ℓ^i with $i = TT, TE, EE, BB$, in order to compare them with the theoretical models generated by exploring the parameter space. In this work we make use of the `cosmomc` package for that. We add a noise bias to these fiducial spectra, consistently with the mentioned instrumental specifications.

For each frequency channel which is listed in Table 3.2, the detector noise considered is $w^{-1} = (\theta\sigma)^2$, where θ is the FWHM (Full-Width at Half-Maximum) of the instrumental beam if one assumes a Gaussian and circular profile and σ is the sensitivity on the temperature measurement. To each of the C_ℓ coefficients the added contribution from the noise is given by

$$N_\ell = w^{-1} e^{(\ell(\ell+1)/\ell_b^2)}, \tag{3.6}$$

where ℓ_b is given by $\ell_b \equiv \sqrt{8\ln 2}/\theta$. The MCMCs were conducted by adopting a convergence diagnostic based on the Gelman and Rubin statistics [129]. We sample six cosmological parameters ($\Omega_b h^2$, $\Omega_c h^2$, τ, n_s, A_s), the w_0 and w_a DE parameters, and r adopting flat priors. We make use of priors coming from different probes in the `cosmomc` package, specifically BAO [55, 130], SNe Ia data [131], results from the HST[7] [132].

In order to calibrate the pipeline, a ΛCDM model with $r = 0$, varying both the DE parameters w_0, w_a or keeping them fixed to a CC through the MCMCs is first analysed, considering for simplicity the combination of PLANCK and one sub-orbital experiment (POLARBEAR). The results in the $(\Omega_\Lambda, \Omega_m)$ plane are shown in Fig. 3.5 (top panel), showing the 1 and 2σ contours for the case of a CC (green) and dynamical DE (blue). The decrease in constraining power due to the extra degrees of freedom is evident, although the shape of the contour regions is rather stable. The given interpretation is that the introduction of new degrees of freedom affects the precision on the measurement of the two parameters considered. On the other hand, the distance to last scattering is degenerate between cosmological

[7] Hubble Space Telescope

abundances and expansion history, resulting in a geometric degeneracy for the non-lensed pure CMB dataset. The datasets forecasted here contain both CMB lensing measurements, as well as external data on the recent expansion history; we see here how this procedure eliminates such degeneracies. The residual effect is represented by a loss of precision due to the higher dimension of the parameter space, accounting now for a dynamical DE. We further investigate this point in the bottom panel of Fig. 3.5, where the results in presence (green) or absence (blue) of the SNe Ia measurements are shown, confirming the substantial relevance of external measurements of the expansion history at low redshift, as anticipated in earlier works [8].

Experiment	Channel	FWHM	ΔT/T
PLANCK	70	14'	4.7
	100	9.5'	2.5
	143	7.1'	2.2
	217	5.0'	4.8
$f_{sky} = 0.85$			
EBEX	150	8'	0.33
	250	8'	0.33
	410	8'	0.33
$f_{sky} = 0.01$			
POLARBEAR	90	6.7'	0.41
	150	4.0'	0.62
	220	2.7'	2.93
$f_{sky} = 0.03$			
CMBPOL	70	12'	0.148
	100	8.4'	0.151
	150	5.6'	0.177
$f_{sky} = 0.85$			

Table 3.2: PLANCK, EBEX, POLARBEAR and CMBPOL performance specifications. Channel frequency is given in GHz, beam FWHM in arcminutes, and the sensitivity for T per pixel in μK/K. The polarisation sensitivity for both E and $B-$modes is $\sqrt{2}\Delta T/T$.

It is interesting to compare the present case in which lensing $B-$modes are probed directly by CMB sub-orbital experiments with the case in which the lensing is extracted from all sky CMB anisotropy maps as expected by adopting the nominal performance of operating (PLANCK) and proposed post-PLANCK polarisation dedicated CMB satellites (CMBPOL and PRISM [133, 134]); the latter cases will give us an estimate of the improvement in the constraining power on w_0, w_a as a function of the satellite instrumental specifications. A similar approach has already been applied to the T spectrum by the SPT collaboration in [45]; the case for this analysis is different since the focus is set on the $B-$modes. We create simulated datasets for PLANCK and CMBPOL, adopting nominal performances as in the previous case, but adding the forecasted lensing potential measurements.

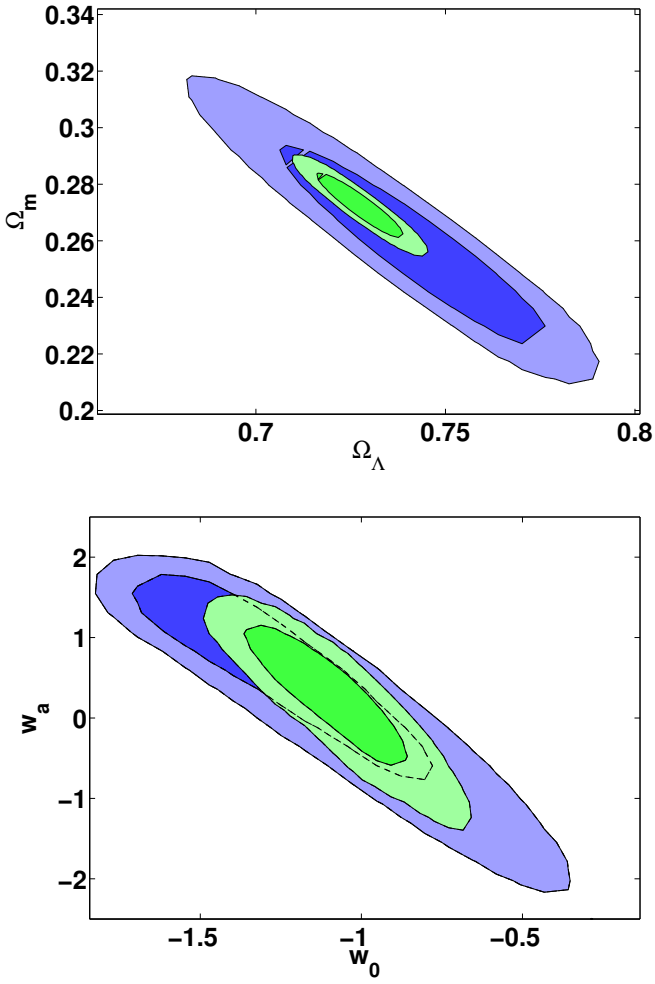

Figure 3.5: Test analysis with $r = 0$, evolving DE. Top panel: 1 and 2σ contours $\Omega_m - \Omega_\Lambda$ diagram. In blue the combination POLARBEAR + PLANCK with dynamical DE, in green POLARBEAR + PLANCK, with ΛCDM. Bottom panel: 1 and 2σ contours for $w_a - w_0$. In blue the results obtained when SNe Ia are not included, in green when SNe Ia data were considered.

Our aim is to quantify, in these cases, the efficiency on the determination of the expansion parameters w_0 and w_a, and how they scale with satellite instrumental capabilities, reaching the cosmic variance limit also for polarisation as in the cases of planned post-PLANCK satellite CMB experiments; therefore we keep $r = 0$ fixed and let the CPL parameters vary. The lensing extraction method presented in [120] is used, in which the authors construct the weighting factor W of Eq. 3.4 as a function of CMB power spectra C_{ab}, with $ab = TT, TE, EE, EB, TB$. The BB spectrum is excluded because the adopted method is only valid when the lensing contribution is negligible compared to the primary anisotropies; this assumption fails for $B-$modes, which are not considered in this analysis, by modifying `cosmomc` according with [135]. This aspect, as well as the instrumental sensitivity, implies that lensing measurements in this case come mainly from sub-degree T and E anisotropy data. We study the constraining power on CPL parameters from

PLANCK data in three cases: first, when lensing measurements are used, second, without lensing, but with the inclusion of the priors introduced above (BAO, HST, SNe Ia), and finally using both. We performed this analysis also on a CMBPOL-like experiment using the specifications in [133]; the major uncertainty on the data from such an experiment will be due to cosmic variance. Results are presented in Table 3.3.

PLANCK	CMB+lensing extraction	CMB+priors	CMB+lensing extraction+priors
$\Delta(w_0)$	0.5	0.2	0.2
$\Delta(w_a)$	1.1	0.6	0.6
CMBPOL	CMB+lensing extraction	CMB+priors	CMB+lensing extraction+priors
$\Delta(w_0)$	0.4	0.159	0.150
$\Delta(w_a)$	1.0	0.57	0.497

Table 3.3: 1σ uncertainties on CPL parameters w_0, w_a for PLANCK and for a CMBPOL specifications when using lensing extraction, when using external priors and when combining both, in the case $r = 0$.

Let us focus first on the comparison between CMB satellite lensing measurements and the case in which the lensing is probed through the lensing dominated part of the $B-$mode spectrum. As it can be seen comparing with the contours in Figure 3.5, the relevance of lensing measurements is comparable in the two cases; moreover, it is found that the priors have a comparable relevance. We conclude that satellite lensing measurements using T and E, and sub-orbital ones directly accessing lensing $B-$modes, have a comparable capability for constraining the expansion history. Both cases are relevant to study, as the impact of non-idealisations including systematics as well as removal of foreground emissions may produce different outcomes [135, 136].

Let us now discuss the differences between the case of PLANCK, which is a cosmic variance limited experiment for total intensity, with respect to the enhanced capability of planned post-PLANCK satellites, approaching the same limit for polarisation as well. As the results show, the improvement in the instrumental specification does cause an enhancement of the constraining capability corresponding to a factor 20% for w_0 and 10% for w_a; when priors are considered, the results improve by a factor of about 6% for w_0 and 15% for w_a. We conclude that the improvement is sensible but does not change the order of magnitude of the forecasted precision, and we argue that this is consistent with the fact that PLANCK is cosmic variance limited in total intensity, which is the dominant part of the CMB anisotropy signal. In the following we focus on the capability of constraining the expansion parameters using the B-modes, in order to study if new degeneracies arise when the relative amplitude between PGWs (through variations of r) and the lensing spectrum (as traced by lensing $B-$modes) vary at the same time.

3.3 Results

The recovery of the primordial tensor to scalar ratio is addressed here, performed while varying the cosmological expansion history. As we already pointed out, we consider two cases, for a null ($r = 0$) and positive ($r = 0.05$) detection. In both cases, the fiducial DE model is ΛCDM, and the generalised expansion history is parametrised by w_0 and w_a. In order to verify the relevance of sub-orbital probes, probing the lensing peak in the $B-$mode spectrum, we consider the case of pure satellite CMB data separately from the one with joint satellite and sub-orbital probes.

The results on r as 2σ upper limits and 1σ statistical uncertainties in the null and positive detection cases respectively, as well as the corresponding constrains on CPL parameters are shown in Table 3.4. In the case with a non-vanishing fiducial value of r, a change in the MCMC recovered value of r is present when the theoretical model or the experimental configuration are changed. In order to address the reason of the differences in the recovered mean value of r we computed the Gelman and Rubin indicator for the chains we performed, finding that the differences we see can be ascribed to fluctuations in the MCMC procedure (see e.g. [137] for a more specific discussion on this topic). Nevertheless, note that, as expected, the results obtained by adopting the nominal specifications of PLANCK are in agreement with [138] for ΛCDM. A first result concerns the quantification of precision loss of the recovery on r when a generalised expansion rate is considered, and when only satellite CMB data are considered.

This corresponds roughly to 10% for the null and about 5% for positive detections of r. The interpretation is related to the extra degrees of freedom considered, while as in the previous Sections, the lensing component of simulated spectra, as well as the priors on the expansion history from external probes, help reducing geometric degeneracies, leaving room only for an increase in the statistical error of the various measurements, which are quantified here. It is interesting now to look at the case when all the CMB probes are considered, verifying that the precision loss in this case falls below a detectable level. This result is uniquely related to the enhanced sensitivity of sub-orbital probes, allowing for a deeper study of the lensed component of CMB spectra, and in particular on the lensing peak in $B-$modes. Concerning the CPL parameters (w_0, w_a), it is possible to see in Table 3.4 how the constraints do not degrade switching from the $r = 0$ to the $r = 0.05$ simulated dataset. This shows, as previously stated, that there are no detectable degeneracies between r and CPL parameters in our considered datasets.

Moreover we can also notice how constraints on (w_0, w_a) do not improve much if we use sub-orbital experiments alongside satellite data to get better CMB sensitivity; this highlights the fact that the used priors, most of all the SNe Ia data, are crucial to constrain DE quantities.

These limits have been derived from one-dimensional contours, which are shown in Fig. 3.6, reporting the null detection case only, for simplicity, for r and the DE parameters, and restricting to the case of DE models with $w > -1$; it can be noticed how considering the whole CMB datasets yields an improvement

Experiments, fiducial	$r = 0$	$r = 0.05$
PLANCK with priors, ΛCDM	$r < 0.029$	$r = 0.057 \pm 0.022$
PLANCK with priors, CPL	$r < 0.031$	$r = 0.059 \pm 0.023$
all experiments, ΛCDM	$r < 0.025$	$r = 0.057 \pm 0.020$
all experiments, CPL	$r < 0.025$	$r = 0.056 \pm 0.020$
PLANCK with priors, CPL	$w_0 = -1.1 \pm 0.2$	$w_0 = -1.1 \pm 0.2$
all experiments, CPL	$w_0 = -1.1 \pm 0.2$	$w_0 = -1.1 \pm 0.2$
PLANCK with priors, CPL	$w_a = 0.3 \pm 0.6$	$w_a = 0.3 \pm 0.6$
all experiments, CPL	$w_a = 0.3 \pm 0.6$	$w_a = 0.2 \pm 0.6$

Table 3.4: 2σ upper limits and 1σ uncertainties for the measurements of r for the null and positive detection cases, and 1σ uncertainties for the measurements of the CPL parameters w_0, w_a for the different expansion models and dataset combinations.

on the detection of r, reflecting Table 3.4, while almost no difference is noticeable between the cases of dynamical DE or Λ. Looking at the first panel in Fig. 3.6 one can in particular appreciate how the shape in the likelihood for r is non-Gaussian, justifying our choice of going through a MCMC analysis rather than relying on a Fisher matrix approach. For DE parameters, we notice no particular improvement in considering the case of all CMB or pure satellite datasets alongside SNe Ia, BAO and HST data. The same holds when looking at two-dimensional contours, shown in Fig. 3.7 in the (r,w_0), (r,w_a) and (w_0,w_a) planes, for the null (blue) and positive (red) detection cases: in none of the three panels a significant improvement in DE parameter recovery is shown, even allowing for cosmologies with $w < -1$. We also notice that no degeneracies among these parameters are detectable with the datasets we consider. The figures also quantify the precision achievable on DE parameters, being comparable and of the order of a few ten percents, for both parameters and both fiducial models.

Finally, we show other relevant two-dimensional contour plots for the case of null detection (Fig. 3.8) and for the $r = 0.05$ fiducial value (Fig. 3.9), highlighting how with the data considered here it is not possible to detect any degeneracy between the primordial tensorial mode parameter r and other cosmological parameters. Despite this remarkable result, we stress that our results concern a nominal performance of the various datasets, and in particular do not consider foreground cleaning or other systematic effects, which were pointed out as possible sources of bias for r in previous works [127, 128, 139].

3.4 Concluding remarks

The PGWs and lensing power constitute the dominant effects for the $B-$mode polarisation in the anisotropies of the CMB. While the former is dominated by the physics of the early Universe, parametrised through the primordial tensor-to-scalar ratio r, the latter is instead due to structure formation, and thus influenced by the

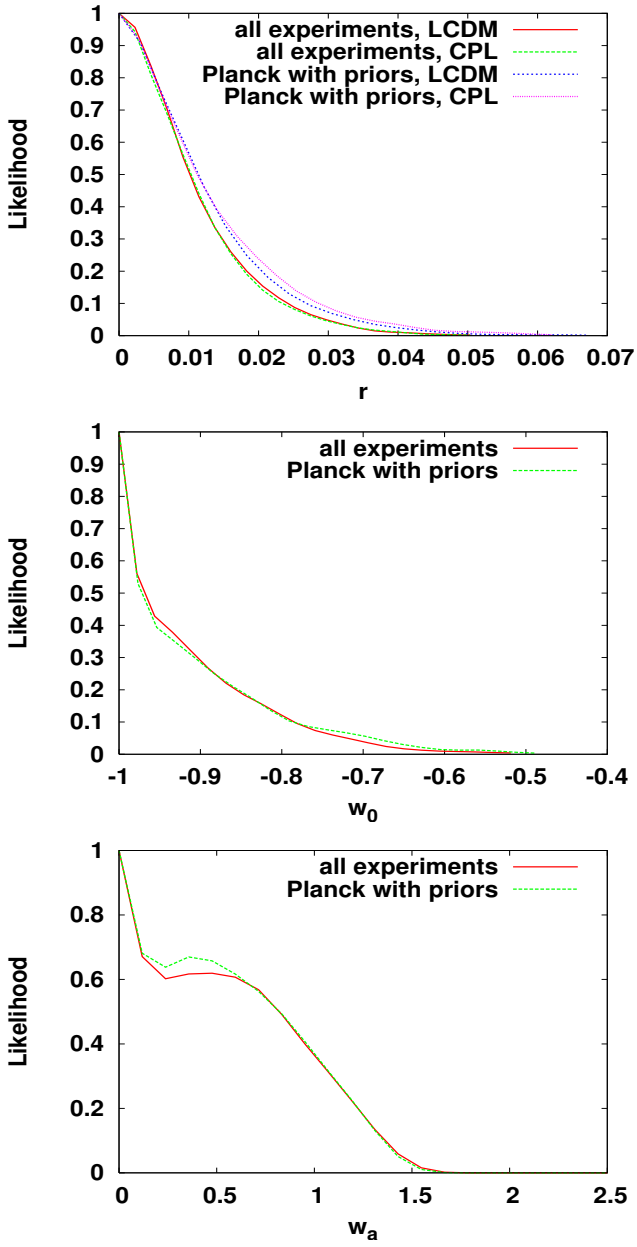

Figure 3.6: One-dimensional contours for r, w_0 and w_a respectively, in the case of null detection for r; all plots show differences when using satellite, or all CMB datasets; the plot for r also includes the ΛCDM cases.

expansion rate at the epoch of the onset of cosmic acceleration. This, in turn, is dependent on the underlying dynamics of DE. Despite both signals being present in the CMB $B-$modes, their joint measurement in terms of parameter estimation was never considered, and the results presented constitute a first step in this direction.

To begin, the lensing relevance for constraining our parametrisation of the expansion history is addressed, assuming no PGWs. We find comparable results when the lensing is extracted from T and E data and when the lensing is more directly inspected through lensing $B-$modes, by forthcoming satellite and sub-

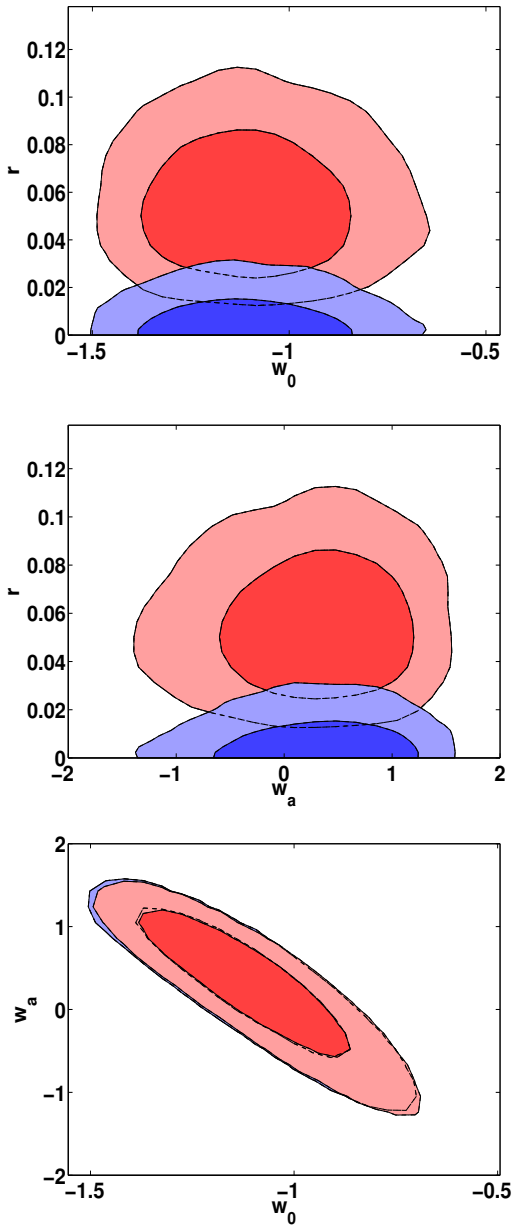

Figure 3.7: Top panel: 1 and 2σ contours $w_0 - r$ diagram for the combination of all considered datasets. In blue, the upper limit on the simulated data with fiducial value $r = 0$. In red, the case of simulated data with fiducial value $r = 0.05$. Middle panel: 1 and 2σ contours $w_a - r$ diagram. In blue, the upper limit on the simulated data with fiducial value $r = 0$. In red, the case of simulated data with fiducial value $r = 0.05$. Bottom panel: 1 and 2σ contours $w_0 - w_a$ diagram. In blue, the constraints on the simulated data with fiducial value $r = 0$. In red, the case of simulated data with fiducial value $r = 0.05$.

orbital data, respectively, both for a PLANCK-like experiment and for a CMBPOL-like experiment. Focusing on the latter case, in which the two processes directly compete for detection in $B-$modes, we quantify the constraining power on the abundance of PGWs which is expected from combined forthcoming satellite and sub-orbital experiments probing CMB polarisation in cosmologies with generalised

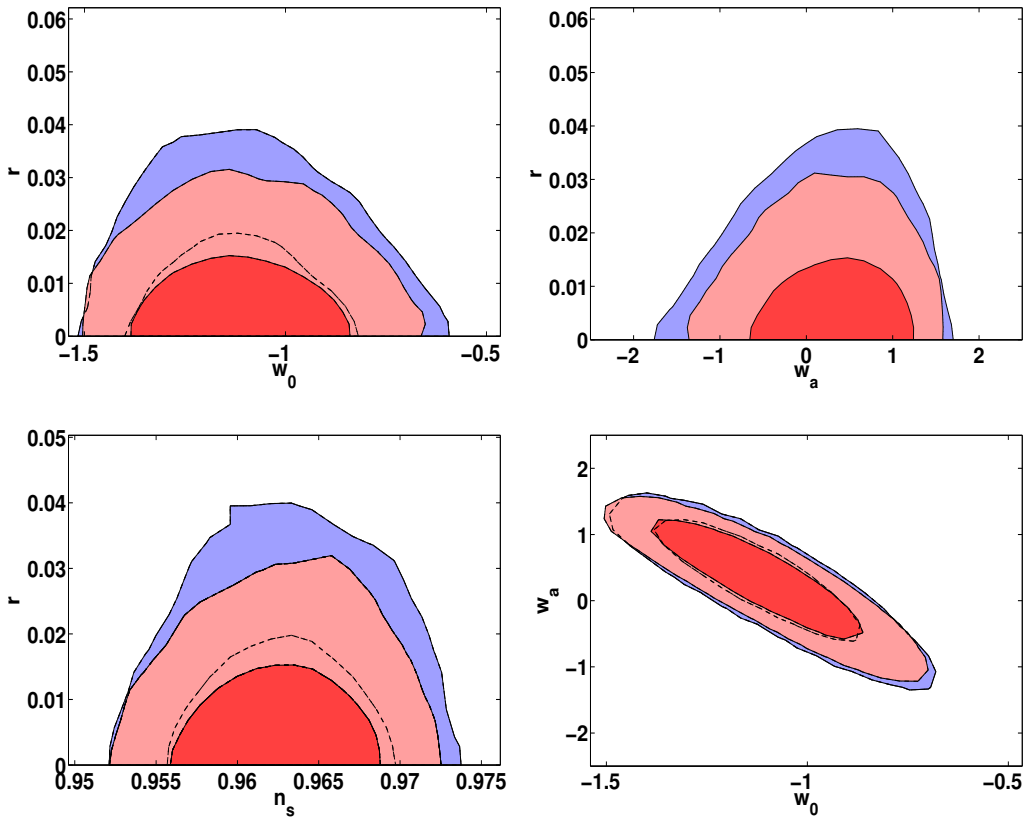

Figure 3.8: Results from the analysis on the $r = 0$ fiducial value simulated dataset. In all plots, blue contours represent pure satellite CMB data, while the red ones include sub-orbital ones as well. From left to right, from top to bottom. 1. $1-2\sigma$ contours for $r - w_0$. 2. $1-2\sigma$ contours for $r - w_a$. 3. $1-2\sigma$ contours for $r - n_s$ for dynamical DE. 4. $1-2\sigma$ contours for $w_0 - w_a$.

expansion histories, parametrised through the present and first redshift derivative of the DE equation of state, w_0 and w_a, respectively. We find that in the case of pure satellite measurements, corresponding to the PLANCK nominal performance, the constraining power on PGWs power is weakened by the inclusion of the extra degrees of freedom, resulting in an increase of about 10% of the upper limits on r in fiducial models with no PGWs, as well as a comparable increase in the error bars in models with non-zero tensor power.

Furthermore, the possibility to perform lensing extraction from satellite data using a full sky estimator is explored and we recovered that, at least for upcoming experiments, when combining CMB with external priors, the results yielded are not significantly different from what obtained without lensing extraction. It is to remember that, for the moment, the algorithm of lensing extraction implemented in the `cosmomc` package only analyses the temperature spectrum, neglecting the information coming from polarisation.

The inclusion of sub-orbital CMB experiments, capable of mapping the $B-$mode power up to the angular scales which are affected by lensing, has the effect of

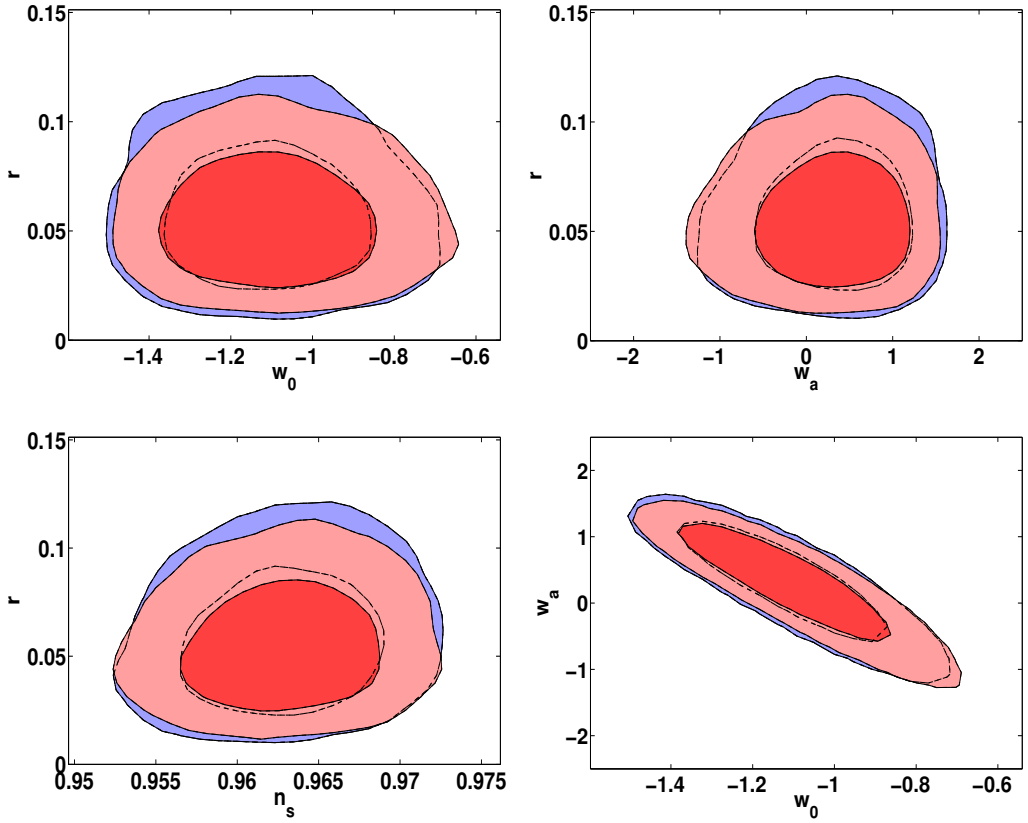

Figure 3.9: Results from the analysis on the $r = 0.05$ fiducial value simulated dataset. In all plots, blue contours represent pure satellite CMB data, while the red ones include sub-orbital ones as well. From left to right, from top to bottom. 1. $1-2\sigma$ contours for $r - w0$. 2. $1-2\sigma$ contours for $r - w_a$. 3. $1-2\sigma$ contours for $r - n_s$ for dynamical DE. 4. $1-2\sigma$ contours for $w_0 - w_a$.

making such loss of constraining power vanishing below a detectable level. We interpret these results as a joint effect of the CMB and external datasets: the former are able, in particular with the data from sub-orbital probes, to access the region of $B-$modes which is lensing dominated, and therefore sensitive to the DE abundance at the onset of acceleration; the latter, as the case of SNe Ia and HST data, are on the other hand strongly constraining the dynamics of cosmic expansion at present. By inspecting the constraints on all cosmological parameters, including those parametrising the expansion history, we also show that the chosen datasets do not highlight new degeneracies in the parametrisation we consider.

These results indicate that the combination of satellite and sub-orbital CMB data, with the available external data useful to inquire the late time expansion history, can be used for constraining jointly the dynamics of the DE as well as the primordial tensor-to-scalar ratio, with no new degeneracies or significant loss of sensitivity in particular on r with respect to the case in which a pure CC determines the late time cosmological expansion. The assumptions of course include the nominal performance of these experiments, and no realistic data analysis consisting in

the inclusion of foregrounds in the CMB data, as well as systematic errors have been considered.

Possible extensions for this work would be to further investigate this phenomenology in specific DE models, and considering the role of future surveys in giving more accurate constraints on the expansion history, also considering different approaches, e.g. delensing techniques [34, 140, 141].

Motivated by these results, we will push the simulation of CMB lensing extraction to a higher level of sophistication by implementing a lensing extraction algorithm. Our aim is to target the small scales, and quantify the precision of the proposed pipeline on CMB lensing realisations based on real structure from N-body simulations, with a map-making procedure based on ray tracing.

4

Characterising CMB lensing simulations for next generation surveys

In the past Chapters we have discussed the characteristics of the CMB lensing effect on various cosmological observables, focusing in Chapter 2 on extensions of standard physics that might be inquired using the information coming from this phenomenon: the time evolution of DE and the presence in our Universe of massive neutrinos. In Chapter 3 we investigated the influence of CMB lensing acting as a contaminant on the constraining power on primordial tensor modes, and how ignoring the simultaneous presence of the two signals in the $B-$modes of CMB can degrade our constraining ability on the inflationary parameter r. At this point, it is relevant to discuss the capability of characterising the lensing signal as a specific tool for increasing the overall information we can extract from a cosmological dataset.

This is especially true in view of the next generation surveys targeting the recent Universe: as argued in the previous Chapters, CMB lensing is able to couple different angular modes of the CMB, giving rise to a non-Gaussian, distinctive signature in the recovered maps. This perturbs the original distribution of anisotropies with a late-time contribution which carries the imprint of the evolving LSS; in this way the CMB carries not only a crucial amount of information about the Early Universe, but also from the recent, non-linear phases of evolution, whose expansion is dominated by the DE component. The relevant information can be extracted with higher precision when combining data delivered by different experiments, and/or relative to different observables; this process adds statistical significance and reduces the contamination from instrumental or astrophysical systematics.

The next generation of data surveys will face the community with new challenges: the non-linear regime of gravitational collapse, dominating the very small angular scales, is still not completely understood; achieving realistic simulations even of the highly non-linear regimes of the matter power spectrum represents a challenge we need to undertake to exploit fully the experimental data from an experiment such as EUCLID, and to combine them with high precision CMB probes.

More and more efforts are being undertaken for measuring second order effects, i.e. physical phenomena which occur after the last scattering surface, the epoch at which CMB photons decouple from the rest of the system and the first

order anisotropies are imprinted. In order to constrain the dark cosmological components, and the DE in particular, the observation and characterisation of the weak lensing of the CMB induced by forming structures along the line of sight of photons at the epoch in which the DE overcomes the CDM component is gathering more and more attention. CMB lensing, in fact, allows us to break the degeneracies present in the measurements of cosmological parameters through CMB observations only [142] as well as providing more constraining power on the same parameters [118, 143].

Moreover, as lensing is closely related to the underlying gravitational theory, it can be used to test the possibility that the late-time accelerated expansion is not given by a DE component, but rather by a modified theory of gravity [119].

Among the possible effects on the matter power spectrum, it has been discussed in subsec. 2.2.3 the implications for cosmology of a non-zero value for the neutrino mass. The presence of relativistic, massive neutrinos, smears out structures below the free streaming scale in Eq. 2.29, and thus modify the structure of the lensing potential which will deflect the CMB, giving it a distinct signature.

In this scenario, our capability of understanding the lensing signal to extreme accuracy is most important, and a necessary condition for that is to be able to model it appropriately and to the accuracy needed by modern cosmological observations. In the recent past, efforts were made in order to simulate lensed CMB maps in the context of modern N-body simulations, which, once validated, have the potential and crucial capability of enabling us to estimate the constraining power which we will have from CMB lensing in particular on the underlying cosmological model [28] and most importantly in view of cross-correlating CMB lensing measurements with those of LSS which are responsible for the lensing itself, culminating with the launch of the EUCLID satellite in about one decade.

In this Chapter a progress on this line is illustrated: for the first time, the lensing signal in simulated CMB temperature and polarisation maps using ray-tracing through N-body simulations, in order to track the effects coming from non-linearities, is extracted and characterised in a range of angular scales $100 < \ell < 2000$. A flat sky lensing extraction pipeline, developed and exploited in [136], is applied onto CMB lensed maps constructed by performing ray-tracing in the Born approximation using the Millennium Simulations (MS) in [27, 144] and a first step for exploiting the information encoded in the lensing spectrum in order to constrain the underlying cosmology, in particular targeting N-body simulations of a Universe with massive neutrinos, is discussed. The discussion will follow the work published in [2], along with the presentation of unpublished material.

In Sec. 4.1 the details of the N-body simulations used to reconstruct the CMB maps are introduced and discussed, also specifying the methods used to produce the analysed maps. In Sec. 4.2 the theoretical background of CMB lensing, already discussed in Chapter 1, and the lensing extraction methods are recalled, detailing the formalism and the adopted procedure. Sec. 4.3 contains the application of the extraction pipeline on the CMB lensed maps obtained from the N-body simulations, assuming observational errors compatible with current and upcoming CMB surveys for a standard ΛCDM case; in Sec. 4.4 the results of the lensing extrac-

tion procedure applied to maps containing the effect of massive neutrinos on the lensing effect are presented. Finally, we discuss our results in Sec. 4.5.

4.1 From N-body simulations to CMB maps

In the following, the procedure of map-making with the lensing process enacted by simulated N-body structures is described. The notation and definitions used throughout Sec. 1.4 will be used, recalling some of the key concepts to facilitate the discussion.

Weak lensing of the CMB deflects photons coming from an original direction $\hat{\mathbf{n}}'$ on the last scattering surface to a direction $\hat{\mathbf{n}}$ on the observed sky, and the lensed CMB field is given by $\tilde{X}(\hat{\mathbf{n}}) = X(\hat{\mathbf{n}}')$ in terms of the unlensed field $X = T, Q, U$. The vector $\hat{\mathbf{n}}'$ is obtained from $\hat{\mathbf{n}}$ by moving its end on the surface of a unit sphere by a distance $|\nabla_\perp \phi(\hat{\mathbf{n}})|$ along a geodesic in the direction of $\nabla_\perp \phi(\hat{\mathbf{n}})$, where $\nabla_\perp$ is the angular derivative in the direction transverse to the line-of-sight pointing along $\hat{\mathbf{n}} \equiv (\vartheta, \varphi)$ [30, 31, 26, 145]. Here the field ϕ, and $|\nabla_\perp \phi(\hat{\mathbf{n}})|$ is assumed to be constant between $\hat{\mathbf{n}}$ and $\hat{\mathbf{n}}'$.

The lensed temperature and polarisation fields are given by

$$\begin{aligned} \tilde{T}(\hat{\mathbf{n}}) &= T\left[\hat{\mathbf{n}} + \hat{\nabla}\phi(\hat{\mathbf{n}})\right], \\ (\tilde{Q} + i\tilde{U})(\hat{\mathbf{n}}) &= (Q \pm iU)\left[\hat{\mathbf{n}} + \hat{\nabla}\phi(\hat{\mathbf{n}})\right]. \end{aligned} \tag{4.1}$$

In what follows we will consider only the *small angle scattering* limit, *i.e.* the case where the change in the comoving separation of CMB light rays, owing to the deflection caused by gravitational lensing from matter inhomogeneities, is small compared to the comoving separation between the *undeflected* rays. In this case it is sufficient to calculate all the relevant integrated quantities, *i.e.* the lensing potential and its angular gradient, the deflection angle, along the undeflected rays. The described limit corresponds to the Born approximation.

Under this condition, adopting conformal time and comoving coordinates [146], the integral for the projected lensing potential due to scalar perturbations in the absence of anisotropic stress reads

$$\phi(\hat{\mathbf{n}}) = -2\int_0^{D_\star} dD\, \frac{D_\star - D}{D D_\star}\, \Phi\left(D\hat{\mathbf{n}}, D\right), \tag{4.2}$$

where D and $D_\star$ are, respectively, the comoving angular diameter distances from the observer to the lens and to the CMB last scattering surface, and Φ is the physical peculiar gravitational potential generated by density perturbations [25, 26, 30, 147]. Let us notice that ϕ is connected to the convergence field κ via $\hat{\nabla}^2\phi = -2\kappa$.

If the gravitational potential Φ is Gaussian, the lensing potential is also Gaussian. However, the lensed CMB is non-Gaussian, as it is a second order cosmological effect produced by matter perturbations onto CMB anisotropies, yielding a finite correlation between different scales and thus non-Gaussianity. This is

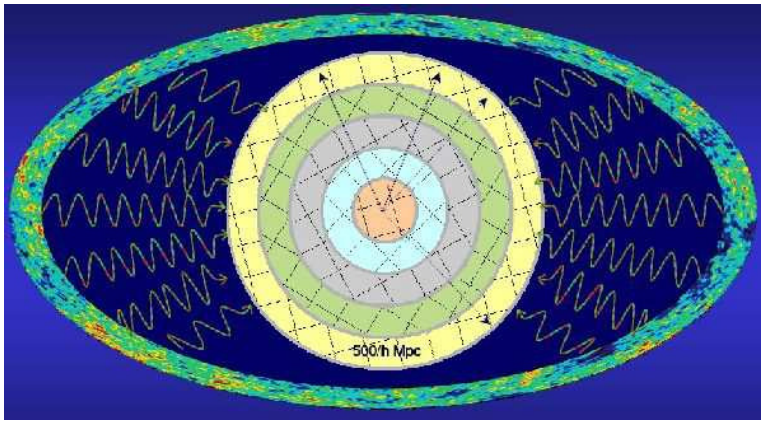

Figure 4.1: Sketch of the adopted stacking and randomisation process. The passage of CMB photons through the dark matter distribution of the Universe is followed by stacking the gravitational potential boxes of the MS, which are 500 h^{-1} Mpc on a side (comoving). Shells of thickness 500 h^{-1} Mpc are filled with periodic replicas of the box. All boxes (squares) that fall into the same shell are randomised with the same coordinate transformation (rotation and translation), which, in turn, differs from shell to shell. Figure from [27].

expected to be most important on small scales, due to the non-linearity already present in the underlying properties of lenses.

Here we analyse the full sky T, Q, U maps lensed by the matter distribution of the MS and generated by [144] via a modification of the publicly available `LensPix` code[1] (LP), described in [26]. In its original version this code lenses the primary CMB intensity and polarisation fields using a Gaussian realisation, in the spherical harmonic domain, of the lensing potential power spectrum as extracted from the publicly available Code for Anisotropies in the Microwave Background (`CAMB`[2]). The modification used here, performed by the authors, consists in forcing LP to deflect the CMB photons using the fully non-linear and non-Gaussian lensing potential realisation obtained from MS exploiting the procedure briefly summarised below, and presented in [144]; the reader is referred to this paper for further details.

The MS is a high resolution N-body simulation for a ΛCDM cosmology consistent with the WMAP 1 year results [148], carried out by the Virgo Consortium [149]. It uses about 10 billion collisionless particles with mass $8.6 \times 10^8 h^{-1}\mathrm{M}_\odot$, in a cubic region $500 h^{-1}$ Mpc on a side which evolves from redshift $z_* = 127$ to the present, with periodic boundary conditions. The map-making procedure developed in [27] is based on ray-tracing of the CMB photons in the Born approximation through the three-dimensional field of the MS peculiar gravitational potential. In order to produce mock lensing potential maps that cover the past light-cone over the full sky, the MS peculiar gravitational potential grids are stacked around the observer located at $z = 0$, and the total volume around the observer up to z_*

[1] `http://cosmologist.info/lenspix/`
[2] `http://camb.info/`

is divided into spherical shells, each of thickness $500h^{-1}$ Mpc: all the MS boxes falling into the same shell are translated and rotated with the same random vectors generating a homogeneous coordinate transformation throughout the shell, while randomisation changes from shell to shell. For a pictorial representation of the process, see Fig. 4.1. The peculiar gravitational potential at each point along a ray in direction $\hat{\mathbf{n}}$ is interpolated from the pre-computed MS potential grids which possess a spatial resolution of about $195h^{-1}$ kpc.

Being repeated on scales larger than the box size, the resulting weak lensing distortion lacks large scale power, which manifests itself in the lensing potential power spectrum as an evident loss of large scale power with respect to semi-analytic expectations, most noticeable at multipoles smaller than $\ell \simeq 400$. This has been cured in [27] by augmenting large scale power (LS-adding) directly in the angular domain, a procedure which we exploit here as well, since large scale modes in the lensing potential field are transferred to small scales in the CMB field, causing, e.g., the increasing of the temperature damping tail with respect to the unlensed field.

This mode coupling effect, which produces the characteristic non-Gaussianity of the CMB lensed field, is indeed exploited for the reconstruction of the underlying matter deflecting field. Nonetheless, in this case, we are mostly interested in studying the lensing reconstruction of the MS matter field, which corresponds to scales $\ell > 400$, and therefore, while still using all sky CMB lensed maps as input, we will exploit the flat sky lensing extraction pipeline for the reconstructed lensing potential output, as described in Sec. 4.2.

For the construction of the all sky lensed CMB input maps, in [144] the LS-adding technique has been implemented directly into the LP code. The spherical harmonics domain has been splitted into two multipole ranges: $2 \leq \ell \leq 400$, where the MS fails in reproducing the correct lensing potential power due to the limited box size of the simulation, and $\ell > 400$, where instead the power spectrum is reproduced correctly. On the latter interval of multipoles, the corresponding ensemble $\phi_{\ell m}^{\rm MS}$ of lensing potential spherical harmonic coefficients produced by the MS lens distribution has been extracted. The LP code has been modified to read and use these MS harmonic coefficients on the corresponding range of multipoles. On the interval $2 \leq \ell \leq 400$, instead, LP generates its own ensemble of spherical harmonic coefficients $\phi_{\ell m}^{\rm LP}$, which are a realisation of a Gaussian random field characterised by the `CAMB` semi-analytic non-linear lensing potential power spectrum inserted as input in the LP parameter file.

Since on multipoles $2 \leq \ell \leq 400$ the effects of non-Gaussianity from the non-linear scales are negligible and the $\phi_{\ell m}$ are independent, every time that we run the MS-modified-LP, we generate a joined ensemble of $\tilde{\phi}_{\ell m}$, where $\tilde{\phi}_{\ell m} = \phi_{\ell m}^{\rm LP}$ for $0 \leq \ell \leq 400$ and $\tilde{\phi}_{\ell m} = \phi_{\ell m}^{\rm MS}$ for $l > 400$. This technique reproduces correctly the non-linear and non-Gaussian effects of the MS non-linear dark matter distribution on multipoles $\ell > 400$, including at the same time the contribution from the large scales at $\ell \leq 400$, where the lensing potential follows mostly the linear trend.

To generate the lensed T, Q, U fields from the MS-modified-LP code, the

method described in [26] is adopted, using a high value of the multipole ℓ_{max} to maximise the accuracy. This allows running the simulation several times without excessive consumption of CPU time and memory. We work under the assumption that tensor modes are absent in the early Universe, so that the produced $B-$mode polarisation is due only to the power transfer from the primary scalar $E-$modes into the lensing induced $B-$modes. We choose $\ell_{max} = 6143$ and a `HEALPix`[3] pixelisation parameter $N_{side} = 2048$, which corresponds to an angular resolution of $\sim 1.72'$ [150], with $12N_{side}^2$ pixels in total.

4.2 CMB lensing extraction

As mentioned in Sec. 4.1, the flat-sky approximation is adopted here for the reconstruction of the lensing potential. In this limit the lensing potential can be written as [145]

$$\phi(\hat{\mathbf{n}}) = \int \frac{d^2L}{(2\pi)^2}\phi(\mathbf{L})e^{i\mathbf{L}\cdot\hat{\mathbf{n}}} \tag{4.3}$$

where the polar and azimuthal angles have been replaced by the displacement $\boldsymbol{\ell}$. The corrections due to lensing in the Fourier moments of temperature and polarisation fields can be expressed, at the linear order in ϕ, as [30]

$$\begin{aligned}
\delta\tilde{T}(\boldsymbol{\ell}) &= \int \frac{d^2l'}{(2\pi)^2} T(\boldsymbol{\ell}')W(\boldsymbol{\ell}', \mathbf{L}), \\
\delta\tilde{E}(\boldsymbol{\ell}) &= \int \frac{d^2l'}{(2\pi)^2} \Big[E(\boldsymbol{\ell}')\cos 2\varphi_{\ell'\ell} - B(\boldsymbol{\ell}')\sin 2\varphi_{\ell'\ell}\Big] W(\boldsymbol{\ell}', \mathbf{L}), \\
\delta\tilde{B}(\boldsymbol{\ell}) &= \int \frac{d^2l'}{(2\pi)^2} \Big[B(\boldsymbol{\ell}')\cos 2\varphi_{\ell'\ell} + E(\boldsymbol{\ell}')\sin 2\varphi_{\ell'\ell}\Big] W(\boldsymbol{\ell}', \mathbf{L}),
\end{aligned} \tag{4.4}$$

where the azimuthal angle difference is $\varphi_{\ell'\ell} \equiv \varphi_{\ell'} - \varphi_{\ell}$, $\mathbf{L} = \boldsymbol{\ell} - \boldsymbol{\ell}'$, and

$$W(\boldsymbol{\ell}, \mathbf{L}) = -[\boldsymbol{\ell}\cdot\mathbf{L}]\phi(\mathbf{L}). \tag{4.5}$$

These equations show that lensing couples the gradient of the primordial CMB modes $\boldsymbol{\ell}'$ to that of the observed modes $\boldsymbol{\ell}$. This is one of the key features of lensing, as it couples modes with different multipole on the sky, giving rise to a non-Gaussian component in the lensed fields, despite the potential generating the deflection obeying a Gaussian statistics.

Furthermore, even if primordial $B-$modes are vanishing, $B(\boldsymbol{\ell}') = 0$, lensing generates $B-$mode anisotropies in the observed map given the leakage from the E and $T-$modes.

[3] `http://healpix.jpl.nasa.gov/`

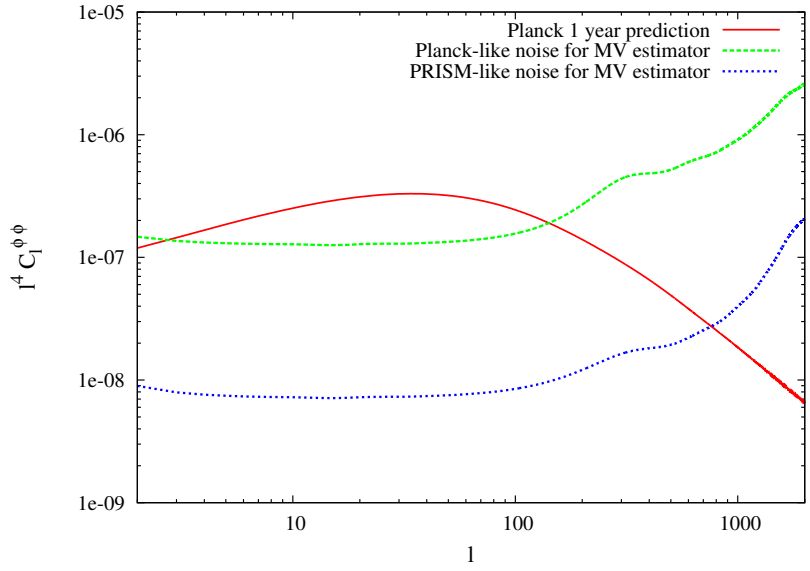

Figure 4.2: Noise spectrum for different experimental specifications. For graphical purposes we show the convergence power spectrum which is connected to the potential through $C_\ell^{\kappa\kappa} = \ell^4 C_\ell^{\phi\phi}$. Here the prediction for the convergence spectrum using as input cosmology the estimated cosmological parameters coming from PLANCK 1 year observations (red solid line), the noise for the minimum variance quadratic estimator for a PLANCK-like experiment (green dashed line) and the noise for the same estimator for a PRISM-like experiment (blue dashed line) are plotted.

We will consider noise in the CMB maps assumed homogeneous and white, characterised by a Gaussian beam. The power spectrum of the detector noise is [151]

$$C_\ell^{N,X} = \sigma_{pix}^2 \, \Omega_{pix}, \tag{4.6}$$

where σ_{pix} is the r.m.s. noise per pixel and Ω_{pix} is the solid angle subtended by each pixel. The observed CMB temperature and polarisation fields, $X \in [T, E, B]$, and their power spectra, $\tilde{C}_\ell^X$, are

$$\begin{aligned} \tilde{X}_\ell^{obs} &= \tilde{X}_\ell \, e^{-\frac{1}{2}\ell^2\sigma_b^2} + N_\ell^X, \\ \tilde{C}_\ell^{X,obs} &= \tilde{C}_\ell^X e^{-\ell^2\sigma_b^2} + C_\ell^{N,X}, \end{aligned} \tag{4.7}$$

where N_ℓ^X is the Fourier mode of the detector noise, and σ_b is related to the FWHM of the telescope beam, θ, as $\theta = \sigma_b\sqrt{8\ln 2}$.

We exploit the quadratic estimator formalism [152, 153, 154], built in the context of the convergence estimators [155, 156], in order to extract the lensing information from the simulated CMB maps used in the analysis.

The estimator is uniquely determined by requiring each component to be unbiased over an ensemble average of the CMB temperature and polarisation fields X and Y ($\langle\hat{\kappa}^{XY}(\hat{\mathbf{n}})\rangle = \kappa(\hat{\mathbf{n}})$) and the variance of the estimator to be minimal,

$$\langle\hat{\kappa}_\ell^{XY}\hat{\kappa}_{\ell'}^{*XY}\rangle = (2\pi)^2 \, \delta^D(\ell - \ell')(C_\ell^{\kappa\kappa} + N_\ell^{\kappa\kappa,XY}) \, , \tag{4.8}$$

where the $N_\ell^{\kappa\kappa,XY}$ term represents the noise contribution which is also predicted by the estimator, as we see below. In real space the convergence estimators are constructed on the basis of appropriate filters of the observed fields, weighted in the harmonic domain by their power spectra, which are given by [156]

$$\mathbf{G}_{XY}(\hat{\mathbf{n}}) = \int \frac{d^2\boldsymbol{\ell}}{(2\pi)^2}\, i\boldsymbol{\ell}\tilde{X}_{\boldsymbol{\ell}}^{obs} \frac{C_\ell^{XY}}{\tilde{C}_\ell^{X,obs}} \left\{ \begin{array}{c} e^{2i\varphi_\ell} \\ e^{2i\varphi_\ell} \end{array} \right\} e^{-\frac{1}{2}\ell^2\sigma_b^2 + i\boldsymbol{\ell}\cdot\hat{\mathbf{n}}} \tag{4.9}$$

$$W_Y(\hat{\mathbf{n}}) = \int \frac{d^2\boldsymbol{\ell}}{(2\pi)^2}\, \frac{\tilde{Y}_{\boldsymbol{\ell}}^{obs}}{\tilde{C}_\ell^{Y,obs}} \left\{ \begin{array}{c} e^{2i\varphi_\ell} \\ ie^{2i\varphi_\ell} \end{array} \right\} e^{-\frac{1}{2}\ell^2\sigma_b^2 + i\boldsymbol{\ell}\cdot\hat{\mathbf{n}}} \tag{4.10}$$

where $\varphi_{\boldsymbol{\ell}}$ is the azimuthal angle of the wave vector $\boldsymbol{\ell}$; the two phase factors in braces are applied when $Y = E, B$ respectively, and are unity when $Y = T$. Also, $C_\ell^{XY} = C_\ell^{XE}$ for $Y = B$. In the construction of these fields the map beam deconvolution is incorporated, hence the beam factors $e^{-\frac{1}{2}\ell^2\sigma_b^2}$ appearing on both fields.

Given the two filtered fields in Eq. (4.9) and Eq. (4.10), the convergence estimators are then given by

$$\hat{\kappa}_{\boldsymbol{\ell}}^{XY} = -\frac{A_\ell^{XY}}{2}\, i\boldsymbol{\ell}\cdot \int d^2\hat{\mathbf{n}}\, Re\left[\mathbf{G}_{XY}(\hat{\mathbf{n}}) W_Y^*(\hat{\mathbf{n}})\right]\, e^{-i\boldsymbol{\ell}\cdot\hat{\mathbf{n}}}. \tag{4.11}$$

The normalisation coefficients, A_ℓ^{XY}, are related to the noise power spectrum, $N_\ell^{\kappa\kappa,XY}$, of the estimators $\hat{\kappa}^{XY}(\hat{\mathbf{n}})$ by $N_\ell^{\kappa\kappa,XY} = \ell^2 A_\ell^{XY}/4$, and can be expressed as

$$\begin{aligned} \frac{1}{A_\ell^{XY}} &= \frac{1}{\ell^2}\int \frac{d^2\boldsymbol{\ell}_1}{(2\pi)^2}(\boldsymbol{\ell}\cdot\boldsymbol{\ell}_1)\, \frac{C_{\ell_1}^{XY} f_{\boldsymbol{\ell}_1\boldsymbol{\ell}_2}^{XY}}{\tilde{C}_{\ell_1}^{X,obs}\, \tilde{C}_{\ell_2}^{Y,obs}} \\ &\times \left\{ \begin{array}{c} \cos 2\Delta\varphi \\ \sin 2\Delta\varphi \end{array} \right\} e^{-\ell_1^2\sigma_b^2}\, e^{-\ell_2^2\sigma_b^2}, \end{aligned} \tag{4.12}$$

with $\boldsymbol{\ell} = \boldsymbol{\ell}_1 + \boldsymbol{\ell}_2$, $\Delta\varphi = \varphi_{\boldsymbol{\ell}_1} - \varphi_{\boldsymbol{\ell}_2}$, and $\langle X_{\boldsymbol{\ell}_1} Y_{\boldsymbol{\ell}_2}\rangle = f_{\boldsymbol{\ell}_1\boldsymbol{\ell}_2}^{XY}\, \phi_{\boldsymbol{\ell}}$, where [153]

$$\begin{aligned} f_{\boldsymbol{\ell}_1,\boldsymbol{\ell}_2}^{TT} &= (\boldsymbol{\ell}\cdot\boldsymbol{\ell}_1)\, C_{\ell_1}^T + (\boldsymbol{\ell}\cdot\boldsymbol{\ell}_2)\, C_{\ell_2}^T, \\ f_{\boldsymbol{\ell}_1,\boldsymbol{\ell}_2}^{TE} &= (\boldsymbol{\ell}\cdot\boldsymbol{\ell}_1)\, C_{\ell_1}^C \cos 2\Delta\varphi + (\boldsymbol{\ell}\cdot\boldsymbol{\ell}_2)\, C_{\ell_2}^C, \\ f_{\boldsymbol{\ell}_1,\boldsymbol{\ell}_2}^{TB} &= (\boldsymbol{\ell}\cdot\boldsymbol{\ell}_1)\, C_{\ell_1}^C \sin 2\Delta\varphi, \\ f_{\boldsymbol{\ell}_1,\boldsymbol{\ell}_2}^{EE} &= \left[(\boldsymbol{\ell}\cdot\boldsymbol{\ell}_1)\, C_{\ell_1}^E + (\boldsymbol{\ell}\cdot\boldsymbol{\ell}_2)\, C_{\ell_2}^E\right] \cos 2\Delta\varphi, \\ f_{\boldsymbol{\ell}_1,\boldsymbol{\ell}_2}^{EB} &= (\boldsymbol{\ell}\cdot\boldsymbol{\ell}_1)\, C_{\ell_1}^E \sin 2\Delta\varphi. \end{aligned} \tag{4.13}$$

On the basis of the relations above, it should be stressed that a careful estimation of the noise contribution to lensing depends on how accurately the observed spectra are known, as well as how much the exponential representation of the high l cutoff due to instrumental beam in (4.12) is indeed faithful. Our code for estimating the convergence using the quadratic estimator formalism is a direct implementation of the above equations, Eq. (4.6)–(4.13), and was exploited in [136]. In that work,

Experiment	FWHM	σ_{pixT} (μK·arcmin)
PLANCK	7.18'	43.1
PRISM	3.2'	2.43

Table 4.1: PLANCK and PRISM performance specifications. Beam FWHM is given in arcminutes, and the sensitivity for T per pixel in μK·arcmin. The channels used are 143 GHz for PLANCK and 160 GHz for PRISM. The polarisation sensitivity for both E and $B-$modes is $\sqrt{2}\Delta T/T$.

the CMB lensing signal was directly simulated on flat sky. In the present one, we need to project a curved sky onto a flat patch, in order to proceed with the analysis. We exploit a gnomonic projection scheme validating it in the next Section.

In Fig. 4.2 the forecasted noise spectra for the minimum variance estimator in a PLANCK-like case [117] and in a PRISM-like case [134] (for the adopted specifications see Tab. 4.1), computed for the PLANCK 1 year cosmology [13] are shown.

By comparing the amplitude of the noise contribution between the PLANCK and PRISM cases, we can conclude that the precision of the PLANCK experiment, despite being extremely powerful on the already delivered temperature spectrum, does still not allow for a detection with high signal to noise ratio at the large scales targeted in this work, both due to the beam amplitude and to the sensitivity, whereas in the case of a future survey with the PRISM specifications the quality of the measurement will improve significantly, permitting to obtain a highly precise reconstruction also at very small angles. For this reason, in this work we will adopt the PRISM specifications to address the contribution coming from non-linearities.

4.3 The reconstructed lensing signal

Here the results of our lensing extraction are presented and discussed, showing the maps of recovered shear lensing signal, and quantitative comparisons of its power spectrum against the ΛCDM predictions in the interval of angular scales which is made accessible by the present simulation setup. First, let us do a few considerations on the noise spectra in the angular region of interest. It is known that the noise spectra of all the possible combinations TT, TE, TB, EE, EB for the convergence spectrum are relatively flat on large scales, just having a difference in amplitude, but not exhibiting a particular dependence on ℓ (see [120]). As already argued in the previous Sections, we are interested in lensing reconstruction ranging from the arcminute to the degree scale, where the noise spectrum is comparable or lower than the signal to extract only for the TT and EB cases. Thus, the focus of the analysis is on the latter two observables as they are most significant for the experimental configurations examined.

We apply the flat sky lensing estimator procedure described in Sec. 4.1 by adopting a 15° patch side. The lensing extraction pipeline proceeds as follows. From the all sky lensed maps, we extract 296 squared patches, with centres dis-

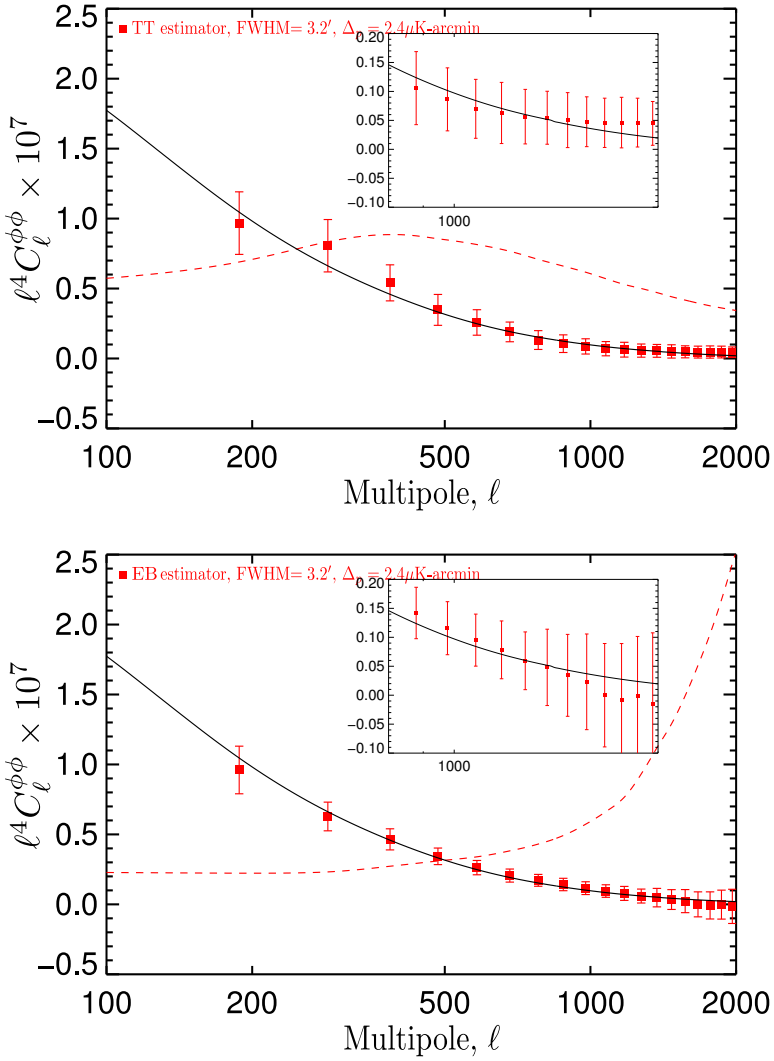

Figure 4.3: Convergence spectrum extraction from LP simulated maps using the TT (top) and EB estimator (bottom), side of patch side of 15° for the PRISM specifications. The error bars are estimated as the variance of the 296 patches. The dashed lines represent the noise contribution as evaluated by the estimator, which has been subtracted from the recovered signal in order to obtain the data points. The black line is the convergence spectrum obtained by CAMB for the reference cosmology, the red dashed lines represent the noise contribution.

tributed following [157]. The shear angular power spectra from each single patch are then stacked for producing the final result. The noise contribution as predicted by the lensing estimator is subtracted. In order to validate our simulation setup, we perform a test run using a simulated LP map by adopting the PRISM specifications and a WMAP 1 year fiducial set of cosmological parameters [148]. The resulting convergence spectra as output by the lensing extraction pipeline and obtained by subtracting the noise contribution are shown in Fig. 4.3 and exhibit a complete agreement with the theoretical prediction both for the TT and the EB case. The zoomed regions in the $800 \leq \ell \leq 2000$ exhibit numerical instabilities which are

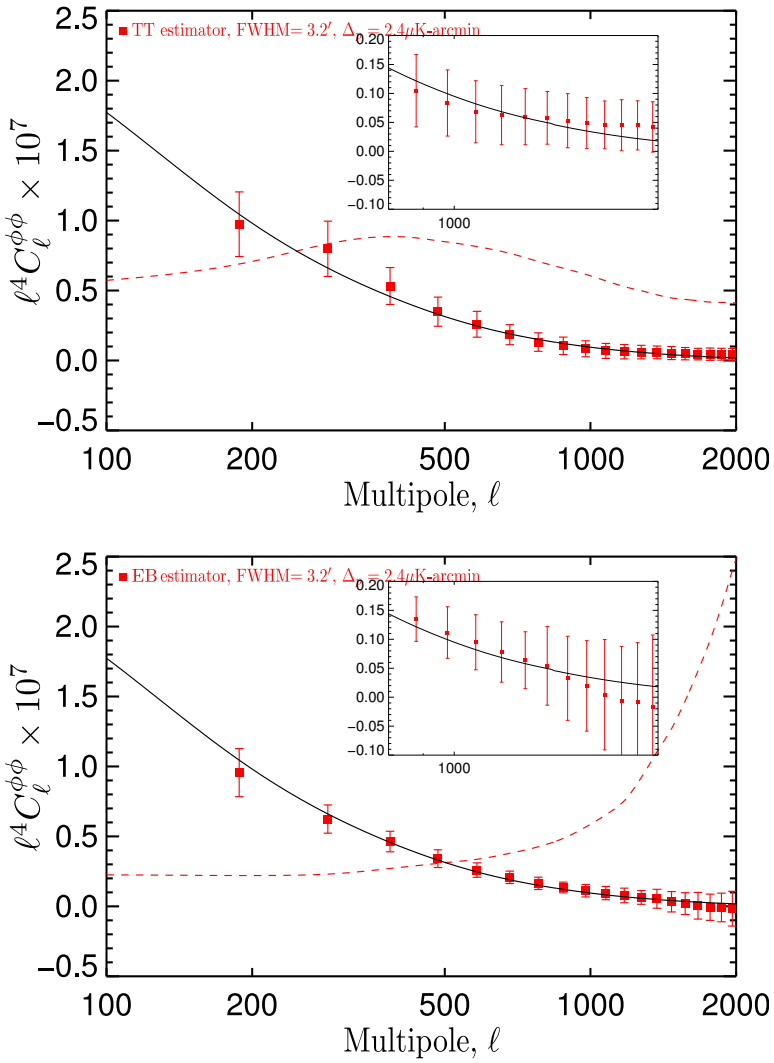

Figure 4.4: Convergence spectrum extraction from N-body lensed maps using the TT (top) and EB estimator (bottom). Notation and line style associations are the same as in Fig. 4.3.

showing up at the highest multipoles. The figure also anticipates some of the features which will be highlighted for the cases of the run on the N-body CMB lensed maps, precisely in the shape and amplitude of the noise contributions, for the TT and EB cases. The TT case appears to be noise dominated on all angular scales, while the effects of the limited angular resolution are visible at the largest scales in the EB signal, in the shape of the noise contribution, reflected by the error bar increase in the recovered signal at $\ell \gtrsim 1500$. The ΛCDM predicted power is recovered very accurately on all scales, reflecting the precision in the evaluation of the noise contribution. Finally, with the adopted specifications, the polarised data do represent a significant contribution to the recovery of the signal, with comparable precision up to $\ell \simeq 1500$. It is also interesting to look at the reconstruction precision, reaching a few percent in bins with $\Delta\ell \simeq 100$ in the angular multipole

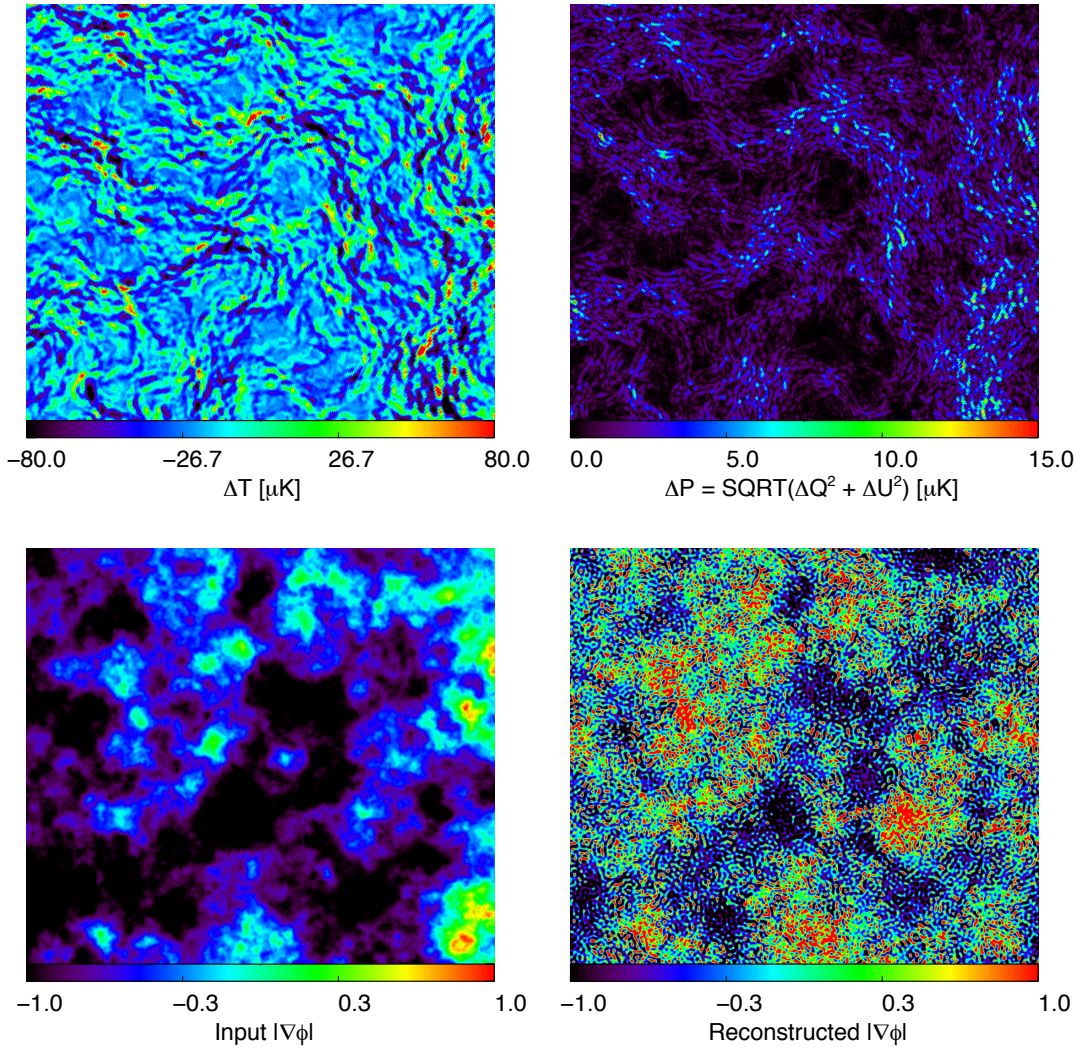

Figure 4.5: Lensed and unlensed difference maps in the temperature (top right panel) and polarised intensity fields (top left panel) in the same patch of the CMB maps compared with the modulus of the input (bottom right panel) and reconstructed (bottom left panel) deflection angle.

interval $1000 \lesssim \ell \lesssim 2000$ for T, and about 10% for EB.

Let us now turn to the study of results on the N-body lensed CMB maps. The angular power spectra from the shear maps stacking are shown in Fig. 4.4, where the two panels corresponding to the result of the TT (top) and EB (bottom) estimators, respectively, show the reconstructed lensing potential evaluated by stacking the lensing spectra extracted in each of the regions considered. As expected, the noise contributions for the two cases are the same as the LP case in Fig. 4.3. The solid lines corresponding to the the spectra after subtraction of the noise contribution show no visible departure from predictions of the weak lensing power as predicted by the ΛCDM cosmology, within uncertainties, for both cases, in particular

on the angular scales which are less affected by cosmic variance, e.g. corresponding to $\ell \simeq 1000$ and beyond.

The consistency between the two cases keeps validity up to the extreme angular resolution, as it is clear by comparing the zoomed areas in Figs.4.3 and 4.4 cases, indicating that the behaviour at the largest scales is actually a numerical feature to be attributed to the estimator rather than to the simulated CMB lensing maps. It is to be noted that the results in Fig. 4.4 are obtained from the MS-modified-LP as defined in Sec. 4.1, whereas the panels shown in 4.3 have been obtained with the standard unmodified LP version. This result, validating the whole scheme of the simulation pipeline, constructed using N-body structures out of theoretical power predicted semi-analytically, ray-traced and then inspected at the level of the CMB lensing extraction precision, has the immediate consequence that the biases from inaccuracies across the pipeline are well below the high precision performance of next generation CMB experiments for lensing extraction.

The outlined procedure should then allow to characterise departures from ΛCDM predictions within the redshift interval which is contributing significantly to the lensing power, within the assumed instrumental accuracy. It should be noted that this is true in particular in the small scale part, where the corrections from mildly non-linear matter evolution, described through the `Halofit`[4] package into `CAMB`, contribute and are faithfully reconstructed.

Before concluding we perform a last visual study of our results, showing how the lensing signal is consistent in different renderings. In Fig. 4.5 the four panels show the modulus of the input and reconstructed deflection angle compared with the difference between the lensed and unlensed CMB maps for T and the polarisation amplitude $P = \sqrt{Q^2 + U^2}$. A first immediate evidence is the marked non-Gaussianity of the lensing field, e.g. in the T difference; the structures there represent the line of sight integral of MS DM lenses acting on the background CMB field. The same holds for the polarisation field difference, with a clear correlation with the T field, as expected, as well as a finer structure in the lensing contribution.

The bottom panels show the input and reconstructed noisy lensing potential field, again featuring an evident correlation between input and output, despite of the noise pattern, which is also well evident. A similar analysis, on the whole sky, was performed by [144], without applying a full lensing extraction pipeline as we do in the present work.

Before closing this Chapter, the beginning of the exploitation of the results obtained so far is presented. The successful recovery of the CMB lensing pattern on all the relevant angular scales for the adopted simulations allows us to investigate its behaviour and constraining power in cosmologies which are modified with respect to the concordance ΛCDM model. Here, the case of the presence in the Universe of massive neutrinos is considered.

[4] `http://www.roe.ac.uk/~jap/haloes/`

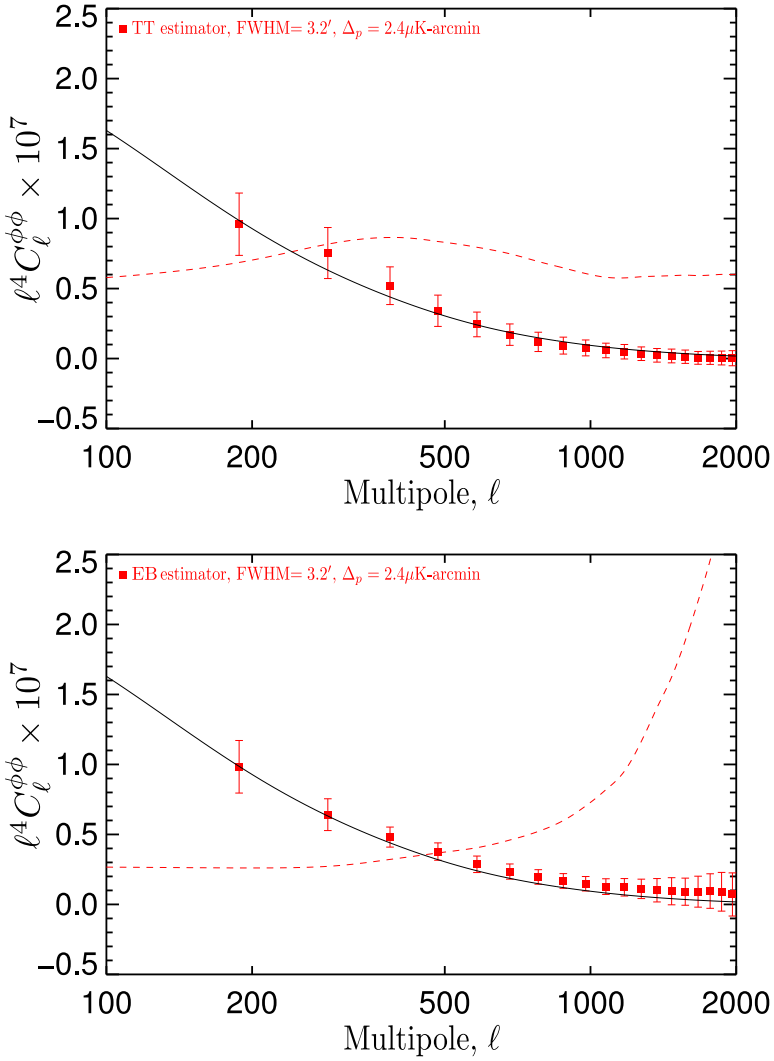

Figure 4.6: Convergence spectrum extraction from N-body lensed DEMNUNI map with a ΛCDM cosmology, using the TT (top) and EB estimator (bottom).

4.4 CMB lensing extraction from DEMNUni maps

In this Section the results of the application of the pipeline described in Sec. 4.2 on CMB maps obtained by lensing the unperturbed fields through the DEMNUNI (Dark Energy, Massive NEutrino Universe) simulations with massive neutrinos are presented.

As it was argued in subsec. 2.2.3, once the background cosmology is fixed (and particularly the initial amplitude of perturbations A_s), the effect of neutrinos is to suppress the growth of structures below the free streaming length, damping significantly the matter power spectrum. Linear predictions overestimate significantly this observable (look again at Fig. 2.8); for this reason, it is most important to address simulations which include the influence of structure formation from

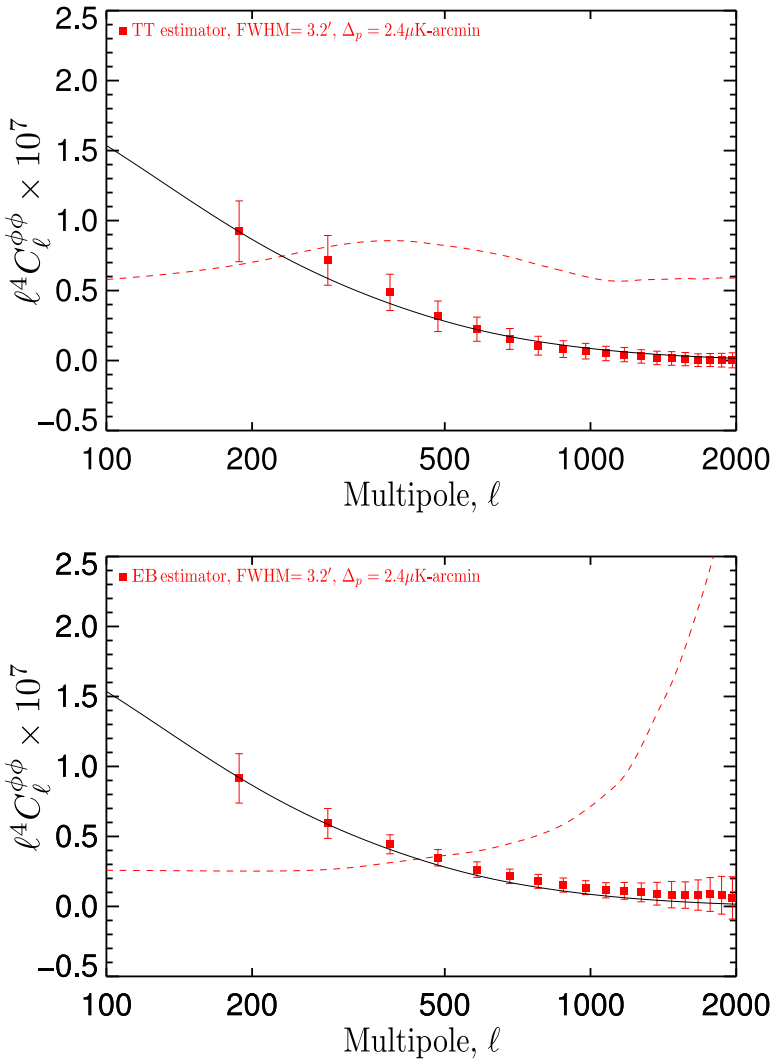

Figure 4.7: Convergence spectrum extraction from N-body lensed DEMNUNI map with $\sum m_\nu = 0.17$ eV on a ΛCDM background using the TT (top) and EB estimator (bottom). Notation and line style associations are the same as in Fig. 4.3.

different species in such a way to achieve a full understanding not only of the formation of structures itself, but subsequently, also of all the observables involving the interplay of structure formation during cosmic time.

For this reason, the same method outlined in this Chapter is currently being applied to the DEMNUNI set of simulations [158, 159, 160], which is a group of high resolution N-body simulations with a reference cosmology compatible with PLANCK 1 year results [13], created using the GADGET-3[5] code which includes CDM and neutrino particles [101]. It uses about 2048^3 DM particles with mass $8.6 \times 10^8 h^{-1} M_\odot$, and 2048^3 neutrino particles (in this case the mass depends on the value $\sum m_\nu$) in a cubic region of $2h^{-1}$ Gpc side which evolves from redshift $z_* =$

[5] http://www.mpa-garching.mpg.de/gadget/

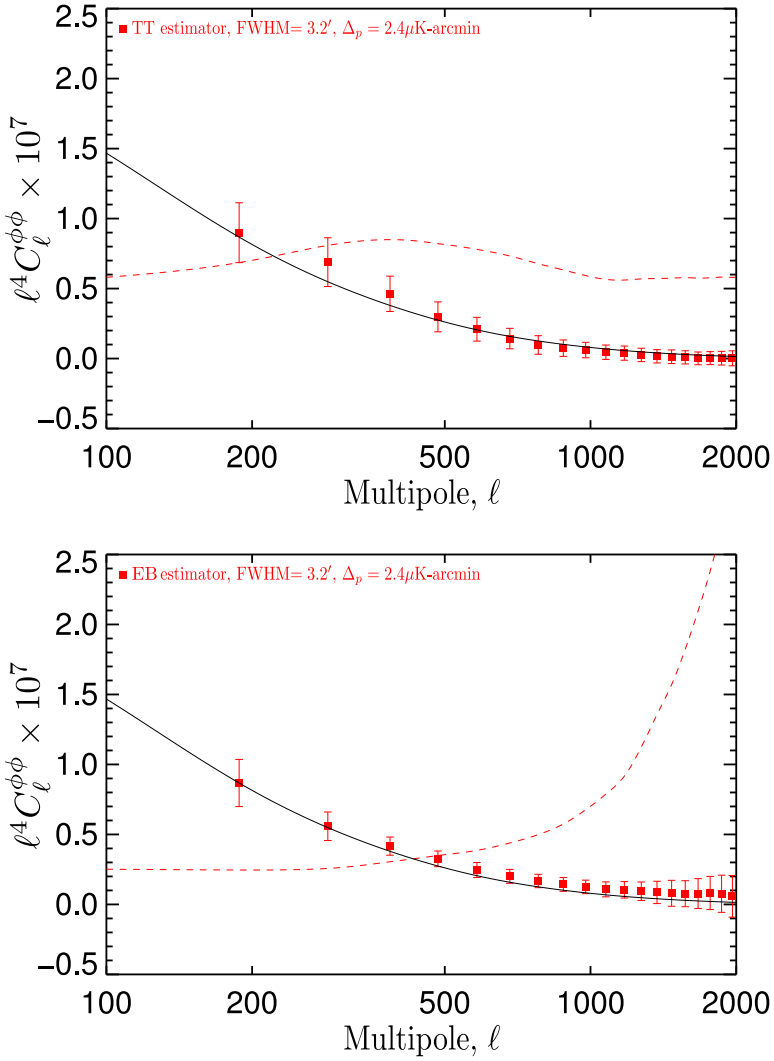

Figure 4.8: Convergence spectrum extraction from N-body lensed DEMNUNI map with $\sum m_\nu = 0.3$ eV on a ΛCDM background using the TT (top) and EB estimator (bottom). Notation and line style associations are the same as in Fig. 4.3.

99 to the present, with periodic boundary conditions. The considered cosmologies are a standard ΛCDM case, and three cases with $\sum m_\nu = 0.17$ eV, 0.3 eV, 0.53 eV respectively. The neutrinos are treated as a separate collisionless fluid, just like the DM; in this case no baryons are considered, so the hydrodynamics is not included.

All the above characteristics make sure that the formation of structures is taken into account faithfully in the N-body realisation; the same map making procedure explained in Sec. 4.1 (the only difference being that, as the simulation box is bigger, the LS-adding only takes place for $\ell < 30$, and the dimension of the shell is $2h^{-1}$ Gpc side), as well as the algorithm of CMB lensing extraction described in Sec. 4.2 are adopted in order to create CMB maps lensed by this set of simulations, and to extract and characterise the resulting convergence power spectrum. The PRISM

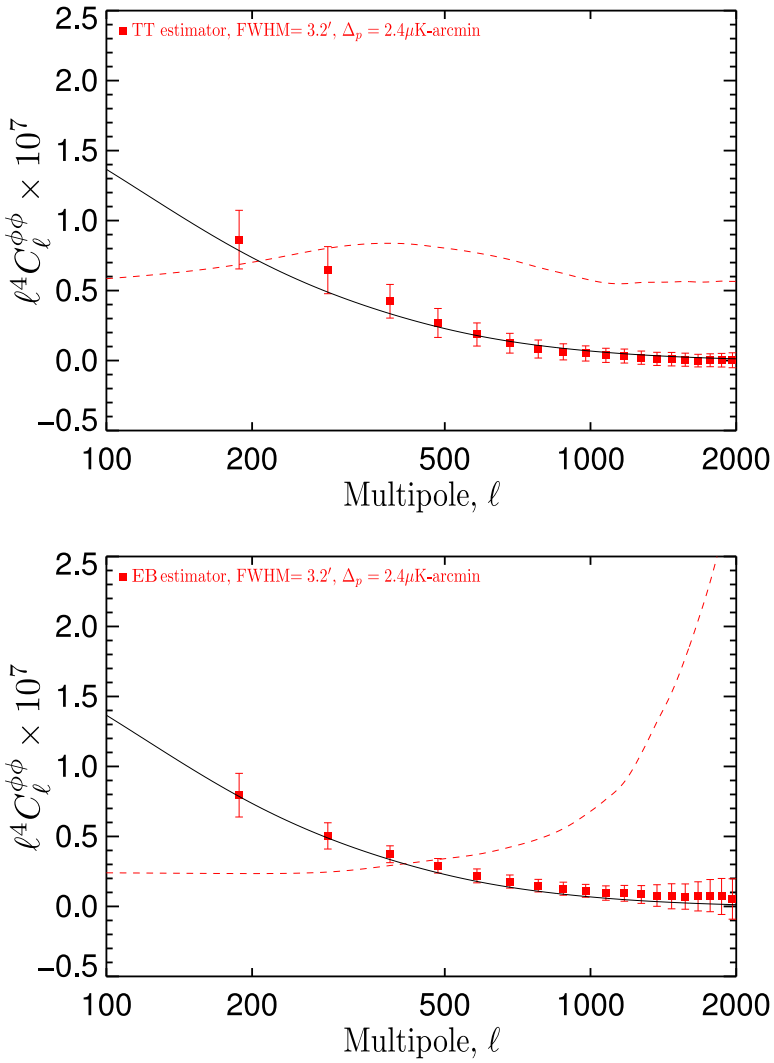

Figure 4.9: Convergence spectrum extraction from N-body lensed DEMNUNI map with $\sum m_\nu = 0.53$ eV on a ΛCDM background cosmology, using the TT (top) and EB estimator (bottom). Notation and line style associations are the same as in Fig. 4.3.

specifications in Table 4.1 are used again.

Let us now examine the results from the extraction of the lensing signal showing the maps of recovered shear lensing signal, and quantitative comparisons of its power spectrum with the predicted one in the different cases considered. Fig. 4.6, 4.7, 4.8, 4.9 show the extracted convergence spectrum for the considered cosmologies (ΛCDM with no neutrinos, ΛCDM with $\sum m_\nu = 0.17$ eV, 0.3 eV, 0.53 eV) for the TT and EB estimators.

It can be clearly seen how the theoretical and extracted spectra change with the presence of a non-vanishing neutrino mass, which as already underlined causes a damping in the structure formation, ranging from $C_\ell^{kk} \sim 1.6 \times 10^{-7}$ in the case with no neutrinos, to $C_\ell^{kk} \sim 1.45 \times 10^{-7}$ in the case $\sum m_\nu$ =0.53 eV at $\ell \sim 100$;

it is noteworthy to see that the agreement is very good on all the involved scales, in particular in the range $100 \lesssim \ell \lesssim 500$, probing the robustness of the algorithm also in case of deviations from a standard ΛCDM cosmology.

As for the validating runs in Sec. 4.3, also here it is found that any possible bias introduced by the pipeline are below the high precision performance of next generation CMB experiments for lensing extraction. On large multipoles we detect a discrepancy, especially in the case of the *EB* estimator; despite the fact that the signal is being recovered within the error bars (and well below the noise level of the experiment), we are inspecting this effect of overestimation in the DEMNUNI set of maps; a thorough comparison with the small scale power of the original simulations is needed, and will be addressed in a future work aiming at the full characterisation of the studied maps, and at quantifying in detail the constraining power of the deflection spectrum when combined with other cosmological information.

Overall, we deem these results as encouraging, and we plan on applying the pipeline to different N-body simulations, such as the CODECS (Coupled Dark Energy Cosmological Simulations) [28] which simulate non-linear structures in the context of non-standard expansion histories in the period dominated by DE.

4.5 Concluding remarks

We presented here the first extraction of lensing shear and quantitative comparison with semi-analytical expectations of CMB lensing simulations obtained through ray-tracing across N-body structure formation. We consider the lensed total intensity and polarisation CMB maps obtained by displacing the background field with Born approximated deflection angles evaluated from the Millennium Run simulation, stacked to fill up the whole Hubble volume. The pipeline described is tested and validated by making use of simulated realisations of CMB lensing fields where the polarisation angle is assumed to have a Gaussian statistics and a power spectrum as given by semi-analytic predictions.

We adopt the specifications of future high resolution and sensitivity CMB satellites, corresponding to arcminute and μK-arcminute angular resolution and sensitivity, respectively. The geometry of the simulation setup, corresponding to a N-body box size of $500h^{-1}$ Mpc and a pixelisation with $1.7'$ pixel size, gives us access to angular scales covering the arcminute and reaching about a degree in the sky. For that we use a flat sky approximated version of the lensing extraction pipeline based on a quadratic estimator.

The extracted lensing pattern is inspected separately from total intensity and polarisation. We discuss the lensing contribution as predicted by the lensing estimator in the two cases, which turns out to be completely noise dominated for total intensity, while the effect of limited angular resolution is evident in the polarisation noise contribution at the small scale edge of the relevant interval.

By applying the extraction pipeline, the reconstructed weak lensing shear power spectra are found to be featureless as in the case of the simulated maps, follow-

ing the theoretically predicted power within the assumed uncertainties, separately for the total intensity and polarisation based estimator. Within the assumed instrumental specifications, the polarisation field has comparable relevance in constraining the lensing signal.

The proposed method is applied to the DEMNUNI set of cosmological N-body simulations, describing four different cosmologies with different values of the neutrino mass. The results are promising, in particular when considering the outlook that can be obtained by applying the pipeline to simulations with different specifications, or with different choices of the background cosmology. Among our future perspectives in this sense, the next step is to study CMB maps lensed by the CODECS set of coupled DE cosmologies simulated structures. It is interesting to note that, in the studied case, the extracted signal follows closely the variations of the theoretical spectrum, suggesting that the extracted signal might be used as a constraining probe of the neutrino mass.

The performed analysis is relevant in the context of the current and planned CMB and LSS large observational campaigns. In this context, galaxy-galaxy and CMB lensing are predicted to be most important observables for constraining the dark cosmological components, and the control and reliability of the corresponding simulated signal possesses a crucial importance in the forecasting phase, as well as for the interpretation of the data.

For this reason, it is important in particular for CMB lensing to gather the different pieces of the simulations in a single pipeline and to study the results. This work represents a first significant step in this direction, demonstrating not only that the inaccuracies of the simulated cosmological structure, ray-tracing scheme and lensing extraction provide no significant disturbance to the lensing recovery on the entire interval of angular scale considered, but also that this procedure can be upgraded by adopting more sophisticated simulations, both in terms of general architecture of the N-body and/or ray-tracing procedure, as well as underlying cosmologies. These aspects are indeed the subject of our future works in this direction.

Conclusions

The physics of the evolving and expanding Universe is at present well described by the standard ΛCDM model. The current sensitivity of experimental setups is enabling us to address increasingly finer corrections of the initial perturbations power spectra. For the CMB, these are the sources of secondary anisotropy, *i.e.* modifications of the spectra happening during the path of the photons from the last scattering surface to the observer. Among the latter, the deflection enacted by the interaction of photons with the gravitational potential arising from matter structures in the Universe, CMB lensing, is gathering more and more attention; after its first detection in the high multipoles of the temperature data by various collaborations, its constraining power is starting to increase our knowledge of the fundamental parameters describing the energy content and expansion history of the Universe.

In this regard, in the next years a number of datasets relevant for the full characterisation of this effect are going to be released by various collaborations. In the next months, PLANCK second data release, including polarisation data, is going to be published; a number of suborbital experiments (SPT, ACT, POLARBEAR, BICEP2, EBEX...) are taking data, or planning extensions of the observational time. In the upcoming years, this continuous flow of data is going to foster a growing attention of the community on the potential of this observable and the implications that a precise measurement of the lensing power spectrum from CMB can reflect on our knowledge about cosmology and astrophysics.

Among the next generation endeavours for observing the sky, a crucial role will be played by the EUCLID satellite, which will deliver a catalogue of billions of objects in a range $0.5 \lesssim z \lesssim 2$, along with imaging and spectroscopic data. Mapping the recent Universe on a large volume and with such a sensitivity will allow to constrain the recent expansion history, as well as possible deviations from General Relativity.

In this regard, it should be noted that constraints on the cosmological parameters can be improved not only by considering CMB lensing as a separate observable, but also by taking into account the cross-correlation between CMB lensing and galaxy angular distributions. This process enhances the contribution given to the unperturbed CMB by the gravitational potential by relating it to the structures enacting the deflection itself. Furthermore, cross-correlating different datasets allows to identify and gain control on the different systematics, peculiar to each ex-

periment, and lower their bias on the final results. This aspect becomes even more important when considering the fact that cosmological and astrophysical datasets are now increasingly dominated by systematic, rather that statistical uncertianties.

For addressing this topic, there is a need for improving the current capabilities of understanding of the signal, in particular concerning the simulation machinery: the more experimental specifications are improved, the more second order, and non-linear effects come into play. A comprehension of the observables currently in use, and the definition of new ones, is necessary down to the smallest angular scales, demanding for more accurate, detailed simulations accounting for many different physical effects.

In this work, the physics of CMB lensing was addressed and exploited in order to increase our knowledge about the interplay of this observable with the inflationary signal of primordial origin. Considering jointly the presence of both signals in the $B-$modes of CMB datasets allows to exploit wisely all the encoded information resulting in a simultaneous constraint of different physical phenomena, in particular in view of forthcoming sub-orbital observations at high resolution. A deep understanding of all the phenomena in play is essential for establishing correct results; this also represents a further indication that a further step is needed in the current way of developing simulations. As the process of data analysis digs deeper in data, new degenerations can arise, which may challenge our assumptions; and this can only be taken into account with an increasing precision on jointly considering the taking place of multiple effects at all scales.

As a step towards this direction, a method for characterising CMB lensed maps raytraced through the lensing potential of N-body simulations in a range $100 \lesssim \ell \lesssim 2000$ was here presented. This approach allows to have full control of the underlying physics, in order to check for deviations from the standard ΛCDM case, as well as to address the non-linear clustering which kicks in at small scales in the sky. The pipeline was validated on CMB maps lensed by structures created via stacking the MS, showing a good agreement of the results with the predictions. This shows that the method is ready for exploitation on more sophisticated cases, and that the hunt for the influence of non-linearities pushes towards even smaller scales, facing us with new computational challenges.

The full exploitation of this method is already taking place: the possible applications are variegate, ranging from modified gravity, non-standard DE evolution histories, the only limit being the choice of the cosmological model to simulate, and hence the computational time invested in the realisation of the N-body boxes. We presented here a first application to the DEMNUNI set of N-body simulations considering a non-zero mass of neutrinos. The ultimate aim of this approach is to quantify the accuracy of simulations with respect to semianalytic approaches, and to understand the lensing signal in relation to open issues of contemporary cosmology, and of physics in general.

The work described here is an ongoing process, and just a number of all the possible applications have been hypothesised up to now. Possible extensions to be considered for the near future are the full characterisation of maps with non-trivial neutrino content and their exploitation to forecast a constraint on the neutrino

mass, as a completion of the ongoing work; the application of the method to the CoDECS set of N-body realisations of non-standard DE histories; the extension of the algorithm to a faithful reconstruction of the large angular scales; and the analysis of maps produced with more sophisticated ray-tracing machineries, going beyond the Born approximation [161].

The next step is start the study of the cross-correlation signal between the CMB maps with the structures that enact the distortion along the path of photons. It is to remark that the CMB N-body lensing setup is particularly suitable for studying the capabilities of cross-correlations. A first step would imply the creation of "tomographic" redshift shells of lenses, followed by the generation of mock catalogues in order to simulate observations and associated errors. Observations are progressing quite fast for cross-correlation studies, see e.g. [162].

It is certainly crucial to complement these findings with appropriate simulations, in order to understand the associated constraining capabilities in given instrumental setups. This topic will become increasingly interesting in view of the analysis of the EUCLID dataset: to exploit at its full potential all the cosmological information potentially contained in the combination PLANCK + EUCLID dedicated algorithms and pipelines will be developed; in the specific case of CMB lensing, the preparatory work could involve the cross-correlation of the lensing signal with the shells of structures generated in the map-making procedure or with halo catalogues of the simulations itself, as well as a complete study of the systematics involved in the two instruments.

List of Figures

List of Tables

Bibliography

[1] C. Antolini, M. Martinelli, Y. Fantaye, and C. Baccigalupi. Measuring primordial gravitational waves from CMB $B-$modes in cosmologies with generalized expansion histories. *J. Cosm. Astroparticle Phys.*, 2:24, February 2013. (Cit. on p. 1, 8, 29, and 63)

[2] C. Antolini, Y. Fantaye, M. Martinelli, C. Carbone, and C. Baccigalupi. N-body lensed CMB maps: lensing extraction and characterization. *J. Cosm. Astroparticle Phys.*, 2:39, February 2014. (Cit. on p. 1, 8, and 82)

[3] The ACT Collaboration. Detection of the Power Spectrum of Cosmic Microwave Background Lensing by the Atacama Cosmology Telescope. *Physical Review Letters*, 107(2):021301, July 2011. (Cit. on p. 7, 30, 32, and 105)

[4] The SPT Collaboration. A Measurement of the Damping Tail of the Cosmic Microwave Background Power Spectrum with the South Pole Telescope. *Astrophys. J.*, 743:28, December 2011. (Cit. on p. 7, 30, 33, and 105)

[5] The PLANCK Collaboration. PLANCK 2013 results. XVII. Gravitational lensing by large-scale structure. *ArXiv e-prints*, March 2013. (Cit. on p. 7, 30, 31, 32, 62, and 105)

[6] The SPT Collaboration. Detection of $B-$Mode Polarization in the Cosmic Microwave Background with Data from the South Pole Telescope. *Physical Review Letters*, 111(14):141301, October 2013. (Cit. on p. 7, 33, and 105)

[7] The POLARBEAR Collaboration. A Measurement of the Cosmic Microwave Background $B-$Mode Polarization Power Spectrum at Sub-Degree Scales with POLARBEAR. *ArXiv e-prints*, March 2014. (Cit. on p. 7, 30, 34, and 105)

[8] W. Hu, D. Huterer, and K. M. Smith. Supernovae, the Lensed Cosmic Microwave Background, and Dark Energy. *Astrophys. J. Lett.*, 650:L13–L16, October 2006. (Cit. on p. 7, 62, and 70)

[9] V. Acquaviva and C. Baccigalupi. Dark energy records in lensed cosmic microwave background. *Phys. Rev. D*, 74(10):103510, November 2006. (Cit. on p. 7, 46, 47, 62, 65, 66, and 106)

[10] The ACT Collaboration. Evidence for Dark Energy from the Cosmic Microwave Background Alone Using the Atacama Cosmology Telescope Lensing Measurements. *Physical Review Letters*, 107(2):021302, July 2011. (Cit. on p. 7, 32, 33, 62, and 105)

[11] The EUCLID Collaboration. EUCLID Definition Study Report. *ArXiv e-prints*, October 2011. (Cit. on p. 7, 37, and 41)

[12] J. Lesgourgues and S. Pastor. Massive neutrinos and cosmology. *Phys. Rept.*, 429:307–379, July 2006. (Cit. on p. 8 and 55)

[13] The PLANCK Collaboration. PLANCK 2013 results. XVI. Cosmological parameters. *ArXiv e-prints*, March 2013. (Cit. on p. 8, 15, 31, 37, 41, 58, 59, 89, and 95)

[14] J. Lesgourgues, L. Perotto, S. Pastor, and M. Piat. Probing neutrino masses with CMB lensing extraction. *Phys. Rev. D*, 73(4):045021, February 2006. (Cit. on p. 8, 58, and 59)

[15] The KATRIN Collaboration. KATRIN: A next generation tritium beta decay experiment with sub-eV sensitivity for the electron neutrino mass. *ArXiv High Energy Physics - Experiment e-prints*, September 2001. (Cit. on p. 8 and 54)

[16] M. Zaldarriaga and U. Seljak. All-sky analysis of polarization in the microwave background. *Phys. Rev. D*, 55:1830–1840, February 1997. (Cit. on p. 13 and 61)

[17] M. Kamionkowski, A. Kosowsky, and A. Stebbins. Statistics of cosmic microwave background polarization. *Phys. Rev. D*, 55:7368–7388, June 1997. (Cit. on p. 13 and 61)

[18] The PLANCK Collaboration. PLANCK 2013 Results. XXIV. Constraints on primordial non-Gaussianity. *ArXiv e-prints*, March 2013. (Cit. on p. 14)

[19] The COBE Collaboration. Structure in the COBE differential microwave radiometer first-year maps. *Astrophys. J. Lett.*, 396:L1–L5, September 1992. (Cit. on p. 15)

[20] A. Challinor and H. Peiris. Lecture notes on the physics of cosmic microwave background anisotropies. In M. Novello and S. Perez, editors, *American Institute of Physics Conference Series*, volume 1132 of *American Institute of Physics Conference Series*, pages 86–140, May 2009. (Cit. on p. 16, 17, and 104)

[21] S. Dodelson. *Modern cosmology*. 2003. (Cit. on p. 16, 44, and 55)

[22] M. Zaldarriaga. Polarization of the microwave background in reionized models. *Phys. Rev. D*, 55:1822–1829, February 1997. (Cit. on p. 18)

[23] R. Narayan and M. Bartelmann. Lectures on Gravitational Lensing. *ArXiv Astrophysics e-prints*, June 1996. (Cit. on p. 20, 23, and 104)

[24] P. Schneider, J. Ehlers, and E. E. Falco. *Gravitational Lenses*. 1992. (Cit. on p. 20)

[25] M. Bartelmann and P. Schneider. Weak gravitational lensing. *Phys. Rept.*, 340:291–472, January 2001. (Cit. on p. 21, 47, 65, 83, and 104)

[26] A. Lewis and A. Challinor. Weak gravitational lensing of the CMB. *Phys. Rept.*, 429:1–65, June 2006. (Cit. on p. 24, 25, 26, 27, 29, 83, 84, 86, and 104)

[27] C. Carbone, V. Springel, C. Baccigalupi, M. Bartelmann, and S. Matarrese. Full-sky maps for gravitational lensing of the cosmic microwave background. *MNRAS*, 388:1618–1626, August 2008. (Cit. on p. 25, 82, 84, 85, and 108)

[28] C. Carbone, M. Baldi, V. Pettorino, and C. Baccigalupi. Maps of CMB lensing deflection from N-body simulations in Coupled Dark Energy Cosmologies. *J. Cosm. Astroparticle Phys.*, 9:4, September 2013. (Cit. on p. 25, 82, and 98)

[29] R. E. Smith, J. A. Peacock, A. Jenkins, S. D. M. White, C. S. Frenk, F. R. Pearce, P. A. Thomas, G. Efstathiou, and H. M. P. Couchman. Stable clustering, the halo model and non-linear cosmological power spectra. *MNRAS*, 341:1311–1332, June 2003. (Cit. on p. 26)

[30] W. Hu. Weak lensing of the CMB: A harmonic approach. *Phys. Rev. D*, 62(4):043007, August 2000. (Cit. on p. 26, 28, 65, 83, and 86)

[31] A. Challinor and G. Chon. Geometry of weak lensing of CMB polarization. *Phys. Rev. D*, 66(12):127301, December 2002. (Cit. on p. 26, 28, and 83)

[32] E. V. Linder. Correlated gravitational lensing of the CMB. *ArXiv Astrophysics e-prints*, June 1996. (Cit. on p. 27)

[33] W. Hu. Dark synergy: Gravitational lensing and the CMB. *Phys. Rev. D*, 65(2):023003, January 2002. (Cit. on p. 29)

[34] U. Seljak and C. M. Hirata. Gravitational lensing as a contaminant of the gravity wave signal in the CMB. *Phys. Rev. D*, 69(4):043005, February 2004. (Cit. on p. 29, 62, 66, and 79)

[35] A. Blanchard and J. Schneider. Gravitational lensing effect on the fluctuations of the cosmic background radiation. *Astron. & Astrophys.*, 184:1–6, October 1987. (Cit. on p. 29)

[36] K. M. Smith. Pseudo-C_ℓ estimators which do not mix E and B modes. *Phys. Rev. D*, 74(8):083002, October 2006. (Cit. on p. 29)

[37] C. M. Hirata, S. Ho, N. Padmanabhan, U. Seljak, and N. A. Bahcall. Correlation of CMB with large-scale structure. II. Weak lensing. *Phys. Rev. D*, 78(4):043520, August 2008. (Cit. on p. 29)

[38] The ACBAR Collaboration. High-Resolution CMB Power Spectrum from the Complete ACBAR Data Set. *Astrophys. J.*, 694:1200–1219, April 2009. (Cit. on p. 30)

[39] The POLARBEAR Collaboration. Evidence for Gravitational Lensing of the Cosmic Microwave Background Polarization from Cross-Correlation with the Cosmic Infrared Background. *Physical Review Letters*, 112(13):131302, April 2014. (Cit. on p. 30, 34, 35, and 105)

[40] The PLANCK Collaboration. PLANCK 2013 results. XV. CMB power spectra and likelihood. *ArXiv e-prints*, March 2013. (Cit. on p. 30 and 105)

[41] The PLANCK Collaboration. PLANCK early results. I. The Planck mission. *Astron. & Astrophys.*, 536:A1, December 2011. (Cit. on p. 30 and 68)

[42] A. Kosowsky. The Atacama Cosmology Telescope. *New Astron. Rev.*, 47:939–943, December 2003. (Cit. on p. 32)

[43] K. M. Smith and M. Zaldarriaga. General solution to the $E - B$ mixing problem. *Phys. Rev. D*, 76(4):043001, August 2007. (Cit. on p. 33 and 105)

[44] The SPT Collaboration. The 10 Meter South Pole Telescope. *Publications of the ASP*, 123:568–581, May 2011. (Cit. on p. 33)

[45] The SPT Collaboration. A Measurement of Gravitational Lensing of the Microwave Background Using South Pole Telescope Data. *Astrophys. J.*, 756:142, September 2012. (Cit. on p. 33 and 70)

[46] The SPT Collaboration. Measurements of Secondary Cosmic Microwave Background Anisotropies with the South Pole Telescope. *Astrophys. J.*, 719:1045–1066, August 2010. (Cit. on p. 33)

[47] The SPT Collaboration. A Measurement of the Cosmic Microwave Background Damping Tail from the 2500-Square-Degree SPT -SZ Survey. *Astrophys. J.*, 779:86, December 2013. (Cit. on p. 33)

[48] The SPT Collaboration. A Cosmic Microwave Background Lensing Mass Map and Its Correlation with the Cosmic Infrared Background. *Astrophys. J. Lett.*, 771:L16, July 2013. (Cit. on p. 33)

[49] The POLARBEAR Collaboration. The POLARBEAR experiment. In *Society of Photo-Optical Instrumentation Engineers (SPIE) Conference Series*, volume 8452 of *Society of Photo-Optical Instrumentation Engineers (SPIE) Conference Series*, September 2012. (Cit. on p. 34)

[50] The HERSCHEL Collaboration. The first release of data from the HERSCHEL ATLAS: the SPIRE images. *MNRAS*, 415:911–917, July 2011. (Cit. on p. 35)

[51] A. G. Riess, A. V. Filippenko, P. Challis, A. Clocchiatti, A. Diercks, P. M. Garnavich, R. L. Gilliland, C. J. Hogan, S. Jha, R. P. Kirshner, B. Leibundgut, M. M. Phillips, D. Reiss, B. P. Schmidt, R. A. Schommer, R. C. Smith, J. Spyromilio, C. Stubbs, N. B. Suntzeff, and J. Tonry. Observational Evidence from Supernovae for an Accelerating Universe and a Cosmological Constant. (Cit. on p. 37)

[52] S. Perlmutter, G. Aldering, G. Goldhaber, R. A. Knop, P. Nugent, P. G. Castro, S. Deustua, S. Fabbro, A. Goobar, D. E. Groom, I. M. Hook, A. G. Kim, M. Y. Kim, J. C. Lee, N. J. Nunes, R. Pain, C. R. Pennypacker, R. Quimby, C. Lidman, R. S. Ellis, M. Irwin, R. G. McMahon, P. Ruiz-Lapuente, N. Walton, B. Schaefer, B. J. Boyle, A. V. Filippenko, T. Matheson, A. S. Fruchter, N. Panagia, H. J. M. Newberg, W. J. Couch, and T. S. C. Project. Measurements of Ω and Λ from 42 High-Redshift Supernovae. *Astrophys. J.*, 517:565–586, June 1999. (Cit. on p. 37 and 42)

[53] `https://www.sdss3.org/future/eboss.php`. (Cit. on p. 38)

[54] The DESI collaboration. The DESI Experiment, a whitepaper for Snowmass 2013. *ArXiv e-prints*, August 2013. (Cit. on p. 38)

[55] The SDSS Collaboration. Baryon acoustic oscillations in the Sloan Digital Sky Survey Data Release 7 galaxy sample. *MNRAS*, 401:2148–2168, February 2010. (Cit. on p. 38 and 69)

[56] S. M. Carroll. *Spacetime and geometry. An introduction to general relativity*. 2004. (Cit. on p. 40 and 106)

[57] L. Amendola. Coupled quintessence. *Phys. Rev. D*, 62(4):043511, August 2000. (Cit. on p. 40)

[58] F. Perrotta, C. Baccigalupi, and S. Matarrese. Extended quintessence. *Phys. Rev. D*, 61(2):023507, January 2000. (Cit. on p. 40)

[59] V. Pettorino and C. Baccigalupi. Coupled and extended quintessence: Theoretical differences and structure formation. *Phys. Rev. D*, 77(10):103003, May 2008. (Cit. on p. 40)

[60] M. Chevallier and D. Polarski. Accelerating Universes with Scaling Dark Matter. *International Journal of Modern Physics D*, 10:213–223, 2001. (Cit. on p. 40 and 64)

[61] E. V. Linder. Mapping the Dark Energy Equation of State. *ArXiv Astrophysics e-prints*, November 2003. (Cit. on p. 40 and 64)

[62] V. Pettorino. Testing modified gravity with PLANCK: The case of coupled dark energy. *Phys. Rev. D*, 88(6):063519, September 2013. (Cit. on p. 41)

[63] L. Amendola, S. Appleby, D. Bacon, T. Baker, M. Baldi, N. Bartolo, A. Blanchard, C. Bonvin, S. Borgani, E. Branchini, C. Burrage, S. Camera, C. Carbone, L. Casarini, M. Cropper, C. de Rham, C. Di Porto, A. Ealet, P. G. Ferreira, F. Finelli, J. García-Bellido, T. Giannantonio, L. Guzzo, A. Heavens, L. Heisenberg, C. Heymans, H. Hoekstra, L. Hollenstein, R. Holmes, O. Horst, K. Jahnke, T. D. Kitching, T. Koivisto, M. Kunz, G. La Vacca, M. March, E. Majerotto, K. Markovic, D. Marsh, F. Marulli, R. Massey, Y. Mellier, D. F. Mota, N. Nunes, W. Percival, V. Pettorino, C. Porciani, C. Quercellini, J. Read, M. Rinaldi, D. Sapone, R. Scaramella, C. Skordis, F. Simpson, A. Taylor, S. Thomas, R. Trotta, L. Verde, F. Vernizzi, A. Vollmer, Y. Wang, J. Weller, and T. Zlosnik. Cosmology and Fundamental Physics with the EUCLID Satellite. *Living Reviews in Relativity*, 16:6, September 2013. (Cit. on p. 41)

[64] R. Jimenez, P. Thejll, U. G. Jorgensen, J. MacDonald, and B. Pagel. Ages of globular clusters: a new approach. *MNRAS*, 282:926–942, October 1996. (Cit. on p. 42)

[65] The SNLS Collaboration. Supernova Constraints and Systematic Uncertainties from the First Three Years of the Supernova Legacy Survey. *Astrophys. J. Supp.*, 192:1, January 2011. (Cit. on p. 43 and 106)

[66] M. M. Phillips. The absolute magnitudes of Type IA supernovae. *Astrophys. J. Lett.*, 413:L105–L108, August 1993. (Cit. on p. 43)

[67] C. H. Lineweaver and C. A. Egan. The Cosmic Coincidence as a Temporal Selection Effect Produced by the Age Distribution of Terrestrial Planets in the Universe. *Astrophys. J.*, 671:853–860, December 2007. (Cit. on p. 45 and 106)

[68] N. Straumann. On the Cosmological Constant Problems and the Astronomical Evidence for a Homogeneous Energy Density with Negative Pressure. In B. Duplantier and V. Rivasseau, editors, *Vacuum Energy - Renormalization*, page 7, 2003. (Cit. on p. 45)

[69] R. de Putter, O. Zahn, and E. V. Linder. CMB lensing constraints on neutrinos and dark energy. *Phys. Rev. D*, 79(6):065033, March 2009. (Cit. on p. 47)

[70] M. Doran, G. Robbers, and C. Wetterich. Impact of three years of data from the Wilkinson Microwave Anisotropy Probe on cosmological models with dynamical dark energy. *Phys. Rev. D*, 75(2):023003, January 2007. (Cit. on p. 47)

[71] S. Das and E. V. Linder. CMB polarization impact on cosmological constraints. *Phys. Rev. D*, 86(6):063520, September 2012. (Cit. on p. 47)

[72] O. Zahn and M. Zaldarriaga. Lensing Reconstruction Using Redshifted 21 Centimeter Fluctuations. *Astrophys. J.*, 653:922–935, December 2006. (Cit. on p. 47)

[73] J. R. Pritchard and E. Pierpaoli. Constraining massive neutrinos using cosmological 21cm observations. *Phys. Rev. D*, 78(6):065009, September 2008. (Cit. on p. 47)

[74] J. Beringer for the Particle Data Group. Review of particle physics. *Phys. Rev. D*, 86:010001, Jul 2012. (Cit. on p. 47 and 53)

[75] The ATLAS Collaboration. Observation of a new particle in the search for the Standard Model Higgs boson with the ATLAS detector at the LHC. *Physics Letters B*, 716:1–29, September 2012. (Cit. on p. 48)

[76] The CMS Collaboration. Observation of a new boson at a mass of 125 GeV with the CMS experiment at the LHC. *Physics Letters B*, 716:30–61, September 2012. (Cit. on p. 48)

[77] `http://en.wikibooks.org/wiki/A-level_Physics_(Advancing_Physics)/The_Standard_Model`. (Cit. on p. 50 and 106)

[78] M. E. Peskin and D. V. Schroeder. *An Introduction to Quantum Field Theory*. Westview Press, 1995. (Cit. on p. 49)

[79] M. Goldhaber, L. Grodzins, and A. W. Sunyar. Helicity of Neutrinos. *Physical Review*, 109:1015–1017, February 1958. (Cit. on p. 50)

[80] P. Minkowski. $\mu \rightarrow e\ \gamma$ at a rate of one out of 10^9 muon decays? *Physics Letters B*, 67:421–428, April 1977. (Cit. on p. 50)

[81] M. Gell-Mann, P. Ramond, and R. Slansky. In *Supergravity*, ed. by F. van Nieuwenhuizen and D.Freedmann, 1979. (Cit. on p. 50)

[82] Tsutomu Yanagida. Horizontal Symmetry and Masses of Neutrinos. *Prog.Theor.Phys.*, 64:1103, 1980. (Cit. on p. 50)

[83] R. N. Mohapatra and G. Senjanovic. Neutrino mass and spontaneous parity nonconservation. *Physical Review Letters*, 44:912–915, April 1980. (Cit. on p. 50)

[84] W. Hollik. Electroweak theory. *J.Phys.Conf.Ser.*, 53:7–43, 2006. (Cit. on p. 51)

[85] W. Buchmüller, R. D. Peccei, and T. Yanagida. Leptogenesis as the Origin of Matter. *Annual Review of Nuclear and Particle Science*, 55:311–355, December 2005. (Cit. on p. 51)

[86] S. M. Bilenky and S. T. Petcov. Massive neutrinos and neutrino oscillations. *Rev. Mod. Phys.*, 59:671–754, Jul 1987. (Cit. on p. 52 and 55)

[87] `http://antares.in2p3.fr/users/pradier/orca.html`. (Cit. on p. 52 and 106)

[88] F. Capozzi, G. L. Fogli, E. Lisi, A. Marrone, D. Montanino, and A. Palazzo. Status of three-neutrino oscillation parameters, circa 2013. *Phys. Rev. D*, 89(9):093018, May 2014. (Cit. on p. 54 and 110)

[89] C. Kraus, B. Bornschein, L. Bornschein, J. Bonn, B. Flatt, A. Kovalik, B. Ostrick, E. W. Otten, J. P. Schall, T. Thümmler, and C. Weinheimer. Final results from phase II of the Mainz neutrino mass searching tritium β decay. *European Physical Journal C*, 40:447–468, April 2005. (Cit. on p. 54)

[90] V. N. Aseev, A. I. Belesev, A. I. Berlev, E. V. Geraskin, A. A. Golubev, N. A. Likhovid, V. M. Lobashev, A. A. Nozik, V. S. Pantuev, V. I. Parfenov, A. K. Skasyrskaya, F. V. Tkachov, and S. V. Zadorozhny. Upper limit on the electron antineutrino mass from the Troitsk experiment. *Phys. Rev. D*, 84(11):112003, December 2011. (Cit. on p. 54)

[91] A. Staudt, T.T.S. Kuo, and H.V. Klapdor-Kleingrothaus. beta beta decay of Te-128, Te-130, and Ge-76 with renormalized effective interactions derived from Paris and Bonn potentials. *Phys.Rev.C*, C46:871–883, 1992. (Cit. on p. 55)

[92] E. Caurier, F. Nowacki, A. Poves, and J. Retamosa. Shell Model Studies of the Double Beta Decays of Ge-76, Se-82, and Xe-136. *Phys.Rev.Lett.*, 77:1954–1957, 1996. (Cit. on p. 55)

[93] H. V. Klapdor-Kleingrothaus, A. Dietz, L. Baudis, G. Heusser, I. V. Krivosheina, B. Majorovits, H. Paes, H. Strecker, V. Alexeev, A. Balysh, A. Bakalyarov, S. T. Belyaev, V. I. Lebedev, and S. Zhukov. Latest results from the HEIDELBERG-MOSCOW double beta decay experiment. *European Physical Journal A*, 12:147–154, 2001. (Cit. on p. 55)

[94] the IGEX Collaboration. IGEX ^{76}Ge neutrinoless double-beta decay experiment: Prospects for next generation experiments. *Phys. Rev. D*, 65:092007, May 2002. (Cit. on p. 55)

[95] V. A. Rodin, A. Faessler, F. Šimkovic, and P. Vogel. Uncertainty in the $0\nu\beta\beta$ decay nuclear matrix elements. *Phys. Rev. C*, 68(4):044302, October 2003. (Cit. on p. 55)

[96] The CUORICINO Collaboration, editor. *Results from* CUORICINO *Experiment and Prospects for* CUORE, April 2007. (Cit. on p. 55)

[97] H.V. Klapdor-Kleingrothaus, I.V. Krivosheina, A. Dietz, and O. Chkvorets. Search for neutrinoless double beta decay with enriched Ge-76 in Gran Sasso 1990-2003. *Phys.Lett.*, B586:198–212, 2004. (Cit. on p. 55)

[98] C. Macolino. Results on Neutrinoless Double-Beta Decay from Gerda Phase I. *Modern Physics Letters A*, 29:30001, January 2014. (Cit. on p. 55)

[99] J. Lesgourgues and S. Pastor. Neutrino cosmology and Planck. *New Journal of Physics*, 16(6):065002, June 2014. (Cit. on p. 56, 58, and 106)

[100] J. Lesgourgues, S. Matarrese, M. Pietroni, and A. Riotto. Non-linear power spectrum including massive neutrinos: the time-RG flow approach. *J. Cosm. Astroparticle Phys.*, 6:17, June 2009. (Cit. on p. 55)

[101] M. Viel, M. G. Haehnelt, and V. Springel. The effect of neutrinos on the matter distribution as probed by the intergalactic medium. *J. Cosm. Astroparticle Phys.*, 6:15, June 2010. (Cit. on p. 57, 95, and 106)

[102] A. Lewis and A. Challinor. Evolution of cosmological dark matter perturbations. *Phys. Rev. D*, 66(2):023531, July 2002. (Cit. on p. 56 and 58)

[103] The SPT Collaboration. Constraints on Cosmology from the Cosmic Microwave Background Power Spectrum of the 2500 deg^2 SPT-SZ Survey. *Astrophys. J.*, 782:74, February 2014. (Cit. on p. 58)

[104] The ACT Collaboration. The Atacama Cosmology Telescope: cosmological parameters from three seasons of data. *J. Cosm. Astroparticle Phys.*, 10:60, October 2013. (Cit. on p. 58)

[105] M. Kaplinghat, L. Knox, and Y.-S. Song. Determining Neutrino Mass from the Cosmic Microwave Background Alone. *Physical Review Letters*, 91(24):241301, December 2003. (Cit. on p. 58)

[106] R. de Putter, O. Mena, E. Giusarma, S. Ho, A. Cuesta, H.-J. Seo, A. J. Ross, M. White, D. Bizyaev, H. Brewington, D. Kirkby, E. Malanushenko, V. Malanushenko, D. Oravetz, K. Pan, W. J. Percival, N. P. Ross, D. P. Schneider, A. Shelden, A. Simmons, and S. Snedden. New Neutrino Mass Bounds from SDSS-III Data Release 8 Photometric Luminous Galaxies. *Astrophys. J.*, 761:12, December 2012. (Cit. on p. 59)

[107] M. C. Gonzalez-Garcia, M. Maltoni, J. Salvado, and T. Schwetz. Global fit to three neutrino mixing: critical look at present precision. *Journal of High Energy Physics*, 12:123, December 2012. (Cit. on p. 59)

[108] R. Jimenez, T. Kitching, C. Peña-Garay, and L. Verde. Can we measure the neutrino mass hierarchy in the sky? *J. Cosm. Astroparticle Phys.*, 5:35, May 2010. (Cit. on p. 59)

[109] J. Lesgourgues, G. Mangano, G. Miele, and S. Pastor. *Neutrino Cosmology*. February 2013. (Cit. on p. 59)

[110] A. H. Guth. Inflationary universe: A possible solution to the horizon and flatness problems. *Phys. Rev. D*, 23:347–356, January 1981. (Cit. on p. 61)

[111] Y. Zhang, Y. Yuan, W. Zhao, and Y.-T. Chen. Relic gravitational waves in the accelerating Universe. *Classical and Quantum Gravity*, 22:1383–1394, April 2005. (Cit. on p. 62)

[112] The PLANCK Collaboration. Planck 2013 results. XXII. Constraints on inflation. *ArXiv e-prints*, March 2013. (Cit. on p. 62)

[113] The BICEP2 Collaboration. Detection of $B-$Mode Polarization at Degree Angular Scales by BICEP2. *Physical Review Letters*, 112(24):241101, June 2014. (Cit. on p. 62)

[114] R. Flauger, J. C. Hill, and D. N. Spergel. Toward an Understanding of Foreground Emission in the BICEP2 Region. *ArXiv e-prints*, May 2014. (Cit. on p. 62)

[115] The EBEX Collaboration. EBEX: a balloon-borne CMB polarization experiment. In *Society of Photo-Optical Instrumentation Engineers (SPIE) Conference Series*, volume 7741 of *Society of Photo-Optical Instrumentation Engineers (SPIE) Conference Series*, July 2010. (Cit. on p. 64 and 68)

[116] The POLARBEAR Collaboration. Ultra High Energy Cosmology with POLARBEAR. *ArXiv e-prints*, October 2011. (Cit. on p. 64 and 68)

[117] The PLANCK Collaboration. The Scientific Programme of PLANCK. *ArXiv Astrophysics e-prints*, April 2006. (Cit. on p. 64 and 89)

[118] L. Perotto, J. Lesgourgues, S. Hannestad, H. Tu, and Y. Y. Y. Wong. Probing cosmological parameters with the CMB: forecasts from Monte Carlo simulations. *J. Cosm. Astroparticle Phys.*, 10:13, October 2006. (Cit. on p. 64 and 82)

[119] E. Calabrese, A. Cooray, M. Martinelli, A. Melchiorri, L. Pagano, A. Slosar, and G. F. Smoot. CMB lensing constraints on dark energy and modified gravity scenarios. *Phys. Rev. D*, 80(10):103516, November 2009. (Cit. on p. 64 and 82)

[120] T. Okamoto and W. Hu. Cosmic microwave background lensing reconstruction on the full sky. *Phys. Rev. D*, 67(8):083002, April 2003. (Cit. on p. 65, 71, and 89)

[121] D. Hanson, A. Challinor, and A. Lewis. Weak lensing of the CMB. *General Relativity and Gravitation*, 42:2197–2218, September 2010. (Cit. on p. 65)

[122] G. Efstathiou. Principal-component analysis of the cosmic microwave background anisotropies: revealing the tensor degeneracy. *MNRAS*, 332:193–198, May 2002. (Cit. on p. 66)

[123] E. D. Valentino, A. Melchiorri, and L. Pagano. Testing the Inflationary Null Energy Condition with Current and Future Cosmic Microwave Background Data. *International Journal of Modern Physics D*, 20:1183–1189, 2011. (Cit. on p. 66)

[124] L. Wolz, M. Kilbinger, J. Weller, and T. Giannantonio. On the validity of cosmological Fisher matrix forecasts. *J. Cosm. Astroparticle Phys.*, 9:9, September 2012. (Cit. on p. 68)

[125] A. Lewis and S. Bridle. Cosmological parameters from CMB and other data: A Monte Carlo approach. *Phys. Rev. D*, 66(10):103511, November 2002. (Cit. on p. 68)

[126] The WMAP Collaboration. Seven-year Wilkinson Microwave Anisotropy Probe (WMAP) Observations: Cosmological Interpretation. *Astrophys. J. Supp.*, 192:18, February 2011. (Cit. on p. 68)

[127] F. Stivoli, J. Grain, S. M. Leach, M. Tristram, C. Baccigalupi, and R. Stompor. Maximum likelihood, parametric component separation and CMB $B-$mode detection in suborbital experiments. *MNRAS*, 408:2319–2335, November 2010. (Cit. on p. 69 and 74)

[128] Y. Fantaye, F. Stivoli, J. Grain, S. M. Leach, M. Tristram, C. Baccigalupi, and R. Stompor. Estimating the tensor-to-scalar ratio and the effect of residual foreground contamination. *J. Cosm. Astroparticle Phys.*, 8:1, August 2011. (Cit. on p. 69 and 74)

[129] A. Gelman and D.B. Rubin. Inference from iterative simulation using multiple sequences. *Statistical Science*, 7:457–511, 1992. `http://www.stat.columbia.edu/~gelman/research/published/itsim.pdf`. (Cit. on p. 69)

[130] C. Blake, E. A. Kazin, F. Beutler, T. M. Davis, D. Parkinson, S. Brough, M. Colless, C. Contreras, W. Couch, S. Croom, D. Croton, M. J. Drinkwater, K. Forster, D. Gilbank, M. Gladders, K. Glazebrook, B. Jelliffe, R. J. Jurek, I.-H. Li, B. Madore, D. C. Martin, K. Pimbblet, G. B. Poole, M. Pracy, R. Sharp, E. Wisnioski, D. Woods, T. K. Wyder, and H. K. C. Yee. The WiggleZ Dark Energy Survey: mapping the distance-redshift relation with baryon acoustic oscillations. *MNRAS*, 418:1707–1724, December 2011. (Cit. on p. 69)

[131] The SDSS Collaboration. First-Year Sloan Digital Sky Survey-II Supernova Results: Hubble Diagram and Cosmological Parameters. *Astrophys. J. Supp.*, 185:32–84, November 2009. (Cit. on p. 69)

[132] A. G. Riess, L. Macri, S. Casertano, M. Sosey, H. Lampeitl, H. C. Ferguson, A. V. Filippenko, S. W. Jha, W. Li, R. Chornock, and D. Sarkar. A Redetermination of the Hubble Constant with the Hubble Space Telescope from a Differential Distance Ladder. *Astrophys. J.*, 699:539–563, July 2009. (Cit. on p. 69)

[133] J. Bock, A. Aljabri, A. Amblard, D. Baumann, M. Betoule, T. Chui, L. Colombo, A. Cooray, D. Crumb, P. Day, C. Dickinson, D. Dowell, M. Dragovan, S. Golwala, K. Gorski, S. Hanany, W. Holmes, K. Irwin, B. Johnson, B. Keating, C.-L. Kuo, A. Lee, A. Lange, C. Lawrence, S. Meyer, N. Miller, H. Nguyen, E. Pierpaoli, N. Ponthieu, J.-L. Puget, J. Raab, P. Richards, C. Satter, M. Seiffert, M. Shimon, H. Tran, B. Williams, and J. Zmuidzinas. Study of the Experimental Probe of Inflationary Cosmology (EPIC)-Intemediate Mission for NASA's Einstein Inflation Probe. *ArXiv e-prints*, June 2009. (Cit. on p. 70 and 72)

[134] The PRISM Collaboration. PRISM (Polarized Radiation Imaging and Spectroscopy Mission): A White Paper on the Ultimate Polarimetric Spectro-Imaging of the Microwave and Far-Infrared Sky. *ArXiv e-prints*, June 2013. (Cit. on p. 70 and 89)

[135] L. Perotto, J. Bobin, S. Plaszczynski, J. . Starck, and A. Lavabre. Reconstruction of the CMB lensing for PLANCK. *ArXiv e-prints*, March 2009. (Cit. on p. 71 and 72)

[136] Y. Fantaye, C. Baccigalupi, S. M. Leach, and A. P. S. Yadav. CMB lensing reconstruction in the presence of diffuse polarized foregrounds. *J. Cosm. Astroparticle Phys.*, 12:17, December 2012. (Cit. on p. 72, 82, and 88)

[137] Stephen P. Brooks and Andrew Gelman. General methods for monitoring convergence of iterative simulations. *Journal of Computational and Graphical Statistics*, 7(4):434–455, 1998. `http://www.stat.columbia.edu/~gelman/research/published/brooksgelman2.pdf`. (Cit. on p. 73)

[138] G. Efstathiou and S. Gratton. $B-$mode detection with an extended PLANCK mission. *J. Cosm. Astroparticle Phys.*, 6:11, June 2009. (Cit. on p. 73)

[139] L. Pagano, P. de Bernardis, G. de Troia, G. Gubitosi, S. Masi, A. Melchiorri, P. Natoli, F. Piacentini, and G. Polenta. CMB polarization systematics, cosmological birefringence, and the gravitational waves background. *Phys. Rev. D*, 80(4):043522, August 2009. (Cit. on p. 74)

[140] L. Knox and Y.-S. Song. Limit on the Detectability of the Energy Scale of Inflation. *Physical Review Letters*, 89(1):011303, July 2002. (Cit. on p. 79)

[141] M. Kesden, A. Cooray, and M. Kamionkowski. Separation of Gravitational-Wave and Cosmic-Shear Contributions to Cosmic Microwave Background Polarization. *Physical Review Letters*, 89(1):011304, July 2002. (Cit. on p. 79)

[142] R. Stompor and G. Efstathiou. Gravitational lensing of cosmic microwave background anisotropies and cosmological parameter estimation. *MNRAS*, 302:735–747, February 1999. (Cit. on p. 82)

[143] A. Benoit-Lévy, K. M. Smith, and W. Hu. Non-Gaussian structure of the lensed CMB power spectra covariance matrix. *Phys. Rev. D*, 86(12):123008, December 2012. (Cit. on p. 82)

[144] C. Carbone, C. Baccigalupi, M. Bartelmann, S. Matarrese, and V. Springel. Lensed CMB temperature and polarization maps from the Millennium Simulation. *MNRAS*, 396:668–679, June 2009. (Cit. on p. 82, 84, 85, and 93)

[145] M. Zaldarriaga and U. Seljak. Reconstructing projected matter density power spectrum from cosmic microwave background. *Phys. Rev. D*, 59(12):123507, June 1999. (Cit. on p. 83 and 86)

[146] C.-P. Ma and E. Bertschinger. Cosmological Perturbation Theory in the Synchronous and Conformal Newtonian Gauges. *Astrophys. J.*, 455:7, December 1995. (Cit. on p. 83)

[147] A. Refregier. Weak Gravitational Lensing by Large-Scale Structure. *Ann. Rev. Astron. Astrophys.*, 41:645–668, 2003. (Cit. on p. 83)

[148] The WMAP Collaboration. First-Year Wilkinson Microwave Anisotropy Probe (WMAP) Observations: Determination of Cosmological Parameters. *Astrophys. J. Supp.*, 148:175–194, September 2003. (Cit. on p. 84 and 90)

[149] V. Springel. The cosmological simulation code GADGET-2. *MNRAS*, 364:1105–1134, December 2005. (Cit. on p. 84)

[150] K. M. Gorski, B. D. Wandelt, F. K. Hansen, E. Hivon, and A. J. Banday. The HEALPIX Primer. *ArXiv Astrophysics e-prints*, May 1999. (Cit. on p. 86)

[151] L. Knox. Determination of inflationary observables by cosmic microwave background anisotropy experiments. *Phys. Rev. D*, 52:4307–4318, October 1995. (Cit. on p. 87)

[152] W. Hu. Mapping the Dark Matter through the Cosmic Microwave Background Damping Tail. *Astrophys. J. Lett.*, 557:L79–L83, August 2001. (Cit. on p. 87)

[153] W. Hu. Angular trispectrum of the cosmic microwave background. *Phys. Rev. D*, 64(8):083005, October 2001. (Cit. on p. 87 and 88)

[154] W. Hu and T. Okamoto. Mass Reconstruction with Cosmic Microwave Background Polarization. *Astrophys. J.*, 574:566–574, August 2002. (Cit. on p. 87)

[155] W. Hu, S. DeDeo, and C. Vale. Cluster mass estimators from CMB temperature and polarization lensing. *New Journal of Physics*, 9:441, December 2007. (Cit. on p. 87)

[156] J. Yoo, M. Zaldarriaga, and L. Hernquist. Lensing reconstruction of cluster-mass cross correlation with cosmic microwave background polarization. *Phys. Rev. D*, 81(12):123006, June 2010. (Cit. on p. 87 and 88)

[157] S. Plaszczynski, A. Lavabre, L. Perotto, and J.-L. Starck. A hybrid approach to cosmic microwave background lensing reconstruction from all-sky intensity maps. *Astron. & Astrophys.*, 544:A27, August 2012. (Cit. on p. 90)

[158] C. Carbone et al. The simulated ISWRS effect in the presence of massive neutrinos. *In preparation*, 2014. (Cit. on p. 95)

[159] C. Carbone et al. CMB lens-induced polarization from the DEMNUNI simulations. *In preparation*, 2014. (Cit. on p. 95)

[160] E. Castorina et al. Dark matter and halo clustering frm the DEMNUNI simulations. *In preparation*, 2014. (Cit. on p. 95)

[161] M. Calabrese, C. Carbone, M. Baldi, and C. Baccigalupi. Multiple planes weak-lensing of the CMB. *In preparation*, 2014. (Cit. on p. 103)

[162] F. Bianchini et al. Cross-correlation between the CMB lensing potential measured by PLANCK and high-z sub-mm galaxies detected by the HERSCHEL-ATLAS survey. *Submitted to Astrophys. J.*, 2014. (Cit. on p. 103)